

(NASA-CR-140448) A THEORETICAL AND
 FLIGHT TEST STUDY OF PRESSURE
 FLUCTUATIONS UNDER A TURBULENT BOUNDARY
 LAYER. PART 2: FLIGHT TEST STUDY
 (Texas Univ.) 106 p HC \$8.50 CSCL 20D G3/12 50855
 N74-33797 Unclas

FINAL REPORT
NASA Grant NGR 37-002-083
Ames Research Center

**A THEORETICAL AND FLIGHT TEST STUDY OF
 PRESSURE FLUCTUATIONS UNDER A
 TURBULENT BOUNDARY LAYER**

Project Directors

Ronald L. Panton
 Mechanical Engineering
 The University of Texas
 Austin, Texas

Richard L. Lowery
 Mechanical and Aerospace
 Engineering
 Oklahoma State University
 Stillwater, Oklahoma

'PART TWO
FLIGHT TEST STUDY

by

R. L. Panton, R. L. Lowery, and M. M. Reischman



TABLE OF CONTENTS

- I. INTRODUCTION
- II. FLOW FIELD CHARACTERISTICS
 - Glider Description
 - Inviscid Flow Field
 - Boundary Layer
- III. PRESSURE FLUCTUATION MEASUREMENT
 - Microphone Selection
 - Microphone Calibration
- IV. RESULTS
 - Root-Mean-Square Values
 - Power Spectra
 - Cross Power Spectra
- V. SUMMARY

I. INTRODUCTION

The study of pressure fluctuations under a turbulent boundary layer was undertaken with the objective of extending previous work to lower frequencies. Wind tunnel and flight test measurements are invalid at low frequencies because of extraneous acoustic noises and free stream turbulence.

A glider was instrumented and used as a test bed to carry microphones into a smooth flow free of acoustic noise. Hodgson had previously measured the spectrum of boundary layer noise on a glider wing. These tests showed a drop off at low frequencies that could not be reproduced in any other facility. Hodgson tripped the boundary layer at 15 percent chord and tried to pick the zero point in the pressure gradient curve for his measurement location. This procedure resulted in measurements made at 50 percent chord.

The measurements reported here were made on the forward fuselage of a glider where the boundary layer could develop naturally and have some length in a zero pressure gradient before the measurements were made. Two different sets of measurements were made. First, measurements with a single microphone and simultaneous measurement of the boundary layer profile were made. These tests included three microphone sizes and both natural and tripped

transition. The second set of measurements was a spatial array of microphones without the boundary layer measurement. Tripping was necessary in these tests in order to have a well developed turbulent layer over the entire region.

Prior to the pressure fluctuation tests several preliminary investigations were conducted. A series of flights were made to survey the static pressure on the fuselage forward of the wing and locate a constant pressure region. Next, a tuft study was conducted to find the flight speeds at which the flow was aligned with the fuselage. Finally, the boundary layer was surveyed at several points for information concerning its velocity profile.

The major results of the complete experimental program can be summarized as follows: the boundary layer flow was found to be typical of a zero pressure gradient layer; the pressure spectrum was found to drop off at low frequencies, and the spatial changes in the coherence function were determined. Convective velocity information was judged to be incorrect because of phase errors introduced by damaged microphones.

II. FLOW FIELD CHARACTERISTICS

Glider Description

The tests were run on a Schweizer 2-32 sailplane (Fig. 1). This is an all-metal, two-place, high-performance sailplane of rugged construction. Stall speed is around 48 mph and maximum speed 155 mph. At 60 mph the best glide ratio of 34:1 is obtained. The useful load is 490 pounds.

Measurements were made on the lower portion of the fuselage just forward of the wing (Fig. 2). In this area the lower half of the fuselage is a 16 inch radius circular cylinder for a length of 60 inches. The forward fuselage has complete cylindrical symmetry tapering down to a 2 inch radius spherical nose cap. The axis of the nose cap and forward fuselage section is canted downward at 3.5° with respect to the axis of the 16 inch cylinder. The nose cap did not join smoothly to the fuselage so the joint area was filled and refinished. This left a flat region of 3 or 4 inches around the nose cap joint. In the center of the nose cap the aircraft total pressure port is located within a cup-shaped indentation approximately 1 inch in diameter and 1 inch deep. This configuration prevents icing. Air vent holes are located on each side in the lower quadrant of the

nose cap. The vent on the measurement side of the aircraft was plugged and filled to give a smooth contour. Other modifications included smoothing the forward fuselage nose-cap junction.

Inviscid Flow Field

Unpowered aircraft with a fixed weight will have certain steady state indicated airspeed (or dynamic pressure) associated with each angle of attack (or lift coefficient). Therefore the inviscid flow field and pressure distribution depend only upon the glider angle of attack. From the operation standpoint picking an indicated airspeed gives a definite inviscid flow field and pressure distribution for the test irrespective of altitude. Changing the airspeed not only changes the Reynolds number, but also gives a slightly different pressure distribution and flow field. For these reasons, most tests were run in the narrow range of airspeeds 55, 60, and 65 mph.

Sailplanes are customarily flown at constant airspeed by noting the visual position of the horizon on the canopy. Reference marks on the canopy and the sailplane pitch trim system allowed the pilot to fly a constant airspeed and angle of attack without difficulty. A yarn yaw string taped

to the skin in front of the canopy gave a sensitive indication and was used to insure the fuselage was not yawed. Flights were conducted in the early morning and sometimes in the early evening when the convection layer was thinner. As a general rule the sailplane released 3,000 feet above the top of the convective layer and all data runs were completed in the first 2,000 feet of altitude loss. The release altitude was typically 7,000 feet, although some flights were released as high as 10,000 feet.

A tuft study was done to determine the direction of flow on the fuselage as a function of airspeed. Motion pictures were taken from another plane flying formation with the glider. Figure 3 shows some still photographs taken from the film. The glider actually flies most efficiently around 60 mph; higher airspeeds are obtained by tucking the nose down considerably with a resulting flow from the top of the fuselage around toward the bottom. The lower airspeeds of 55, 60, and 65 mph have the best flow direction over the fuselage, and were chosen for the primary test speeds. Pictures taken at 80 and 90 mph (not shown) reveal considerable cross flow around the nose.

The pressure field was surveyed at the grid positions shown in Fig. 4. A bank of water manometers was mounted on

the back of the pilot's seat and were photographed by the occupant of the rear seat. A typical photograph is shown in Fig. 5.

It was not necessary to know the manometer scale or inclination about the pitch axis. The pressures were referenced to P_{∞} and the total pressure P_o measured; then $C_p = (P - P_{\infty})/q$ is found by dividing $P - P_{\infty}$ column by the $P_o - P_{\infty}$ column. Although the pitch inclination was not important, errors in the roll axis have considerable influence on the results. A roll error in mounting the manometer board was measured in the hanger when the wings were level. From one side of the board to the other, a .1 inch difference in scale was noted, and a correction for this effect was incorporated in the data reduction. Although the difference between adjacent manometers is small, the correction accumulates to the order of .05 in C_p over the length of the measurement region. The manometer board gave consistent results for several different flights, including one removal and reinstallation. It is felt that the pilot could fly with the wings level to within a very small error. A one degree error in roll is equivalent to six inch error at the wing tip. Considering reading accuracy and data reduction it was estimated that an error of ± 0.02 in C_p could occur for any point.

7

The static pressure survey results are given in Figs. 6 through 19. Pressure coefficient as a function of distance in the flow direction is plotted from an arbitrary origin 43.6 inches aft of the nose (see Fig. 4). The highest row, A, is in front of the wing, and the C_p plot shows the effect of the flow stagnating. A plot for row B shows the same effect, but has one point which is located under the wing at $x = 60$ inches. At this point, the air has accelerated to go under the wing and the pressure drops. Plots for rows C and D show similar trends with decreasing influence as one moves away from the wing. At the forward stations, Figs. 8 and 9, also show the flow recompressing from the low pressure obtained as the flow turns around the nose. The C_p plot for row E shows a region of constant pressure of about 40 inches. A plot for row F has a slight dip in pressure at about $x = 40$ followed by a compression as the flow nears the main landing gear. The dip has been checked, and is not an error in data reduction, but it is somewhat unexpected. It is within the accuracy of the measurement.

Cross-plots giving the pressure field at a fixed station are shown in Figs. 12 through 18. The origin for these graphs was the top row of taps and the Y distance is measured along the skin (see Fig. 4). Transverse pressure

gradients, except at wing level, are moderate until one progresses to column 7 which is under the wing; here both the wing and wheel effects are evident.

A line slightly above Row E, 50.7 degrees down from horizontal on the cylinder, was selected for the primary microphone instrumentation. The pressure distribution along this line and continuing to the nose is shown on Fig. 19. The region for the measurements was located somewhat lower than we expected prior to taking the pressure survey.

Mounting brackets which would accept two 2-inch diameter instrument plugs were attached to the sailplane along the measurement line. One bracket was located so the aft hole was 83.5 inches from the nose, and the other bracket located at 60.6 inches from the nose. Figs. 13 and 14 which show the final microphone arrays, also give the location of the instrument plugs.

Boundary Layer

The boundary layer mean velocity profile was found at two stations along the measuring line; the aft plug of each bracket. On tests where a single microphone was used, it was placed at the 80.4 inch station, and a traversing pitot tube located at the 83.5 inch station. In order to

establish the boundary layer growth, some additional data were taken at the 60.6 inch forward bracket location. The traversing pitot probe was driven with a cam in such a way that it moved very slowly near the wall. It made one cycle in about 20 seconds and stroked 2 inches. The static tap was located in the same instrument plug at a position where the reading did not change as the pitot traversed in and out. Position of the pitot was measured electrically and recorded on tape, along with the pressure transducer signal. Analysis of the boundary layer was done by plotting the profiles of three consecutive traverse cycles on an x-y plotter as shown in Fig. 22. An average line was then drawn and points taken from this line for computer processing.

In analyzing the boundary layer data the method used in the "1968 AFOSR-IFP-Stanford Conference on Computation of Turbulent Boundary Layers" was employed. Many previous wind tunnel experiments have been processed by the same method and the results are given in the conference proceedings. The boundary layer is assumed to be one of the profiles from the "equilibrium" family. The law of the wall plus the law of the wake is written in the following form:

$$\frac{u}{u^*} = \frac{1}{k} \ln \left(\frac{yu^*}{\nu} \right) + C + \frac{2\Pi}{k} \sin^2 \left(\frac{\pi}{2} \frac{y}{\delta} \right)$$

where

u = mean velocity

y = distance from wall

u^* = friction velocity = $(\tau_w/\rho)^{1/2}$

τ_w = wall shear stress

ρ = fluid density

ν = kinematic viscosity

K = Von Karmann constant (.41)

C = law of wall constant (5.0)

Π = wake parameter

δ = boundary layer thickness

The procedure adopted by the conference and followed by us was to choose K and C and determine the values of u^* , Π and δ by a least squares fit to the data points. The fit excludes points in the inner 15% and outer 25% of the boundary layer. The inner points are excluded because of questions about the accuracy of a pitot tube when the fluctuations in velocity become a large portion of the mean velocity. The outer points are excluded because of the known deficiency of the wake expression to transition properly into the free stream.

The three parameters u^* , δ , and Π characterize the boundary layer, and any other "thickness" or shape parameter

can be computed with the profile equation. The friction velocity u^* and boundary layer thickness δ and Π are not independent of each other. By setting $y = \delta$ in the previous equation, a complicated skin friction law between u^*/U_∞ , Π , and Re_δ results. The wake strength parameter by definition takes on a constant value for an equilibrium layer. Experimental values for a constant pressure layer are around $\Pi = 0.62$. Earlier values of 0.55 are often quoted.

A summary of the boundary layer properties are tabulated in Tables 1, 2, and 3. They are grouped according to the sailplane indicated airspeed because theoretically a slightly different inviscid flow occurs at each airspeed. Even though the data is taken in a constant pressure region, the location of transition is strongly affected by slight changes in the forward pressure distribution. At any position on sailplane, the boundary layer will depend upon indicated airspeed (fixed inviscid flow field) and the Reynolds number $U_\infty L/\nu$, where L is a characteristic of the sailplane. In particular δ/L or δ^*/L should be plotted vs. $U_\infty L/\nu$. It is customary to take $L = 1$, ignore the dimensions, and use a unit Reynolds number. Hence we have plotted in Fig. 23, δ^* vs. $U_\infty L/\nu$ with indicated airspeed as a parameter. The unit Reynolds number does not change much, and there is no

discernible trend in δ^* . Higher indicated airspeed, on the other hand, increased the boundary layer thickness by moving the transition forward. Flights 76 and 77 are consistently too high in δ^* (also δ and Π) at all airspeeds, and the data is judged to be erroneous. The reason is unknown.

After the boundary layer has developed, its structure in nondimensional terms should be like any other zero pressure gradient layer. Figures 24, 25 and 26 display C_f ($C_f = 2u_*^2/U_\infty^2$), Π , and H ($H = \delta^*/\theta$) as functions of Re_δ^* . Indicated airspeed should enter these graphs only through Re_δ^* , and not as a parameter. For comparison, the experimental measurements of Wieghardt are also plotted. Wieghardt's data was chosen by the AFOSR-IFP-Stanford Conference as typical of a zero pressure gradient layer. Wieghardt's data were taken at various distances along a flat plate in a wind tunnel. The leading edge of the plate was blunt with a trip wire attached.

Figure 24 gives the skin friction coefficient vs. Reynolds number. The scatter in the data points gives an indication of the degree of consistency between flights and airspeeds. As mentioned previously, the velocity profile equation employs a skin friction law which could be of the form $C_f(\Pi, Re_\delta^*)$. Wieghardt's data is consistent with the curve $C_f(\Pi = .62, Re_\delta^*)$, except for a small deviation at

low Re_δ^* . Lower values of Π produce a skin friction curve which is higher. The data points marked "FP" were taken at the front instrument mounting position at station 60.6. In the untripped case the forward points are somewhat higher than Wieghardt's data. Another noticeable trend is that the tripped data is lower than the untripped experiments.

The trends of the C_f curves and the associated values of Π are, of course, consistent because of the method of calculation. When plotting Π vs. Re_δ^* in Fig. 25 it can be seen that for the untripped layer, the data are scattered around 0.5 to 0.6; this is slightly lower than fully developed value of 0.62, which Wieghardt's data achieves at large Reynolds numbers. The untripped forward plug points are around 0.2. There is a well-known tendency for Π to drop off at the beginning of a constant pressure layer. It appears that the turbulent boundary layer is still young at the forward position, but has matured by the time it reaches the aft instrument location. On the other hand, the tripped boundary layer has higher values of the wake component, that is; $\Pi = 0.5$ to 0.9 and shows no drop-off at the forward position.

The shape factor is plotted in Fig. 26. Again the untripped data follows the trend of Wieghardt's data at the

aft position, but not at the forward position. The tripped boundary layer data are somewhat higher, but follow the proper Re_{δ}^* trend when the airspeed is constant. There is a tendency for the tripped points to be further from the curve as the airspeed increases. Returning to the wake factor Π curves, one can also see a slight trend for Π to increase with higher airspeed. One must conclude that there is an artifact of the tripping, which increases the wake component slightly over its nominal value. The amount of the increase is a weak function of the indicated airspeed. In order to put this in perspective, the boundary layer velocity profile data recently published by Wills (4) was processed in a similar manner. The value of Π computed was 0.89, which is larger than the data points reported here at 55 and 60 mph.

In the spatial correlation tests, since the microphones were mounted large distances apart, it is necessary to account for boundary layer growth. Boundary layer data from the two mounting positions was interpolated (and extended aft in one case) by assuming a simple power law growth formula:

$$\delta = C(x - x_0)^{\frac{n+1}{n+3}}$$

where n is the exponent in the velocity profile $u/U_{\infty} = (y/\delta)^{1/n}$. An average value of $H = 1.4$ implies that n is

equal to 5. The constants C and x_0 may be determined at each airspeed from the two measurements. The "apparent" origin of the turbulence, x_0 , was measured forward of the front measuring position (station 60.6 inches) and is at least a qualitative indication of the length of turbulence in front of the first station.

A/S	x_0 untripped	C	x_0 tripped	C
55	13.2 in.	.00747	39.6 in.	.00768
60	15.2 in.	.00734	42.4 in.	.00795
65	14.8 in.	.00804	47.5 in.	.00797

The small lengths for the untripped tests agree with the idea that the Π values at the first station were low because the boundary layer was young, and the wake component not yet fully established.

To summarize: A region of zero pressure gradient was located along the lower fuselage, with a length of about 40 inches and a width of perhaps 15 inches; the flow direction was aligned with the fuselage at the low airspeeds, and tests were therefore limited to 55, 60 and 65 mph. The untripped boundary had the mean flow properties of a nominal zero pressure gradient layer at the aft measuring position, but had a very small wake component at the forward position; the tripped layer had nominal mean flow properties at both

locations, except for a slightly large wake component and slightly low C_f . This component was not so large that the boundary layer should be considered abnormal.

III. PRESSURE FLUCTUATION MEASUREMENT

Microphone Electronics

The choice of the microphones used for measuring the turbulent boundary layer pressure fluctuation was governed by three criteria: (1) the smallest possible size, (2) good low frequency response, and (3) sensitivity. Of course, other considerations such as signal to noise ratio were considered in making the selection.

After comparing all commercially available microphones and some which are available only on a custom basis, the pressure field microphone series manufactured by Bruel & Kjaer Instruments was selected. The smallest of the microphones, the model 4136, is nominally one-quarter inch in diameter with a fundamental resonance of approximately 40,000 Hz. The half-inch microphone type 4134 has a fundamental resonance of approximately 20,000 Hz. The type 4132 is nominally one inch in diameter with the fundamental resonance at approximately 12 kHz.

The bandwidth of interest in the turbulent boundary layer is 5 Hz to 10 kHz which is within the range of all three of the microphones used. The low frequency response of each of the three types of microphones depends upon the

capacitance of the preamplifier used. While several different versions of electronics are available for this series of microphones, the Bruel & Kjaer type 2619 preamplifier was selected since it operates well from a battery powered supply and has a very high input impedance. The design of the Bruel & Kjaer condenser microphone is such that the low frequency response is governed by the capacitance of the microphone and not the acoustic vent time. For example, the smallest of the microphones used, the 4136, is designed with the pressure equilization vent sized so that the -3 db cutoff point is between .5 and 5 Hz. The typical frequency response of the type 4136 pressure field microphone operating with the type 2619 preamplifier is flat between 5 Hz and 10,000 Hz at random incidence. The pressure response is down 3 db at 3 Hz. The one-half inch and one inch models display equally good low frequency response characteristics.

The method of assembly of the Bruel & Kjaer microphone is such that a small shoulder is left at the periphery of the diaphragm. Otherwise the microphone is sufficiently flat that it would not disrupt the boundary layer. Since the shoulder is outside of the active diaphragm area, it is possible to fill the Champford Annulus with a soft lacquer to present a flatter surface to the boundary layer. This

technique was used on the 1/2 and 1 inch diameter microphones with no noticeable detriment in performance. The annulus on the 1/4 inch microphones was small enough to be considered unimportant.

The one-quarter inch microphone was considered the primary transducer since the size correction factor would be less than those of the larger microphones. This microphone, however, was inferior to the other two models in the areas of self-noise and sensitivity. However, since the root mean square levels of the pressure fluctuations at the boundary layer are on the order of 100 db the relatively high threshold of the quarter inch microphone was not a problem. However, the 1/4 inch microphone is extremely fragile and practically all of them were damaged during the test program.

Since the magnetic tape recorder requires considerably more voltage than that produced by the type 2619 microphone pre-amplifier, additional amplification was utilized. A bank of integrated circuit operational amplifiers was constructed which produce the needed gain without a sacrifice in frequency response. The operational amplifiers used in the system, which were manufactured by Analog Devices, proved to be quite stable in gain setting and zero offset. This type of device was selected for the reason that most

conventional wide-band data amplifiers include many additional features and flexibility which were not required for this application since most of the tests were made at a single value of system gain. The operational amplifiers also have the advantage of requiring very low battery drain, permitting a large number to be incorporated in the aircraft.

The microphone signals and other flight data were recorded on a Leach Corporation model 3200 tape recorder. This recorder operates on 28 volts DC. Twelve channels recorded in the FM mode and two channels were operated in the direct mode. Several flight variables, pressures and temperature, were multiplexed on the direct channels through voltage controlled oscillators. Six minutes of recording were available when the recorder was operated at 30 ips.

The main power supply was a set of motorcycle batteries. The batteries, tape recorder, and assorted electronic devices were mounted into a module. The module was then secured by the seat belt attachments into the second seat; immediately behind the pilot. The pilot could control the recorder, power supplies, and traversing motor through switches on his panel.

Microphone Calibration

A number of microphone calibration schemes were tested before the final version was put into effect. Ordinarily a microphone is tested at the factory and supplied to the purchaser with a calibration curve traceable to the National Bureau of Standards. However, the microphone diaphragms were exposed to flying debris during the takeoff and landing of the aircraft and were also subjected to shock and vibration and various forces and moments during their installation and removal from the craft. In several instances the sensitivities of the microphones were noticeably changed after a period of use. Therefore, the final calibration procedure involved the use of a piston phone type device applied over the face of the microphone when mounted in the aircraft.

The piston phone consists of a small electrodynamic loudspeaker mounted in a plastic tube approximately twelve inches long. Neither end of this tube is tightly sealed and the end applied to the fuselage of the aircraft is equipped with a soft rubber gasket which was designed to exclude exterior noises during the calibration process. The seal is porous and permits air to leak out readily to prevent damage to the diaphragm when applying the piston phone. The device

was calibrated with a standard precision soundlevel meter which in turn was calibrated with a commercial piston phone taking into account barometric variations.

A frequency of 500 Hz was selected for the test frequency since the piston phone was relatively insensitive to frequency changes. At that point the application of 31 millivolts rms to the loudspeaker of the piston phone produced a pressure field of 100 db relative to $.0002 \mu$ bar. Output was measured at the tape recorder input with the recorder operating. While earlier tests were made by driving the transducer with a variable frequency oscillator, the final test procedure incorporated the use of a power amplifier having an output impedance of 8 ohms. If the piston phone is not driven by low impedance source, the minute changes in electromechanical impedance due to variations in clamping pressure at the foam rubber seal make the stabilization of the sound pressure level difficult. When the device is driven by a small power amplifier the sound pressure level remains unchanged even if the seal of the tube is lifted away from the surface a fraction of an inch. This method of testing proved to be reproducible and in subsequent tests the sensitivity of the device proved to be quite constant for over a long period of time and at different temperatures.

In addition to the "100 db" test, the rms of the recorded signals were measured immediately after each flight. The rms pressure is closely a function of dynamic pressure and so varies only with indicated airspeed. Tables which present the history of each microphone are given in Tables 4 through 13. These histories are during the spatial correlation flight program. Numbers in the same vertical column can be compared directly. Any number which deviates more than about $\pm 5\%$ from the average has been underlined.

The half-inch microphones were very consistent except for number three. The difficulties with this microphone in the early flights was traced to a bad pre-amplifier. Replacing this amplifier occurred after flight 92, and good results were obtained thereafter. Of the six remaining underlined numbers, half occurred on the 65 mph run in flight 96. It appears that the airspeed was low on this run.

The quarter-inch microphones proved to be easily damaged. Sometimes the damage was progressive and sometimes it was traumatic. With use the diaphragms became dull and showed small pits as if they were bombarded with dust. Half-inch diaphragms had a similar appearance without any change in performance. When a microphone gave a bad calibration one could usually detect a striated scrape mark,

a rough mark or several wrinkles somewhere on the active surface. Microphones with this type of damage usually showed an increased sensitivity, operating as if the diaphragm was too loose.

Another type of damage was a loose cap. The B&K microphone is constructed by welding the diaphragm to an internally threaded cylinder to form a cap. The cap is then screwed to the base electrode until the diaphragm touches a support ring. Further screwing stretches the diaphragm to its proper tension. There is no positive locking of the cap and in two instances caps were found in a loosened condition. Damage of this type undoubtedly occurred during ground handling, installation, or removal. When a loose cap is retightened, perhaps inadvertantly during installation, it may be too tight resulting in a decrease in sensitivity.

The histories of quarter-inch microphones show that only numbers 1 and 3 gave consistent results throughout the program. Microphone number 5 had only two runs which were out of the $\pm 5\%$ tolerance but the results tend to get progressively higher. On flights 95 and 96 microphones 2, 4, and 6 are probably damaged and 4 and 6 were not flush with aircraft skin. Excluding the bad microphones of flights 95 and 96, there are 13 out-of-tolerance data points and nine

of these occur on 65 mph tripped experiments. This would seem a significant trend; however, there is no apparent reason. Measurements of the frequency response of the damaged microphones were attempted after the flight test program. Electrostatic actuator tests showed that all microphones sensitivities would not drop more than 2 db until the frequency was lower than 20 cycles. The response curves were flat out to 10 kHz on the high end. It is not possible to conclude that the frequency response of the damaged microphones was unchanged because of the artificial nature of the electrostatic actuator test. In the test a polarization voltage of 800 volts is applied between the actuator and the diaphragm. This pulls the diaphragm away from its normal position. Ordinarily the correction for this effect is negligible; however, if the diaphragm has wrinkles, the polarization voltage might stretch them out and give an invalid frequency response curve. Attempts to run tests without the polarization voltage give signals that were too weak to measure.

Commercial Piston phone tests were also conducted and the frequency varied from 25 Hz to 500 Hz. These tests also gave a flat frequency response dropping off only at the low frequencies. The 2 db down point was usually around 50 Hz.

It was unfortunate that it was not possible to obtain high frequency data with this method.

Tape Recorder Flutter

Flutter from mechanical transport of the tape had a large component at about 10 Hz. A typical spectrum analysis of a flutter signal is shown in Fig. 27. Fig. 27 is an analysis of a recording made while shortening the input so that only the FM carrier center frequency is recorded. At one point in the program the recorder representative was called out to replace some of bearings and adjust the tape transport mechanisms. In the last stages of the experimental program the recorder had periods of several seconds where grinding noise could be heard. After the program was completed trouble with the recorder continued and it was finally sent back to the factory for a complete overhaul. The flutter signal of Fig. 27 was made after the overhaul and represents a recorder operating at .015 volts rms which is close to the flutter magnitudes measured during the test program. Tape recorder flutter was suspected of contributing to the measured pressure spectra. Below 50 Hz, however, the level of the flutter spectrum is too low to allow a significant contribution.

Data Reduction

The tapes were processed by the Ames Research Center Hybrid Computer facility. The analysis is essentially an analog processing from a 50 sec tape loop. The filter bandwidths used over the various ranges were:

RANGE	BANDWIDTH
5-25 Hz	1 Hz
25-120 Hz	5 Hz
120-500 Hz	20 Hz
500-2400 Hz	100 Hz
2400-5000 Hz	200 Hz
500-10,000 Hz	400 Hz

The data on the first sequence of flights were transcribed from the flight recorder to a new tape which was forwarded to Ames. Data for flights 62 and later flights were processed at Ames using the original tape on which the data were recorded.

Spectra for flights 56 through 59 (files 3924 through 3935) were processed with nominal values of microphone sensitivities and boundary layer parameters. Correction factors for the actual values are listed in Table 15.

Processing of flights 62 and later flights was done during one period of time. The first files in this series

are invalid (Files 4517, 18 and 19). Subsequent files have an amplifier correction. For some unknown reason the Ames tape recorder used in the Hybrid system could not amplify properly a calibration tape made on the Leach 3200 flight recorder. The issue was resolved by playing the tapes with a reproduce amplifier gain of 0.75. A compensating gain correction was then made in the digital computer processing so the spectra have the proper gain factor, and the values for C_p integrated from PSD are thus correct. The rms values read from a meter on the tape loop, called C_p loop, must be divided by .75 to correct for the amplifier gain.

Beginning with files 4520 the Ames tape recorder was played at 60 ips whereas the data was recorded at 30 ips. This gives better bandwidths at the low frequencies. It also causes a displacement of the PSD spectra. Doubling the speed has the effect of moving the spectra to double the frequency and reduces the magnitude by a factor of 2. Thus the spectra in files 4520 through 4563 should be increased in magnitude and reduced in frequency by a factor of two. Because of the frequency shift the computer applied the wrong Corcos corrections and all data with this correction are incorrect.

IV. RESULTS

Two sets of experiments were conducted; single point measurements and array measurements. In the single point measurements a single microphone was mounted in the instrument plug at station 80 (see Fig. 20). The boundary layer traversing probe was placed about 3 inches downstream in the adjacent instrument plug. The purpose of these tests was to determine the pressure spectrum while simultaneously measuring the boundary layer properties. Three different microphone sizes were used with both tripped and untripped boundary layers.

Spatial correlations were measured with two different configurations of ten microphones. Boundary layer measurements were not taken simultaneously in these tests. The boundary layer was tripped to minimize growth effects and have a well-established layer throughout the region. Array number one has the microphones clustered at the aft instrument bracket as shown in Fig. 20. Array number two, shown in Fig. 21, has the microphones clustered at the forward location.

Root-Mean-Square Values

Three different root mean square values are tabulated in Table 14 as $C_{px} = v p^2 / q$. The first, C_{pT} , was measured

immediately after the flight with a Ballantine True RMS meter. The second, C_{pI} , is the numerical integration of the power spectral density curve. It is an indicator to check the PSD computation. The third, C_{pL} , is the meter measurement made on the tape loop during the data reduction. It is considered the most accurate.

Some files need a correction applied to C_{pL} . When the original tapes were played at Ames to form the tape loop, the reproduce amplifier was set at a gain of 0.75. This was set up using a calibration tape made on the Leach flight recorder. When the spectrum was processed a compensating change in the microphone sensitivity figure was made. However, the tape loop rms values were not corrected and all C_{pL} values on files numbered 4520 and higher need to be divided by 0.75.

Experimental measurements of the rms pressure signal are frequently nondimensionalized by the dynamic pressure since it is easily measured. Since many of the turbulence properties scale with the wall shear stress many workers feel that it should be used to give a quantity which would be more independent of the Reynolds number; that is $C_{px}/C_f = v_p^2/\tau_w$. The shear stress coefficient C_f levels out at the higher Reynolds numbers, c.f. Fig. 24, and then the distinction

is not too important. Our tests were run at small or moderate Reynolds numbers and it is possible to investigate the merits of using q or τ_w to scale the data.

On a given flight, the three consecutive runs at different airspeeds offers a set of data taken with the same microphone and simultaneously recorded boundary layer information while the Reynolds number changes. Fig. 29 gives data for C_{pL} taken with three different microphone sizes. Flight 58 is not plotted since this microphone had a loose cap and the calibration is uncertain. There is a general downward trend in C_{pL} as the airspeed (or Reynolds number) is increased. One might suspect that this is an effect of microphone size; however, this is not true. As the airspeed increases the transition moves forward and makes the boundary layer thicker at the measuring station. This causes d/δ^* to decrease which means one should measure more of the actual rms. Due to this effect the curve would increase slightly with airspeed.

The companion graph on Fig. 30 gives the rms non-dimensionalized by the shear stress (C_{pL}/C_f). There is no apparent trend of these curves with airspeed and it appears that τ_w gives a slightly better correlation.

Because the microphone size parameter d/δ^* causes a great influence on the data it is instructive to plot C_{pL}

vs. d/δ^* as in Fig. 31. In addition to the data plotted previously all of the other single point and array experiments taken at 60 mph are shown. There is considerable scatter, however, the data trend is toward $C_p = 5 \cdot 10^{-3}$, a value often thought of as the lowest level for incompressible flow. The corresponding plot for C_{pL}/C_f is also shown in Fig. 32. The data show slightly less scatter, especially for runs on the same flight, and trend toward a value of ≈ 1.9 . Most other experiments yield a value a little above 2. The evidence that C_{pL}/C_f gives a better correlation than C_p is not overwhelming; however, it will be supported by the same trends in the power spectra.

Power Spectra

The power spectra as they were plotted at Ames usually have been processed with rough estimates of the boundary layer parameters and need to have multiplicative scaling corrections applied. In some cases the processing procedures caused further scaling changes. The final scaling changes have been tabulated in Table 15.

The processing was done in two batches; flights 56, 57, 58, 59 and flights 62, 63, 80, 81, 92, 93, 95, 96. The first batch has to be corrected for slightly inaccurate

values of velocity V , dynamic pressure Q , and length parameter L . The second batch need corrections for L and for tape speed. The original data was taken at a tape speed of 30 inches per second. The same tapes were taken to Ames and processed at 60 ips. This causes the spectrum to shift to higher frequencies by a factor of two and to decrease in magnitude by a factor of two. The integral of the spectrum is unchanged.

The power spectra will be given in two sets of coordinates, $GV/Q^2\delta^*$ as a function of $F\delta^*/V$ and $GV/\tau^2\delta$ as a function of $F\delta/V$. The integral of the spectrum in the first set of coordinates is C_{pI}^2 whereas it is $(C_{pI}/C_f)^2$ in the second set.

The spectra for three different indicated airspeeds (data taken on one flight in each instance) are shown in the next four figures. Figure 33 gives data taken with a 1/4 inch diameter microphone, Fig. 34 the 1/2" microphone, Fig. 35 the 1" microphone, and Fig. 36 the 1/2" microphone with a tripped boundary layer. The spectra all show some irregularity at low frequencies, rise fairly smoothly to a peak and then fall off as the microphone size becomes comparable with the eddy size. The fall off at low frequencies is definitely verified.

The source of the irregular plateau at low frequencies is not known definitely. It is suspected that the plateau is not boundary layer noise but a phenomena which has a constant rms irrespective of the test condition. In the next several paragraphs we digress to discuss this possibility in detail. If the extraneous signal is restricted to a certain bandwidth and its rms is constant, then the spectrum level is given by

$$\frac{GV}{Q^2\delta^*} = \frac{\text{rms}^2}{S} \frac{1}{Q^2} \cdot \frac{1}{\Delta(F\delta^*/V)}$$

where S is the overall sensitivity of the microphone circuit. From the expression we can see how the extraneous signal level should change with indicated airspeed and microphone size. As the airspeed increases both Q^2 and δ^* increase, thereby reducing the spectrum level. Typical numbers show that the extraneous signal spectrum level at 55 mph would be 2.1 times the spectrum level at 65 mph. This trend is observed in the figures.

The overall sensitivity of the circuit also affects the extraneous signal spectrum level. The microphone circuits had sensitivities of 1360, 1260, and 1630 volts/psi for the 1/4, 1/2, and 1 inch diameter microphones, respectively. This means that the level for 1/4" should be 1.43 times that for the 1". This trend is also observed.

Another difference should be observed for the tripped vs. untripped layer at the same airspeed. The change in δ^* should cause the tripped extraneous signal level to be approximately .7 of the untripped level. There is also an equivalent shift in the frequency parameter $F\delta^*/V$. This trend is observed in Figs. 36 and 37.

The irregularity in the low frequency spectra makes it hard to definitely conclude that the plateau is an instrumentation problem. If it is actually associated with the turbulent boundary layer one would expect it is not to usual turbulence-meanshear interaction but another phenomena.

Now we return to the effect of airspeed on the PSD's as shown in Figs. 33 through 36. The boundary layers for the three different airspeeds were all typical of a zero pressure gradient layer. In general we can view the different airspeeds as simply changes in the boundary layer Reynolds number, despite the fact that the tuft studies of flow direction show that the 65 mph run has a small crossflow component.

The rising portion of the spectra and the peak region are valid measurements. The spectra tend to drop with increasing airspeed when Q and δ^* are used to nondimensionalize the data. The use of τ and δ gives a better correlation on all four figures. This is consistent with the previous

conclusion that C_{pL}/C_f gives a better correlation than C_{pL} . The high frequency roll off should occur at different places according to the microphone size correction. This changes very little with airspeed but the lower airspeed should roll off slightly sooner.

Tripped and untripped data are compared for the 1/4" and 1/2" microphones in Figs. 37 and 38. The 1/4" data do not have the right trend at high frequencies. Tripping the boundary layer thickens δ^* by about 50%. This will give a smaller d/δ^* and thus a more favorable microphone size correction, which in turn makes the tripped data to roll off more slowly. The curves would have this trend if they could be moved relative to one another. An error in δ^* or V would cause a spectrum to slide along a 45° line from upper left to lower right. Such an error is suspected. One should also note that the recorder flutter level is lower for the tripped data as anticipated.

The 1/2" microphone curves on Fig. 38 give a much more satisfying comparison. The curves have the expected trends in every respect in the Q, δ^* coordinates, but move apart when the τ and δ are used as nondimensionalizing parameters. This is just opposite of what was found when the Reynolds number was varied by changes in the airspeed. When

one reviews the values of the friction coefficient, which essentially causes the curves to separate, one finds that the tripped data is somewhat low and the untripped data slightly high compared to Wieghardt's data at the same Reynolds number.

	C_f measured	C_f Wieghardt
Tripped	$2.78 \cdot 10^{-3}$	$2.86 \cdot 10^{-3}$
Untripped	$3.25 \cdot 10^{-3}$	$3.20 \cdot 10^{-3}$
Ratio squared	1.36	1.25

Since C_f^2 is involved in transferring data from the top graph to the bottom graph, the separation would be slightly less if we used Wieghardt's data rather than our own.

Another thing that should be pointed out is that the curves probably should not lie exactly together on either graph. The boundary layer data for the tripped and untripped layers showed distinct differences in the wake component Π . Since the shear stress vs. Reynolds number curve is different for each value of Π and since the spectrum should also be different for each value of Π , we should not expect exactly the same spectra. It is not possible to conclude from the data at hand exactly what the differences should be, although a higher Π gives a higher spectrum, and the data shown here is in qualitative agreement with this fact.

All of the previous data was taken with a single microphone located at station 80. In order to show that the flow field has longitudinal and transverse uniformity, Fig. 39 was constructed. It shows the spectra from four 1/2" microphones located forward (20 inches), on each side (4 inches), and aft (10 inches) of the single point measuring location, station 80. These data were taken from the spatial array tests and boundary layer properties estimated. Except for different roll off rates because of the boundary layer growth changing d/δ^* , the spectra are fairly consistent. The aft microphone is somewhat low.

Typical untripped spectra at 60 mph are plotted in Figs. 40 and 41. The effect of microphone size is evident in Fig. 40 and Fig. 42 and the Corcos correction computed by hand has been applied. The curve was arbitrarily stopped when the correction became 90% of the level. Original data with Corcos correction included in the processing at Ames was in error because of the artificial doubling when the tape was played at 60 ips.

Corcos correction works reasonably well in collapsing the curves. The larger microphones curves are somewhat sensitive to the numbers used for the diameter. Since the "effective" diameter should be used in the calculation, the

correction is somewhat uncertain for large microphones. These spectra on these curves are probably the most accurate of any of the current measurements and the peak and high frequency end are in agreement with previous experimenters.

The spectra for the spatial correlations were not nearly as good as the single point measurements. The 1/4" microphones changed calibration during the program primarily due to mechanical damage. The next three figures show how the 1/4' mic spectra changed during the four spatial correlation flights. The coordinates are uncorrected since the curves are only for comparison on the same graph. The high frequency roll off is usually consistent. The differences that exist can usually be traced to the fact that the microphones were moved to a new location between flights 93 and 95. The low frequency results show drastic changes from flight to flight and are considered inaccurate. Almost all microphones gave reasonable results on flight 92 but by the end of flight 96 they were practically all damaged.

The 1/2" microphones on the other hand were fairly consistent, Fig. 44. Microphone #4 gave a high low frequency end to the spectra on flight 95 but otherwise the spectra are consistent and in agreement with the single point measurements. The low frequency content of microphone #3 is

somewhat higher than the other microphones. This is attributed to a surface bump about 7 inches forward and only slightly off line with the microphone. The bump was formed by a row of 5 rivets heads for the seat belt attachment. The rivet heads were filled in and covered with modelling clay to about twice their height. Microphone #3 was the only microphone whose spectrum changed when the clay was added so we conclude that it was the only location whose spectrum would be affected by the rivets.

Cross Power Spectra

The spatial array consisted of six 1/4" microphones and four 1/2" microphones. Unfortunately the power spectra from the 1/4" microphones show progressive changes as the flight program progressed. Nevertheless some useful information may be obtained when the data is presented in the form of the coherence coefficient.

The cross-power spectral density may be split into real and imaginary parts,

$$G_{xy} = C_{xy} - i Q_{xy}$$

This can be represented in a polar form using the coherence function defined by

$$\gamma_{xy}^2 = \frac{|G_{xy}|^2}{G_x G_y}$$

An important aspect of the coherence function is that it is normalized by the power spectrum of each record. It is possible to prove that the coherence function is independent of the frequency response curve of the transducer. This is true providing the transducer is still behaving as a linear system.

Some types of microphone damage such as a loose cap or a slight abrasion probably still allow one to consider the behavior as linear. More severe damages which leave wrinkles or gouges in the diaphragm would probably produce nonlinearities. As remarked earlier the electrostatic actuator tests gave a fairly flat frequency response curve; however, these tests involve an artificial steady force on the diaphragm. Commercial piston-phone tests were also flat but had only a limited frequency range. All in all, the deviation of the PSD from previous measurements is probably the best indication of the condition of the microphone.

The other variable in the polar representation is the phase angle

$$\theta = \tan^{-1} \frac{O_{xy}}{C_{xy}}$$

The period of the tangent is π so there is an ambiguity of π in the θ computation.

The phase angle is more sensitive to the microphone condition than the coherence coefficient. If the frequency response curve shows a non-flat region, then there is theoretically a phase difference in the response. This is true even if the system is still linear.

It is customary to express the information contained in the phase angle as a convective velocity. The equation

$$\frac{U_c}{U_\infty} = \frac{2\pi}{\theta} \left(\frac{FL}{V} \right) \left(\frac{\xi}{L} \right)$$

defines the convective velocity, U_c , where ξ/L is the distance separating the transducers. The Ames computer frequency failed to produce curves of U_c/U_∞ . There were several reasons for this. First, the tape was played at twice speed which would give U_c/U_∞ twice its actual value. This tended to boost the values out of the plot range. Second, the computer was trying to pick the quadrant for θ at the low frequencies where the microphones show the most erratic response. Third, the erratic response of the microphones themselves indicates θ may be erroneous.

The coherence data is plotted on Fig. 45 for small microphone separations and Fig. 46 for larger separations. The two curves at the smallest separations show a high contribution in low frequency decade. The microphones in each of

these correlations were in the same instrument plug whereas all other correlations are between microphones in separate mounts. The low frequency correlation may be an extraneous signal resulting from this fact. Another possible explanation would be a slow wandering of the sublayer which does not correlate over long distances.

The remaining curves show a small erratic coherence below $F\delta^*/V \approx 5 \cdot 10^{-3}$. This corresponds to the level portion of the PSD plots. The left side of the peak holds about the same shape as one progresses to larger separation distances. These frequencies correspond to the falling portion of the PSD curve since the peak in the PSD was about $F\delta^*/V = 6 \cdot 10^{-2}$. As expected, the high frequencies lose coherence rapidly with distance; at $\xi/\delta^* = 33$ ($\xi = 5.5$ inches) all eddies which produced the right side of the PSD have decayed. After about $\xi/\delta^* = 22$ the decay changes its character somewhat. The coherence coefficient decays in value but seems to cover the same bandwidth. The initial stages would correspond to decay of the energy containing eddies and the second stage would correspond to the so-called large permanent eddies.

All curves on the large separation plot, Fig. 46, have been adjusted for boundary layer growth. A simple average of the δ^* at the two locations was used. At $\xi/\delta^* \approx 40$

and again at 50 there are two curves, one solid and one dashed. The dashed curve is from transducers in the front portion of the measurement region where the boundary layer is thinner. A large eddy born in a thin layer may persist into the thicker region of the boundary layer but it is no longer as large when scaled by the local boundary layer thickness. Thus there is a tendency for the low frequency end of the dashed correlations to be low. From another point of view these curves give an idea of the influence of the boundary layer growth on our results.

Persistence of the large eddies is illustrated in another way in Fig. 47. Maximum coherence is plotted vs. distance. The maximum coherence coefficient is always in the low frequency portion of the PSD so this is essentially a plot of the large eddy decay.

Convective velocities would complete the picture; unfortunately these data are probably no good. Figure 48 displays three graphs with narrow-band convective velocities at various separation distances. These data were computed by picking the phase angle from the Ames data and using the formula previously given. One expects a low convective velocity at small separations, say .5-.6, with possibly a slight decrease with frequency. The curve at $\xi/\delta^* = 3.3$ is

reasonable. Increasing the separation should give higher velocities but the curve at $\xi/\delta^* = 6.8$ drops. All the curves from 21.9 on show a reasonable consistency. The trend toward low values at low frequency is not explained although Wills has suggested such a tendency (based on one data point).

The reason we put such little faith in the data is shown by the dashed lines. At $\xi/\delta^* = 11.7, 51.5,$ and 54.2 two calculations were made and both are shown. These calculations had the phase angle changed by 180° . Recall that this is the ambiguity in the arctangent function in the calculation. This illustrates how the calculation changes with a change in the phase angle. Since the PSD's showed some damage to the microphones, which probably changed the phase angle, we do not think this data is valid.

V. SUMMARY

The static pressure survey located a region of constant pressure on the cylindrical portion of the forward fuselage. The region was about 40 inches long and 10 to 15 inches wide. Pictures of tufts taken from another airplane showed that the flow was aligned with the fuselage at the low airspeeds. Tests were conducted at 55, 60, and 65 mph for this reason.

The boundary layer velocity profile was measured at three locations using a traversing pitot tube. When transition to turbulence was natural, the aft measuring station had Reynolds numbers, Re_δ^* , of 4000 to 7000. This is moderately low compared to other test situations. The forward measuring station had a value around 2000-3000, which means the turbulent layer is very young. Shear stress at the aft position was typical of a classical zero pressure gradient layer but the wake strength, Π , showed a tendency to be low (.5) compared to a value of .6 now quoted for a high Reynolds number layer. The forward measuring location had a value around .2 which is the proper trend for a layer not far from transition.

When the boundary layer was tripped, both forward and aft locations had Reynolds numbers in the moderate range, 4000-9000, with fully developed turbulence. The wake strength

was now somewhat high and the shear stress correspondingly low compared to nominal values. The deviations were well within the range of experience encountered in typical test situations.

Microphone measurements gave rms values which tended toward $.005 \times q$ and $1.9 \times \tau_w$ when extrapolated to zero microphone diameter. These values are at the low end of previous results. The results showed slightly less scatter when normalized by τ_w . Since the tests were at moderate Reynolds number, there was a larger change in τ_w and a better opportunity to observe this trend. The power spectra of the fluctuations also gave slightly better correlation with different airspeeds and microphone diameters when normalized with τ_w rather than q .

The shape of the spectra was flat at very low frequencies ($F\delta^*/V \leq 6 \cdot 10^{-3}$; $F \leq 50$ Hz). There was a large scatter in this region and the source of these components is uncertain. The spectra then rose to a peak about $F\delta^*/V = 6 \cdot 10^{-2}$. The rise was almost proportional to F whereas some published theoretical conjecture would give F^2 . It may be that an F^2 region exists at the extreme low frequencies. The peak value is in agreement with other comparable experiments. Application of Corcos correction to three different microphone sizes gave reasonable correlation and a fall off rate corresponding to Willmarth's data.

The small 1/4 inch diameter microphones were susceptible to damage and gave erratic spectra as the program continued. Spatial correlation tests were conducted primarily with these microphones. Of the four flights for which data was reduced, only the first was good enough to analyze and report. The convective velocities on this flight are thought to be erroneous because of phase errors introduced by the microphones. On the other hand, the coherence coefficient is unchanged by a frequency response change and this data is fairly good.

The coherence coefficient curves show two types of change as the separation distance increases. At first, the high frequencies decay and the peak lowers while the low frequency side of the curve remains nearly the same. This is characteristic of the energy containing eddies. After frequencies higher than the peak PSD frequency have decayed, the second type of decay begins. In this decay the bandwidth of the coherence is about the same while the level continues to decrease. This may characterize the large "permanent" eddies. The nondimensional frequencies for the correlation tests are lower than usual experiments have achieved and it is unfortunate that a complete set of data with convective velocities was not obtained.

REFERENCES

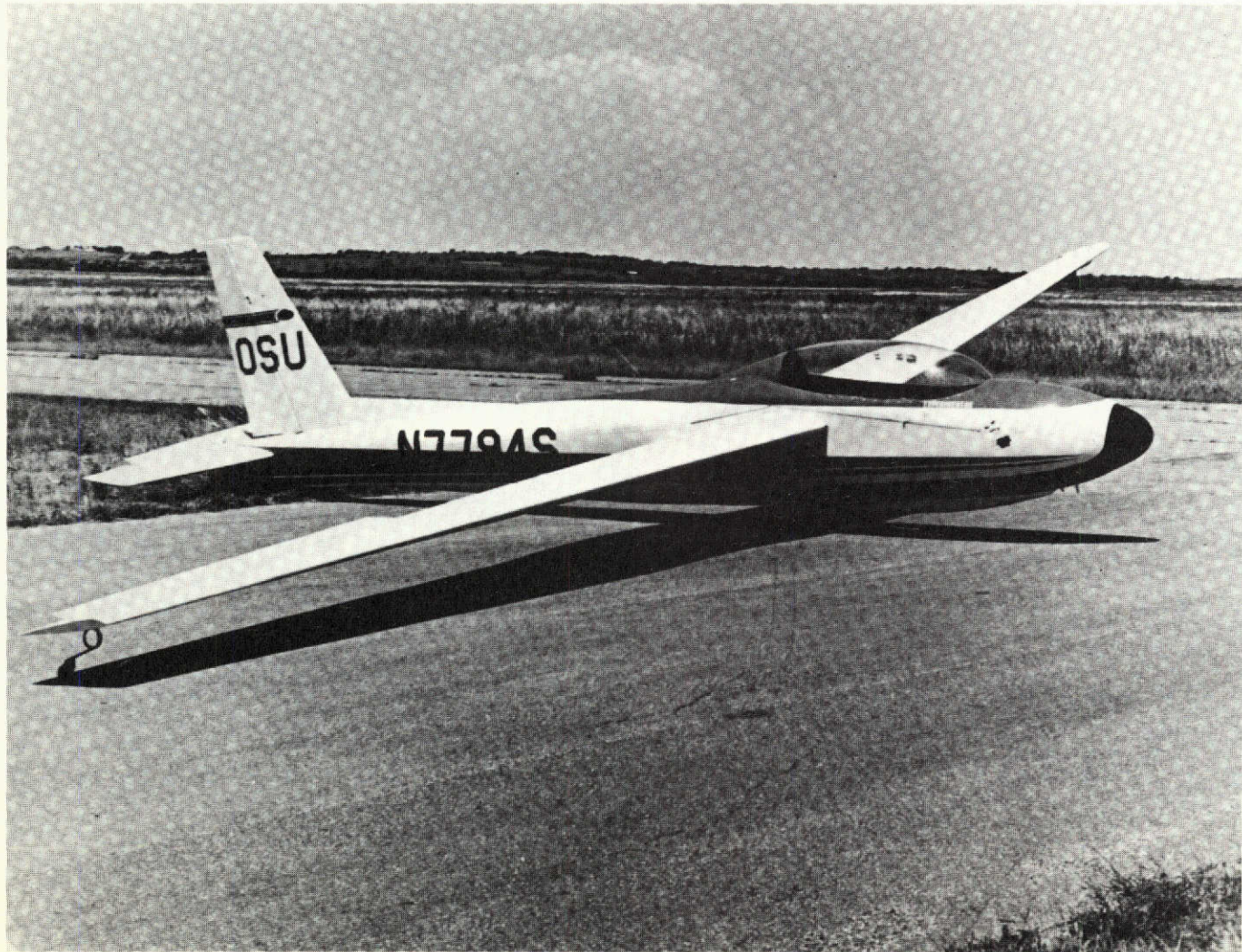
1. Hodgson, T. H., "Pressure Fluctuations in Shear Flow Turbulence," Ph.D. Thesis, University of London, 1962.
2. Proceedings, AFOSR-IFP-Stanford Conference on Computation of Turbulent Boundary Layers. Volume Two, D. E. Coles and E. A. Hirst ed. Stanford University publisher.
3. Wieghardt, K. and Tillmann, W., "On the Turbulent Friction Layer for Rising Pressure," NACA TM 1314 (1951). Also see Ref. 2.
4. Wills, J. A. B., "Measurements of the Wave-Number/Phase Velocity Spectrum of Wall Pressure Beneath a Turbulent Boundary Layer," JFM, 45, 1, pp. 65-90 (1970).
5. Lim, R. S. and Cameron, W. D., "Power and Cross-Power Spectrum Analysis by Hybrid Computers," NASA TMX-1324 (1966).
6. Willmarth, W. W. and Wooldridge, C. E., "Measurements of the Fluctuating Pressure at the Wall Beneath a Thick Turbulent Boundary Layer," JFM 14, 2, pp. 187-210, 1962.

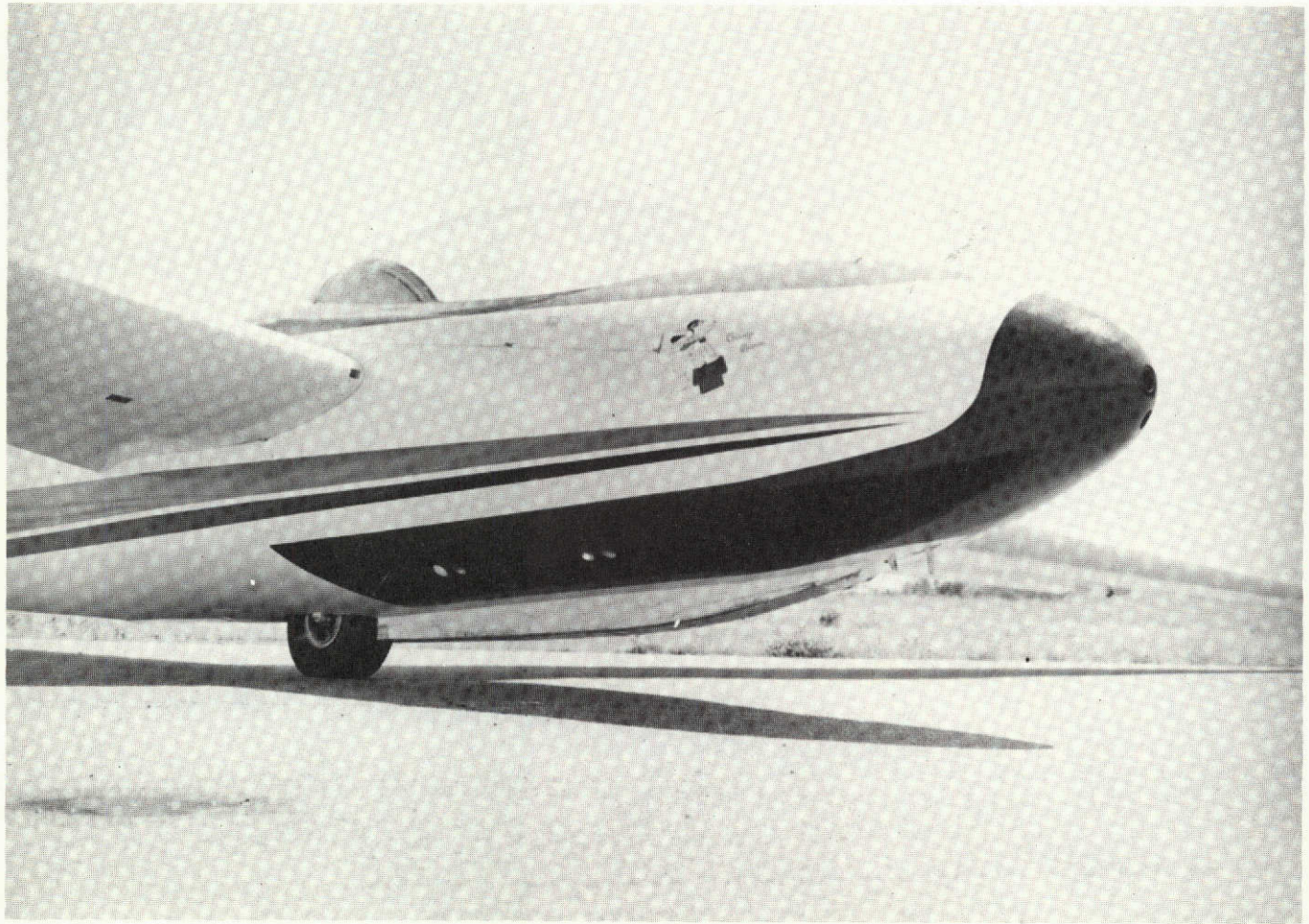
LIST OF FIGURES

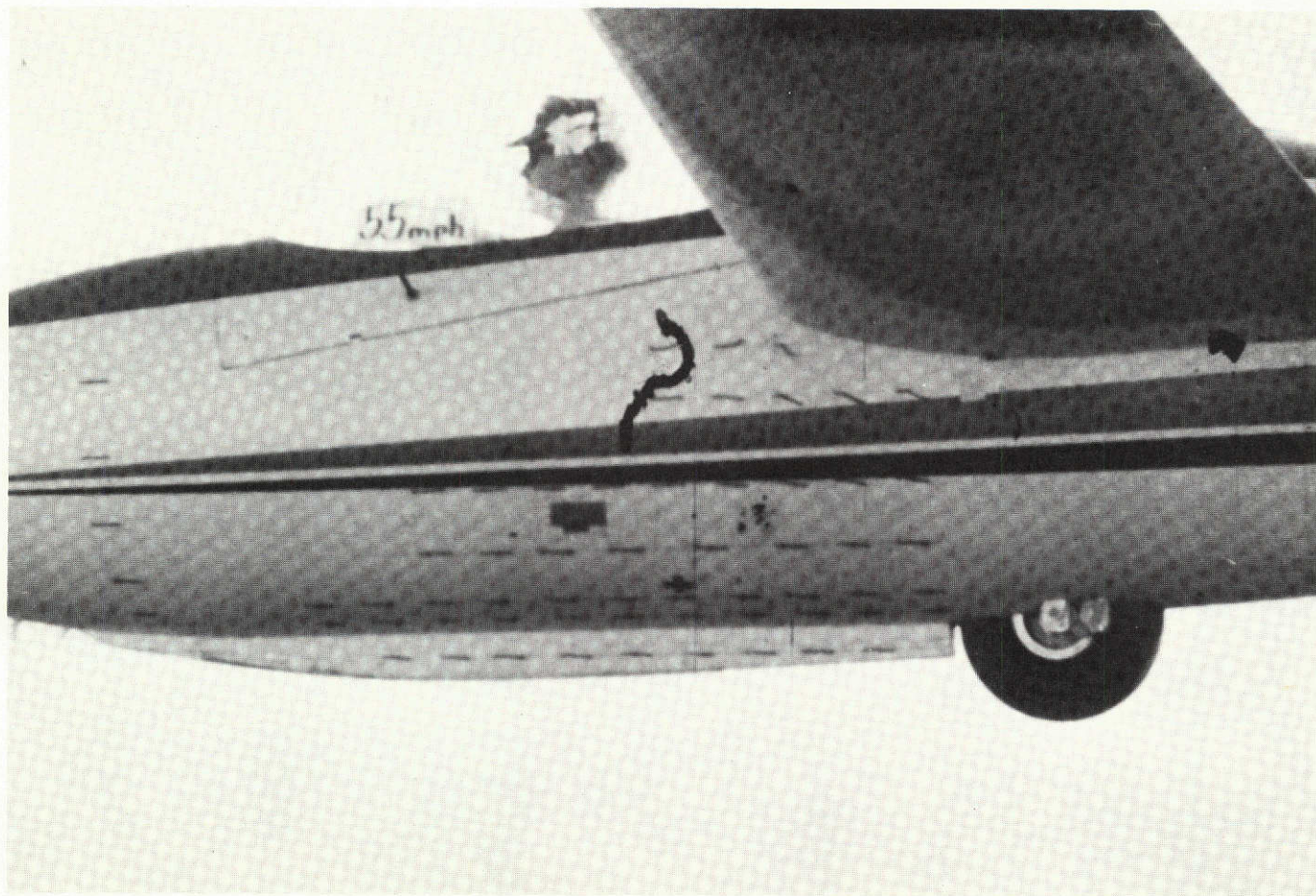
1. Schweizer 2-32 Sailplane
2. Instrument Location
3. Tuft Study of Fuselage Flow
4. Pressure Survey Tap Locations
5. Typical Manometer Record
6. Pressure Coefficient, Rows A & B
7. Pressure Coefficient, Rows C & D
8. Pressure Coefficient, Rows E & F
9. Pressure Coefficient, Columns 1, 2, 3
10. Pressure Coefficient, Columns 4, 5
11. Pressure Coefficient, Columns 6, 7
12. Pressure Coefficient on Measuring Streamline
13. Microphone Array No. 1
14. Microphone Array No. 2
15. Typical Boundary Layer Pitot Traverse
16. Boundary Layer Parameters, 55 mph
17. Boundary Layer Parameters, 60 mph
18. Boundary Layer Parameters, 65 mph
19. Displacement Thickness vs. Unit Reynolds Number
20. Friction Coefficient vs. Reynolds Number
21. Wake Parameter vs. Reynolds Number
22. Shape Factor vs. Reynolds Number

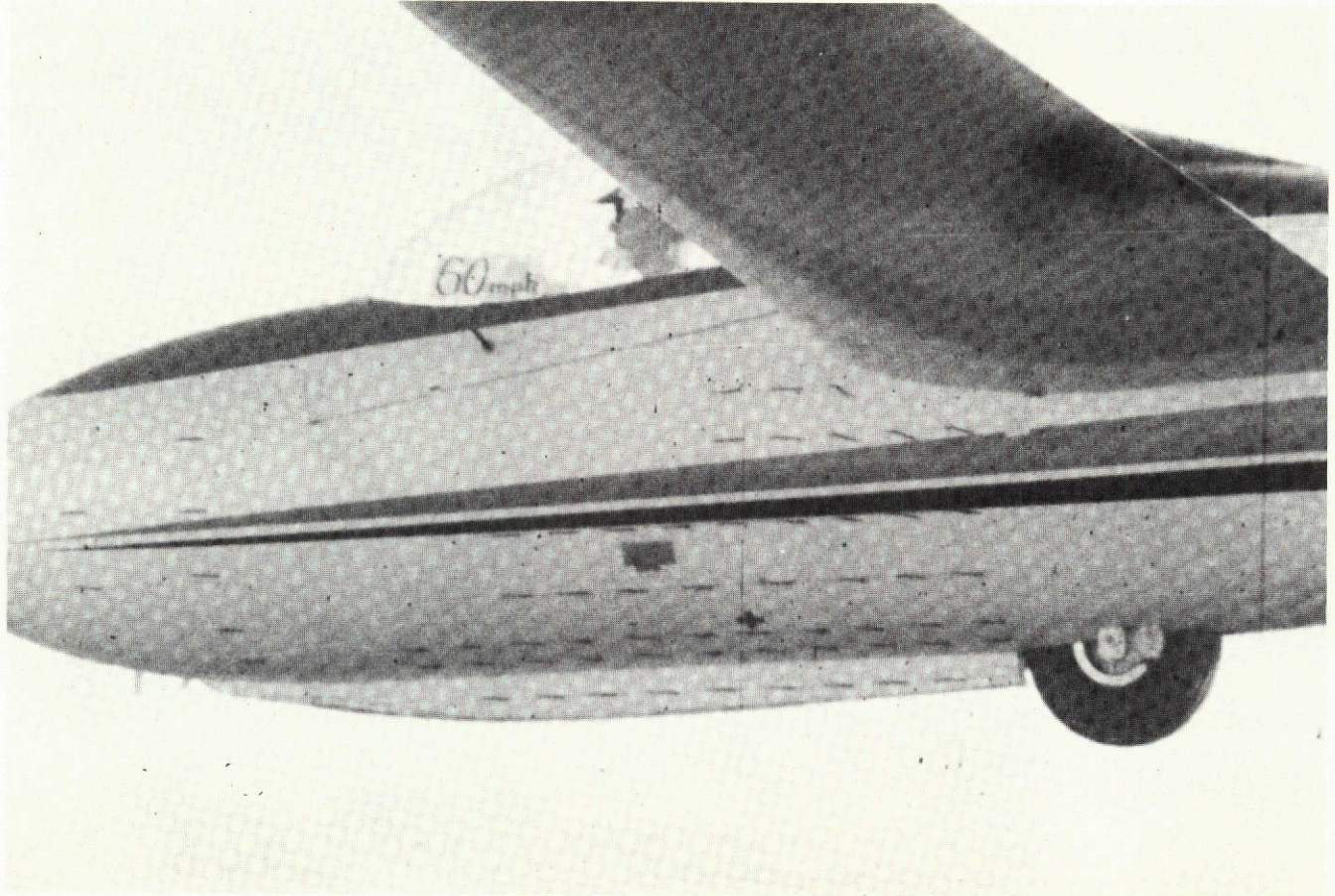
23. Microphone Test RMS Histories
24. Microphone Test RMS Histories
25. Microphone Test RMS Histories
26. Tape Recorder Flutter Spectrum
27. Tape Recorder Flutter Test Signal
28. RMS Results
29. C_{pL} vs. Indicated Airspeed
30. C_{pL} vs. Microphone Size Parameter
31. $C_{pL} C_f$ vs. Microphone Size Parameter
32. Power Spectra Correction Factors
33. Airspeed Effects on PSD, 1/4" microphone (Files 4523, 24, 25)
34. Airspeed Effects on PSD, 1/2" microphone (Files 3924, 25, 26)
35. Airspeed Effects on PSD, 1" microphone (Files 3933, 34, 35)
36. Airspeed Effects on PSD, 1/2" microphone, tripped BL (Files 3927, 28, 29)
37. Effects of Tripping on PSD, 1/4" microphone (Files 4524, 4527)
38. Effects of Tripping on PSD, 1/4" microphone (Files 3925, 3928)
39. Effect of Microphone Location on PSD (Files 4538, 4543, 3928)
40. Effect of Microphone Diameter on PSD (Files 4524, 3925, 3934)
41. Corcos Correction applied to Fig. 40.

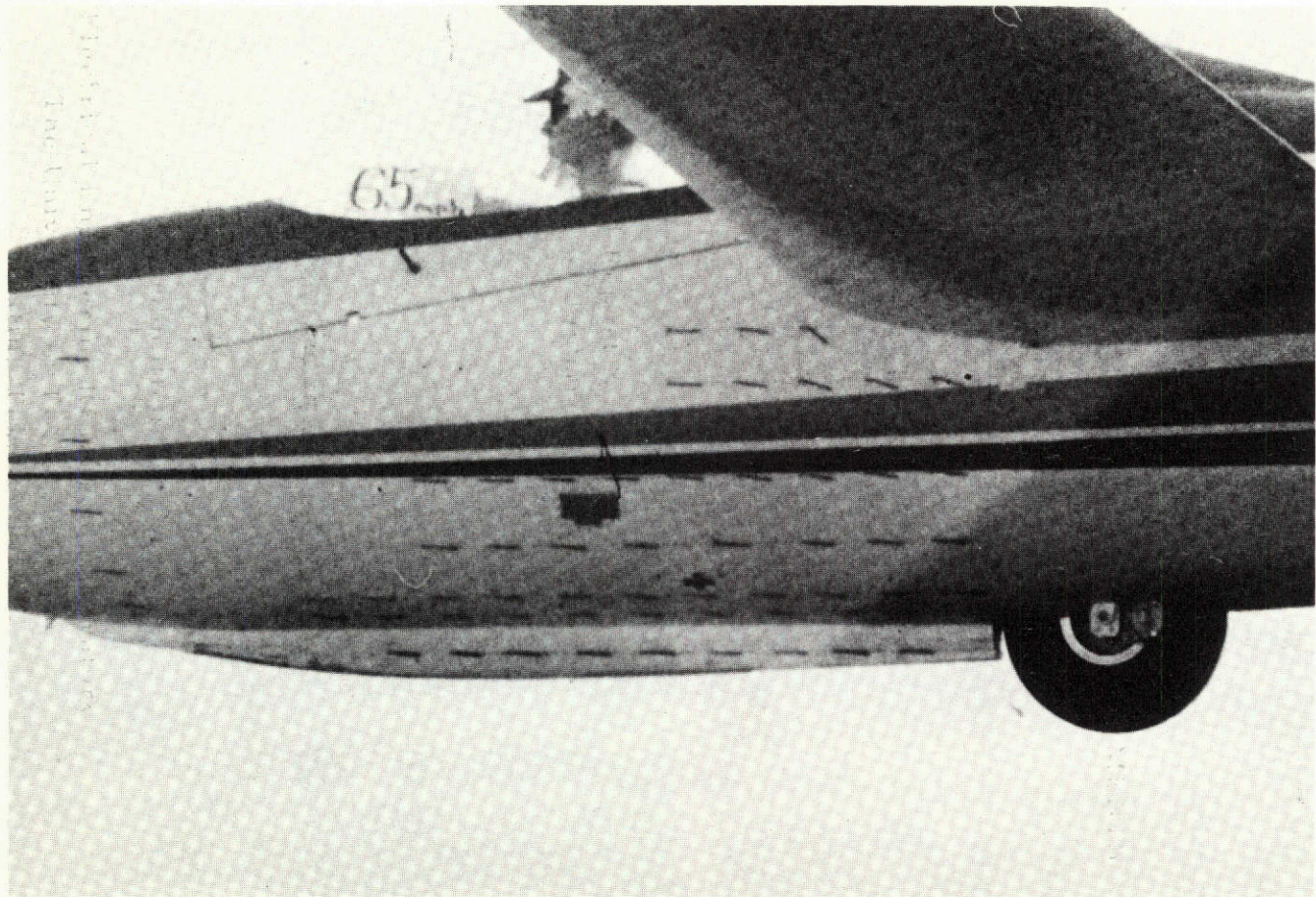
42. Microphone PSD Histories during Flights 92, 93, 94, 95
43. Microphone PSD Histories
44. Microphone PSD Histories
45. Coherence Coefficient at Small Separation
46. Coherence Coefficient at Large Separation
47. Decay of Maximum Coherence Coefficient
48. Convective Velocities

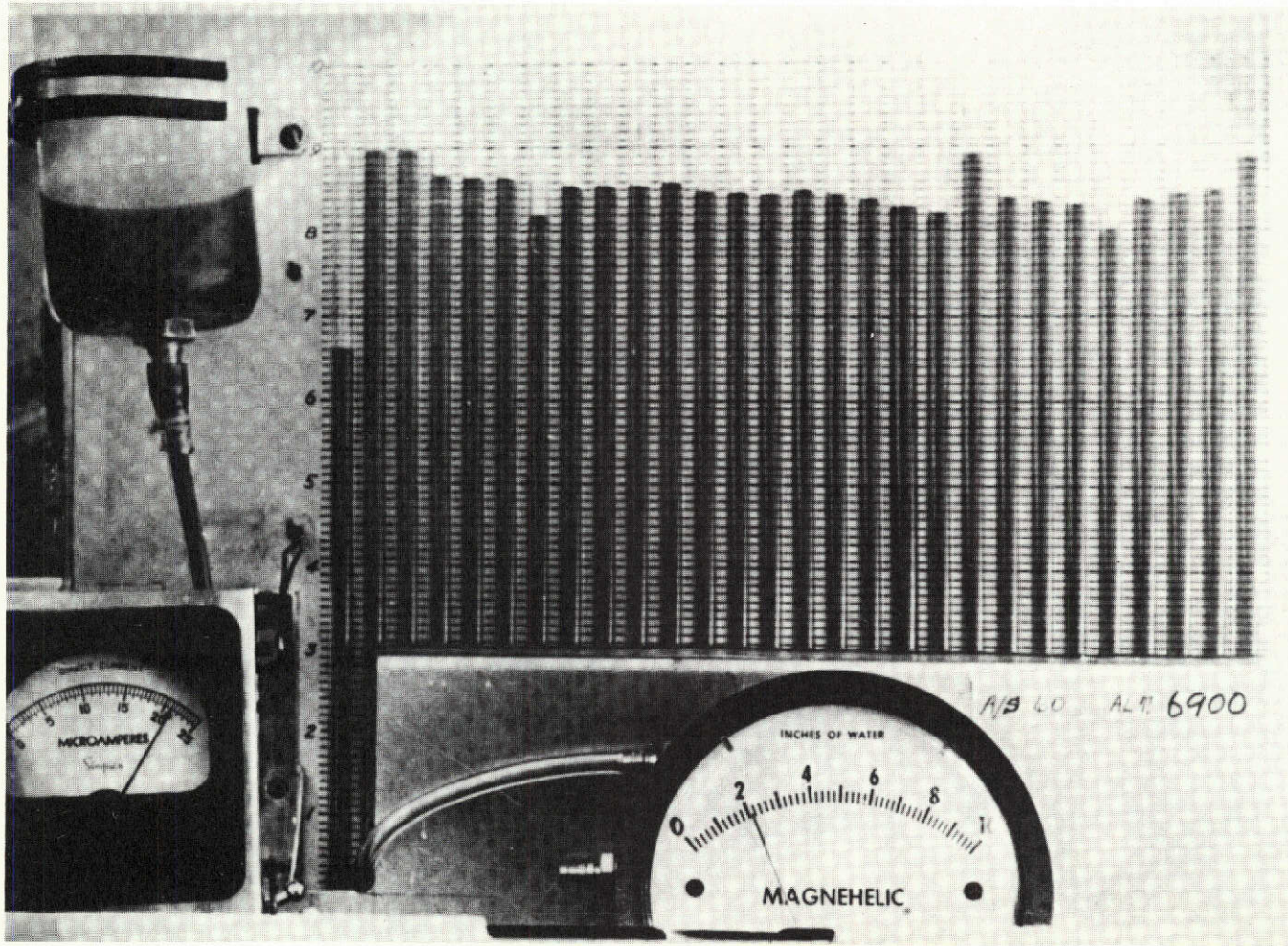












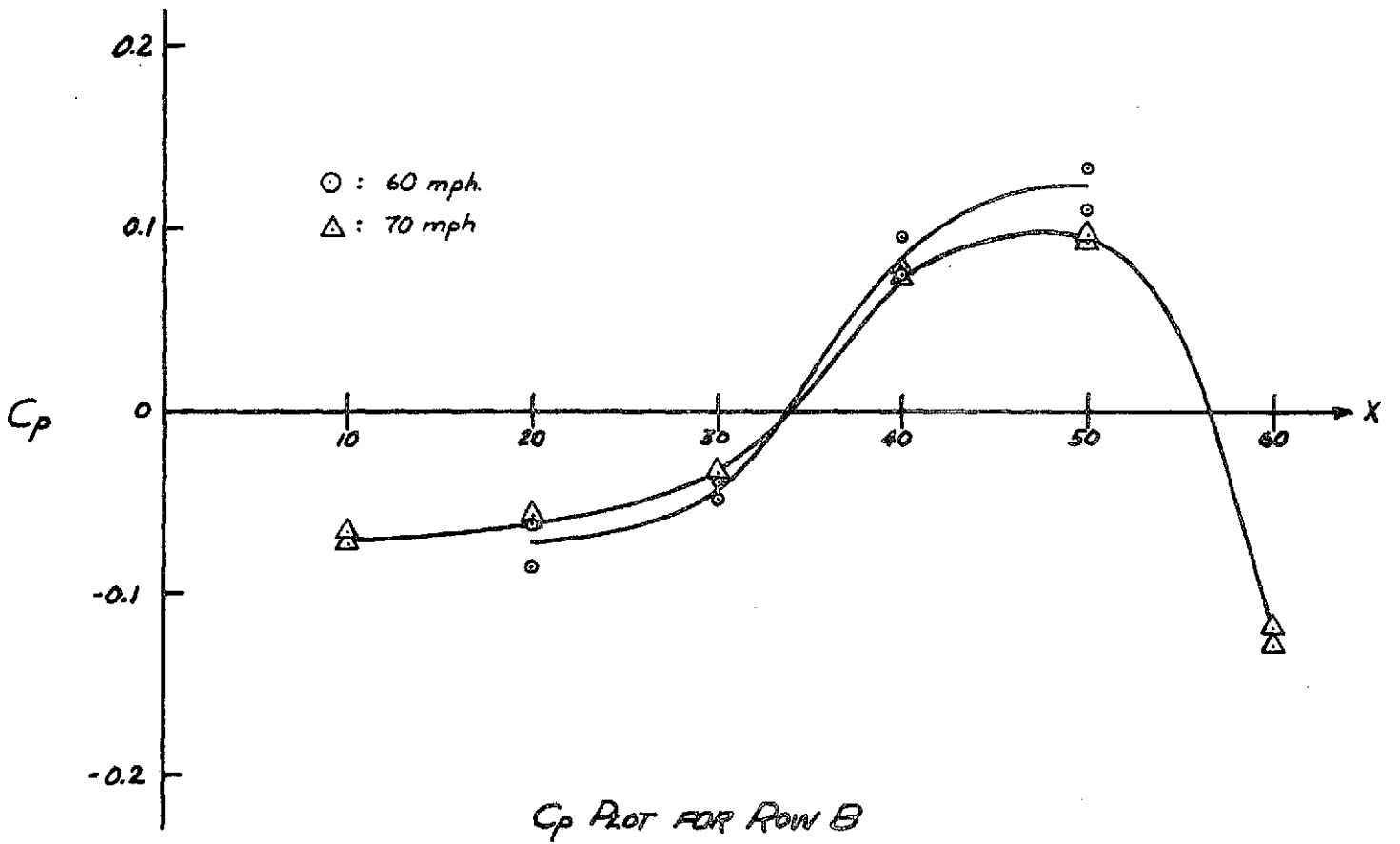
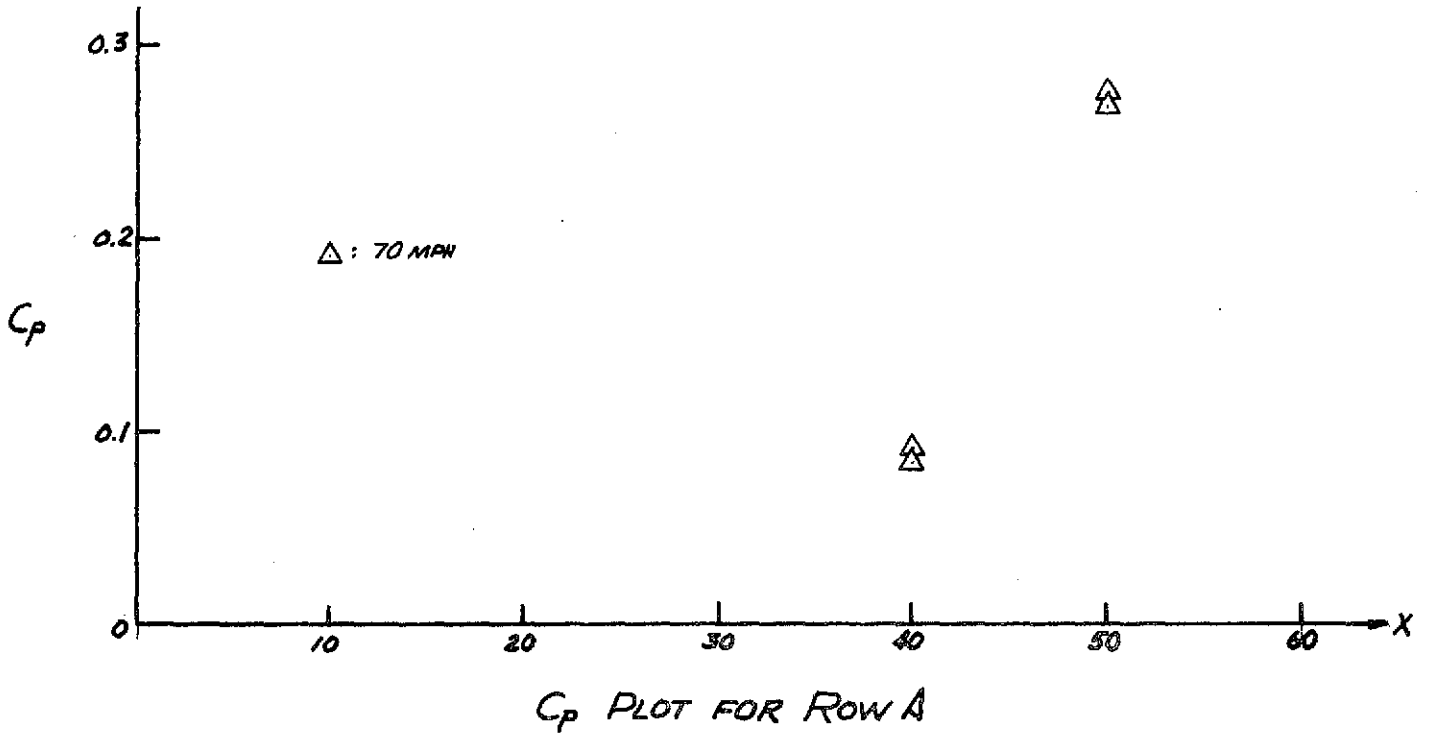
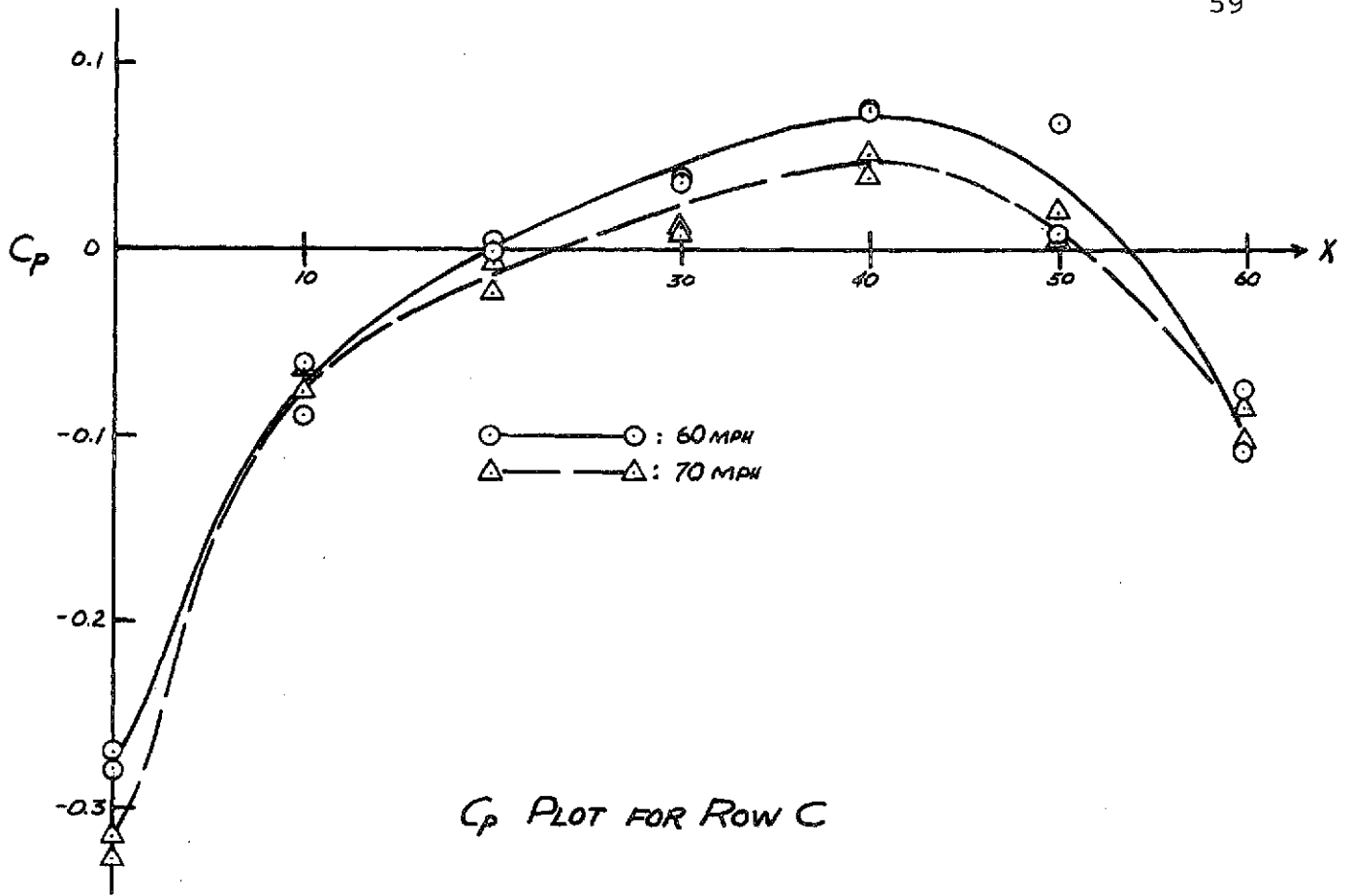
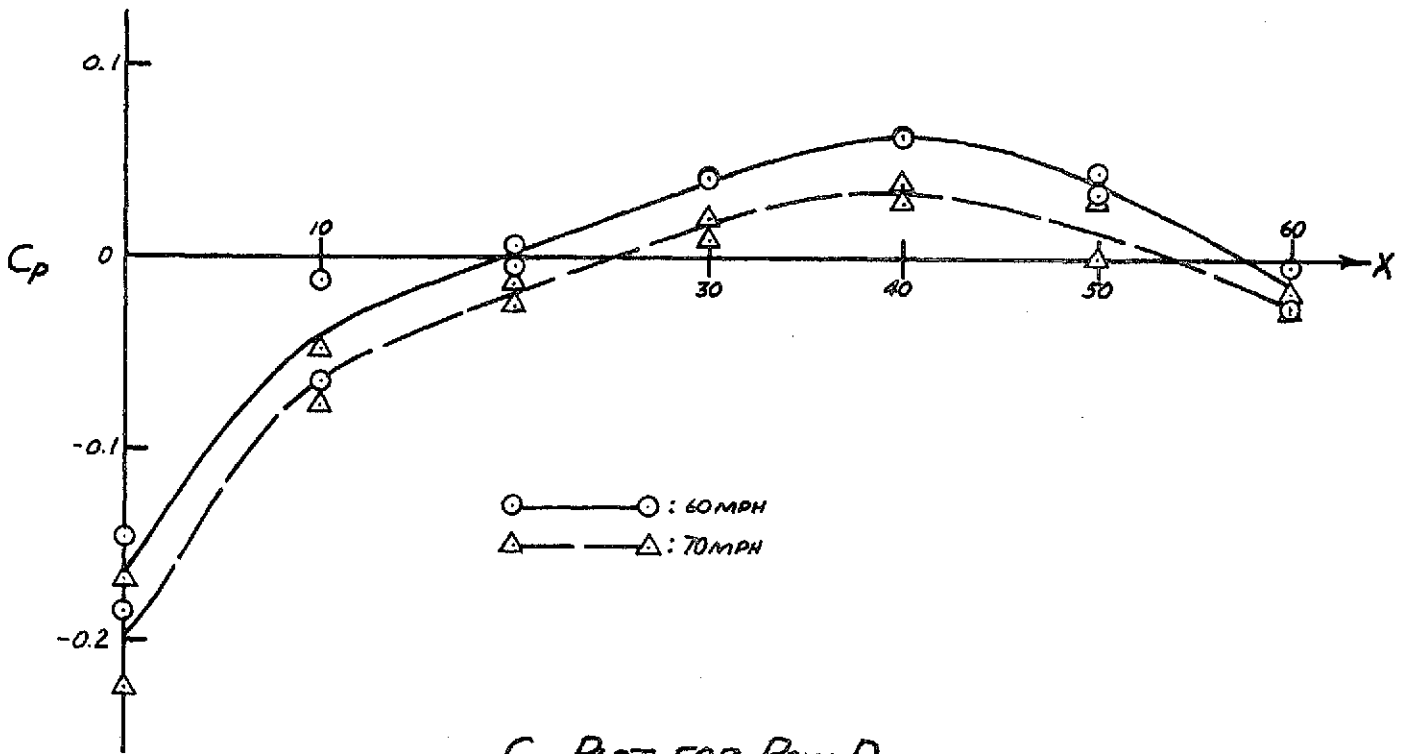


FIG. 6



C_p PLOT FOR ROW C



C_p PLOT FOR ROW D

FIG. 7

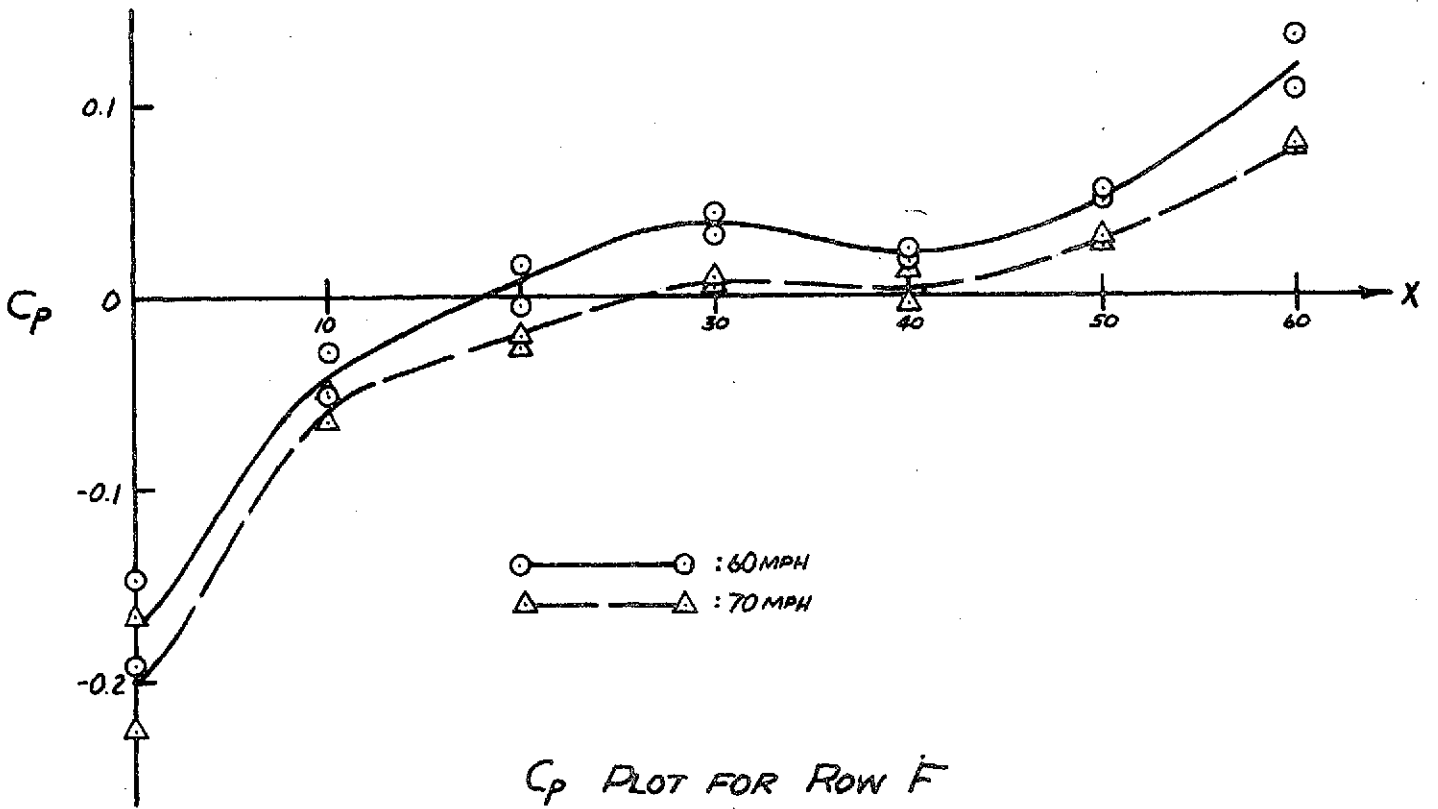
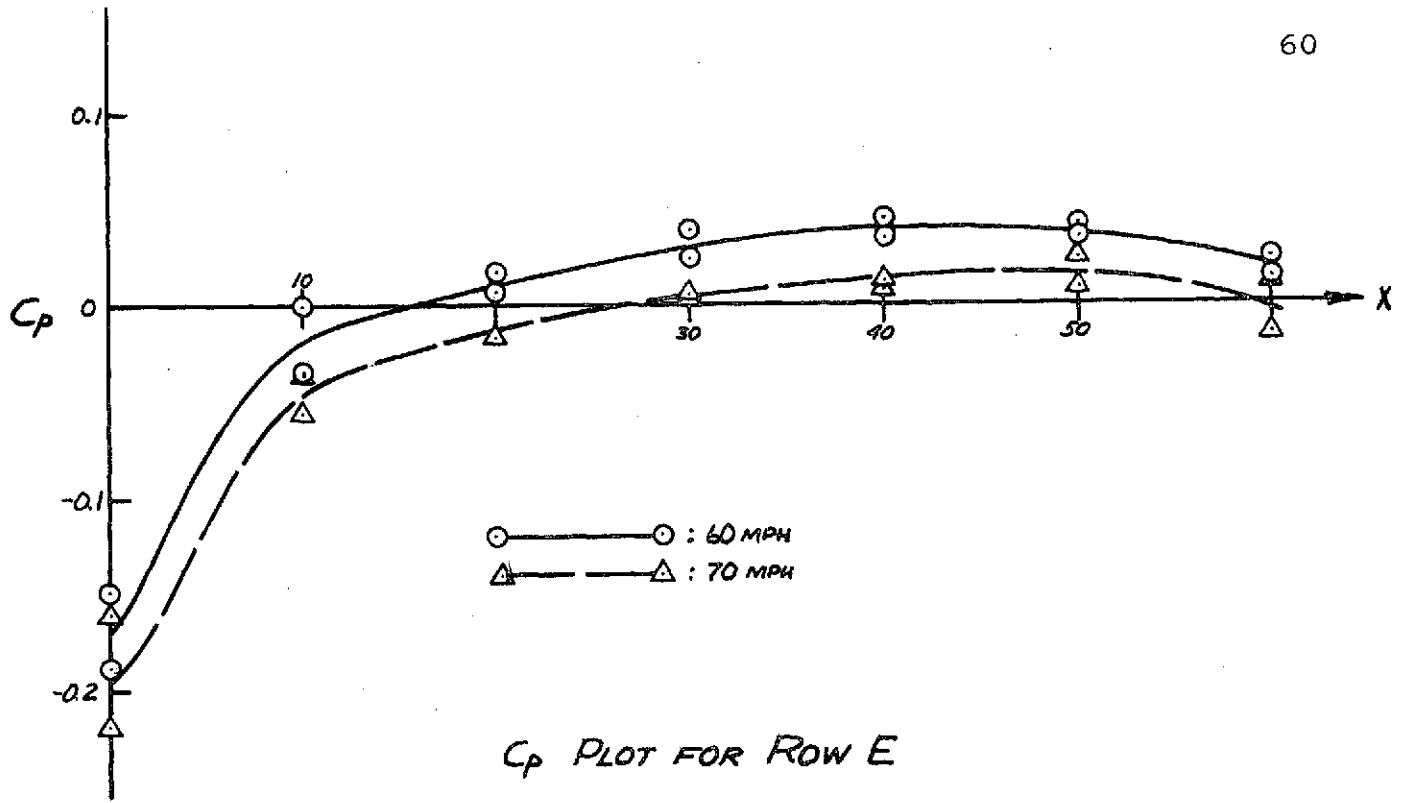


FIG. 8

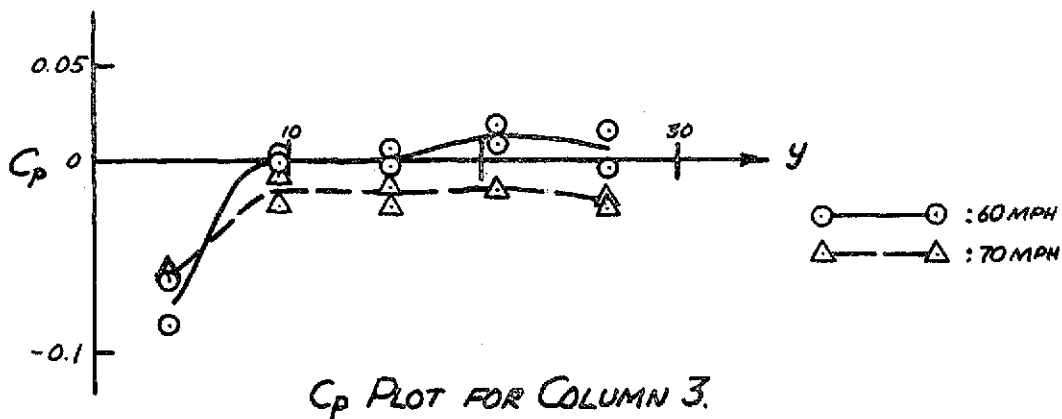
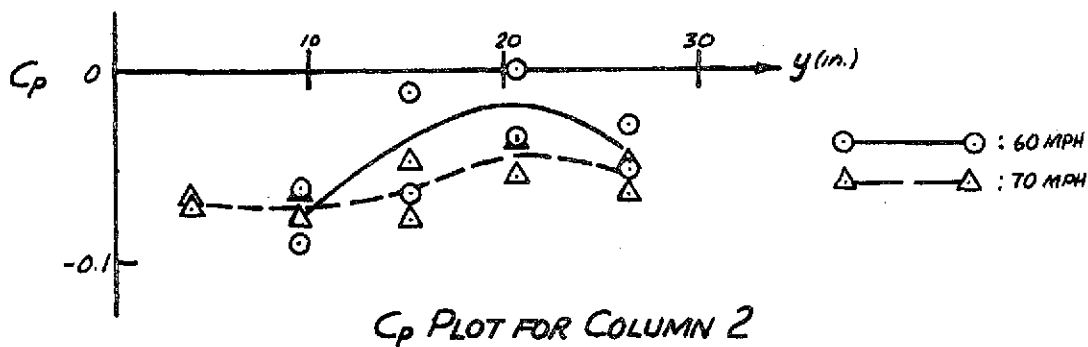
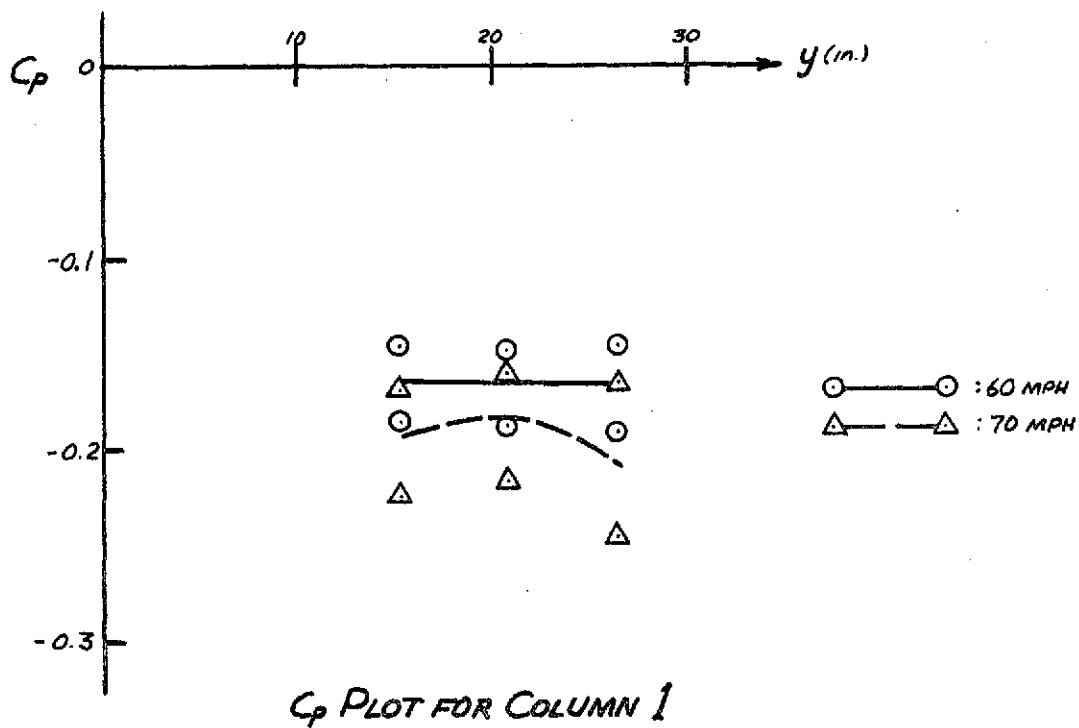
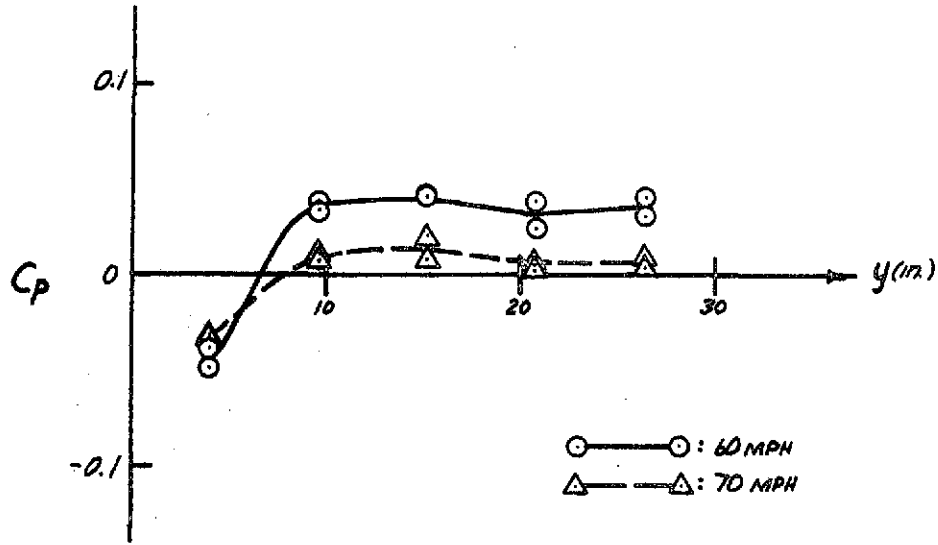
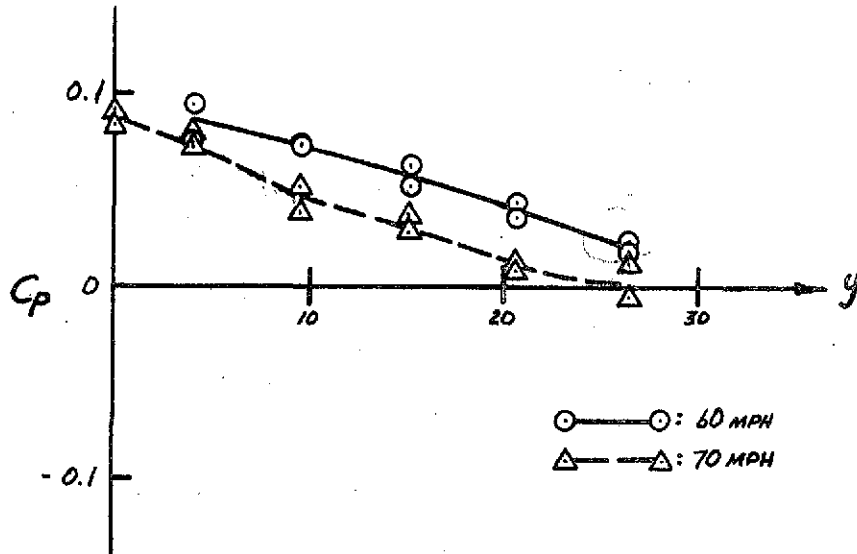


FIG. 9

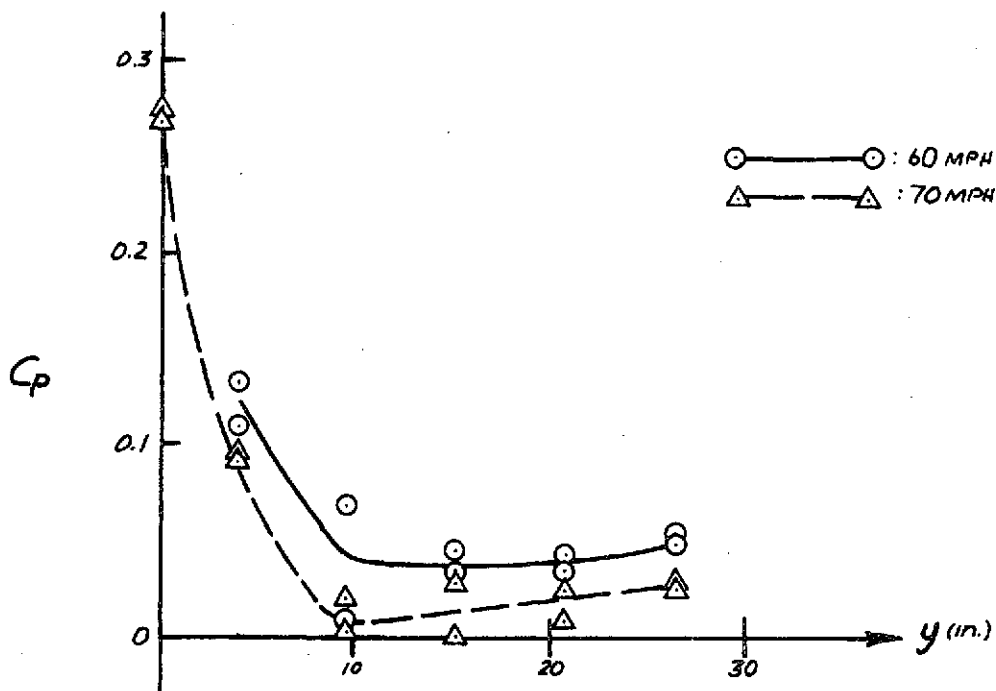


C_p PLOT FOR COLUMN 4

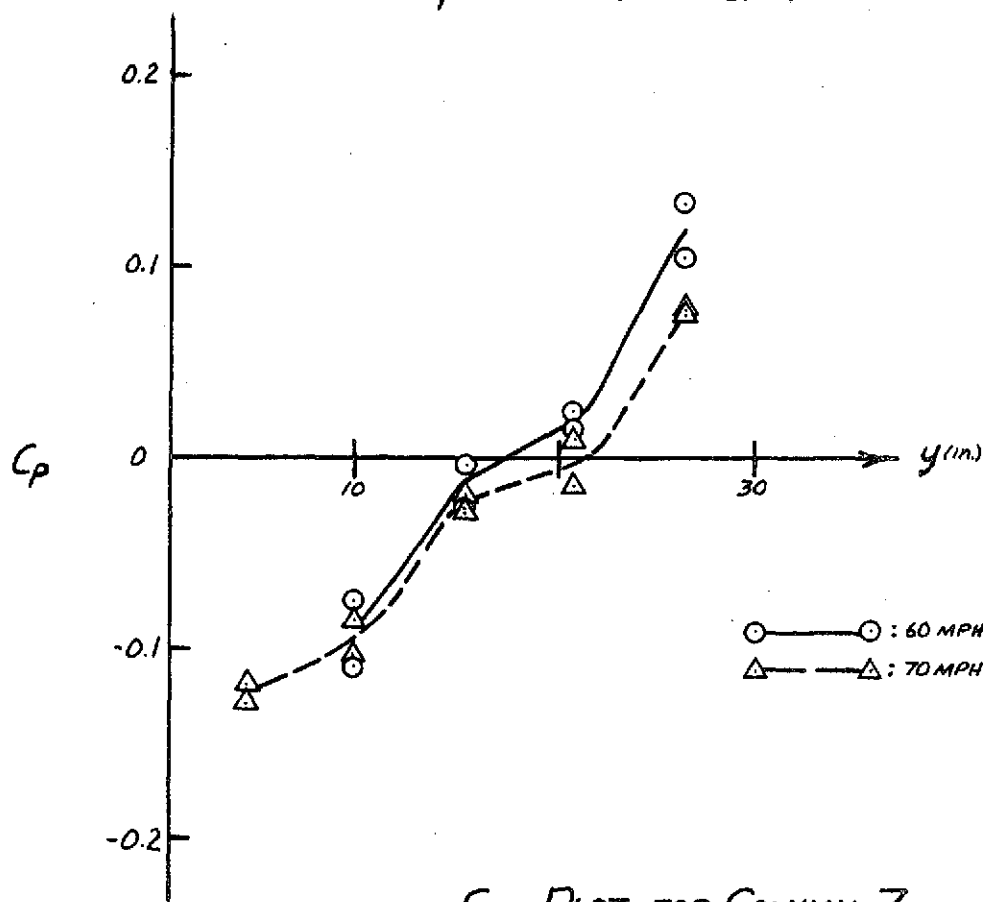


C_p PLOT FOR COLUMN 5

FIG. 10



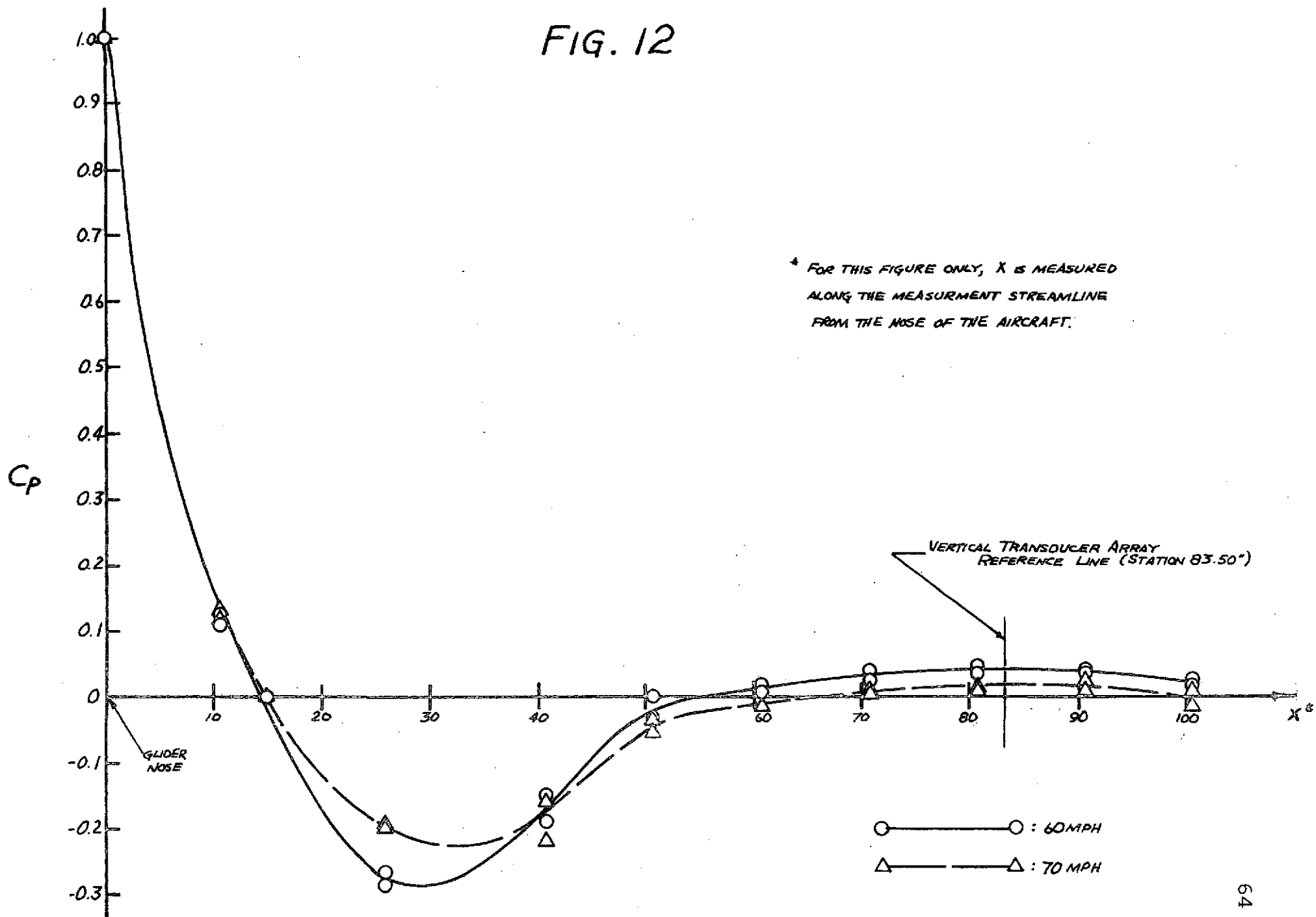
C_p PLOT FOR COLUMN 6



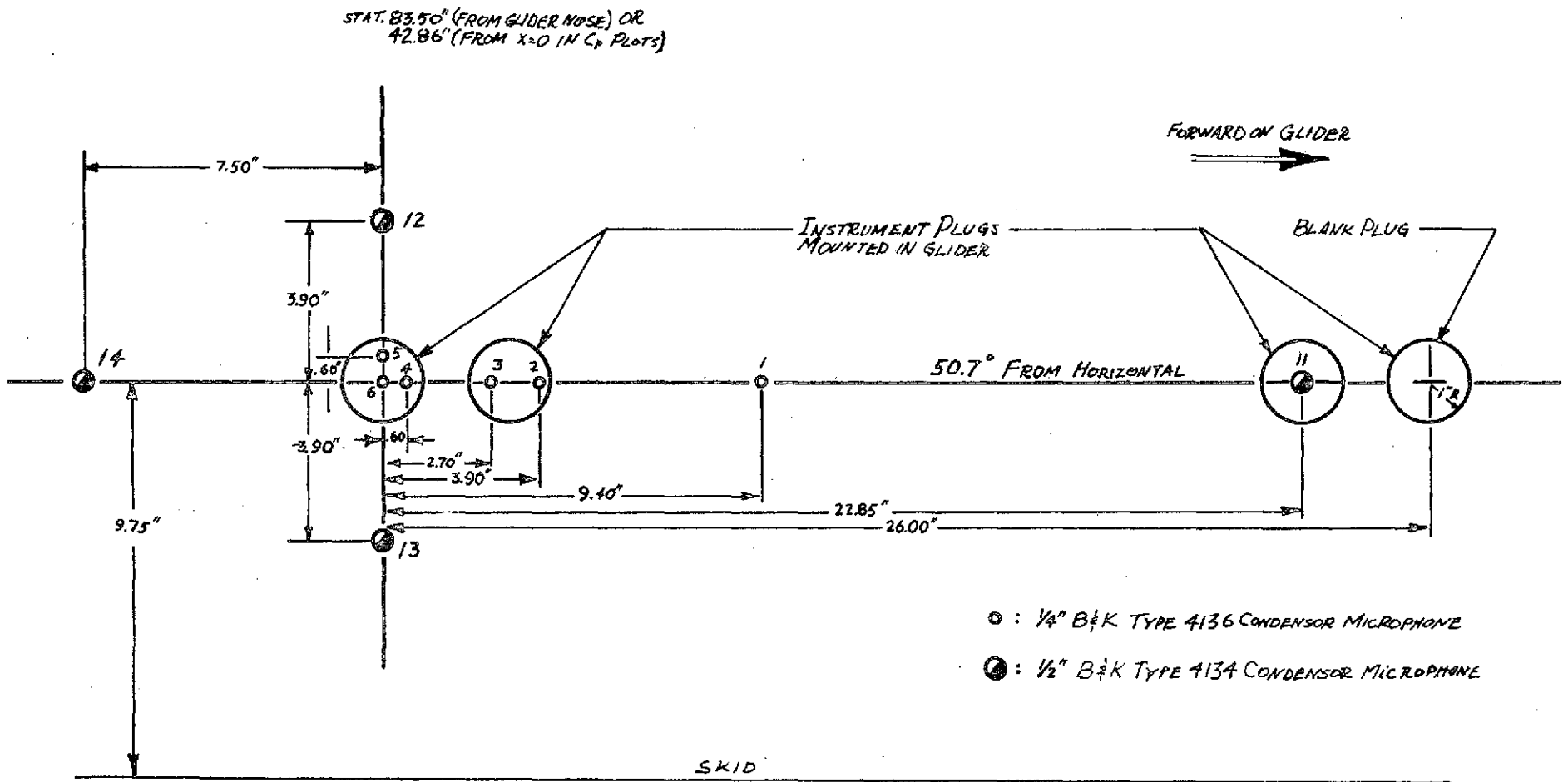
C_p PLOT FOR COLUMN 7

FIG. II

FIG. 12



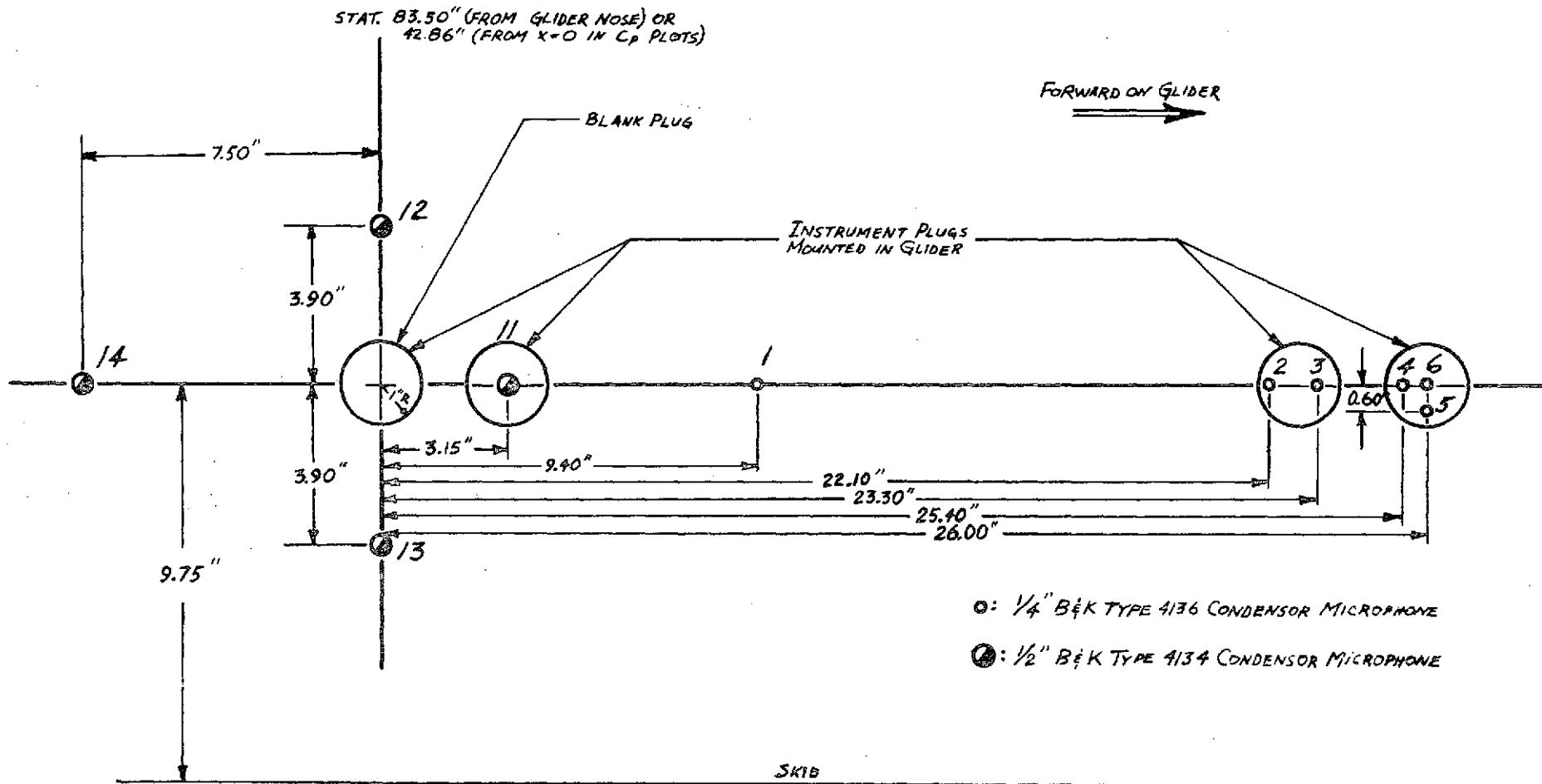
C_p PLOT FOR AIRCRAFT



PLANAR DEVELOPMENT OF TRANSDUCER ARRAY #1

FIG. 13

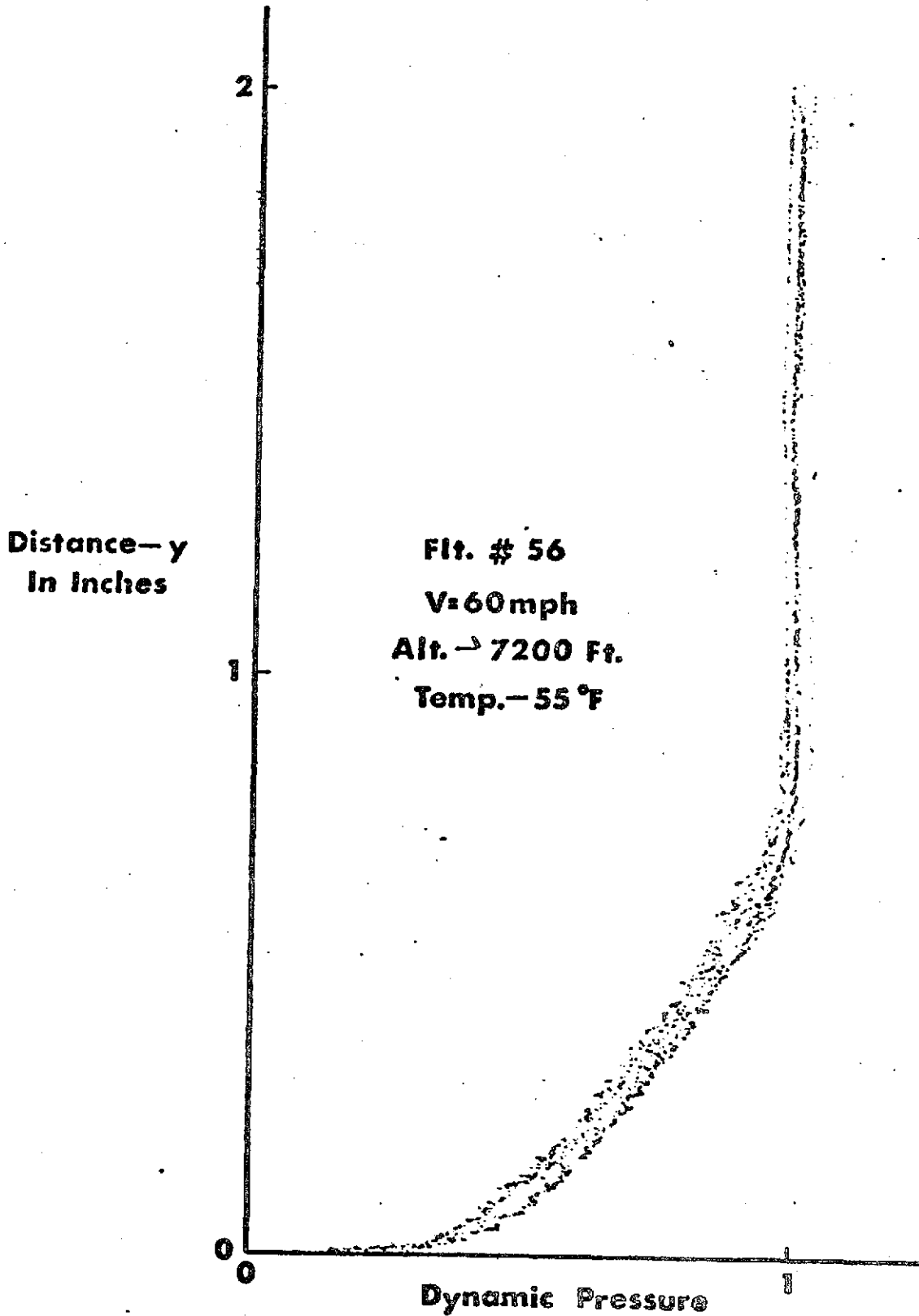
FIG. 14



PLANAR DEVELOPMENT OF TRANSDUCER ARRAY #2

BOUNDARY LAYER PITOT TRAVERSE

E



BOUNDARY LAYER PARAMETERS

55 M.P.H. INDICATED AIRSPEED

FLT. #	U_{∞} (ft/sec)	δ (in.)	π	$C_F (X10^3)$	δ^* (in.)	$H(\frac{\delta^*}{\theta})$	RMS DEV.	Re_{δ^*}
56	94.7	.750	.530	3.28	.115	1.391	.250	4210
57T	98.8	1.114	.715	2.86	.178	1.393	.228	6600
58	99.8	.731	.437	3.39	.107	1.380	.217	3960
59	100.5	.716	.510	3.32	.110	1.386	.141	4100
60	91.0	.743	.534	3.27	.114	1.395	.137	4200
62	93.2	.751	.515	3.29	.115	1.387	.167	4230
63T	90.1	1.097	.625	2.94	.168	1.379	.124	6500
74*	93.6	.658	.621	3.21	.107	1.407	.238	4160
75T*	84.9	1.050	.702	2.89	.167	1.394	.187	6340
76	93.4	.830	.757	2.92	.143	1.399	.223	5780
77T	91.6	1.235	.919	2.60	.208	1.417	.273	8350
80	91.4	.721	.701	3.04	.120	1.407	.178	4930
81	92.1	.712	.566	3.20	.111	1.391	.150	4550
86	90.4	.738	.590	3.19	.117	1.395	.106	4460
88**	92.1	.374	.190	4.22	.052	1.393	.247	1980
89T**	95.4	.748	.676	3.09	.121	1.414	.178	4660

T - Tripped boundary layer

* - forward plug in aft. mounting bracket

** - aft. plug of forward mounting bracket

Fig. 16

BOUNDARY LAYER PARAMETERS
60 M.P.H. INDICATED AIRSPEED

FLT #	U_{∞} (ft/sec)	δ (in.)	π	$C_f (X10^3)$	δ^* (in.)	$H(\frac{\delta^*}{\theta})$	RMS. DEV.	Re_{δ^*}
56	100.8	.781	.496	3.25	.117	1.377	.176	4610
57T	104.4	1.191	.728	2.78	.189	1.387	.286	7610
58	103.4	.766	.426	3.35	.111	1.370	.288	4330
59	106.3	.760	.460	3.29	.111	1.373	.133	4520
60	98.8	.790	.490	3.23	.118	1.371	.128	4810
62	99.6	.763	.468	3.28	.113	1.369	.181	4600
63T	95.7	1.104	.716	2.81	.175	1.387	.137	7300
74*	95.3	.699	.562	3.18	.109	1.384	.154	4740
75T*	92.3	1.083	.789	2.75	.176	1.400	.274	7380
76	101.6	.860	.727	2.88	.140	1.397	.129	6290
77T	98.8	1.316	1.033	2.44	.228	1.424	.241	10,060
80	97.1	.737	.710	2.98	.122	1.402	.168	5400
81	100.5	.754	.643	3.03	.122	1.384	.350	5550
86	95.5	.763	.589	3.14	.119	1.391	.097	4840
88**	96.9	.416	.192	4.05	.057	1.373	.218	2380
89T**	102.6	.819	.843	2.83	.140	1.425	.131	5830

T - Tripped boundary layer
 * - forward plug in aft. mounting bracket
 ** - aft. plug of forward mounting bracket

Fig. 17

BOUNDARY LAYER PARAMETERS
65 M.P.H. INDICATED AIRSPEED

FLT. #	U_{∞} (ft/sec)	δ (in.)	π	$C_f (X10^3)$	δ^* (in.)	$H(\frac{\delta^*}{\theta})$	RMS. DEV.	Re_{δ^*}
56	124.1	.852	.560	2.99	.128	1.362	.105	6520
57T	113.2	1.247	.858	2.60	.205	1.398	.123	9150
58	118.8	.818	.581	3.04	.125	1.376	.161	5830
59	126.8	.791	.542	3.06	.119	1.366	.129	5910
60	108.6	.815	.528	3.12	.123	1.367	.121	5520
62	102.5	.811	.478	3.15	.118	1.360	.092	5560
63T	105.0	1.153	.762	2.70	.184	1.384	.082	8550
74*	105.9	.729	.601	3.05	.113	1.383	.187	5550
75T*	100.7	1.193	.881	2.58	.196	1.403	.938	9110
76	109.0	.940	.743	2.78	.150	1.389	.165	7450
77T	107.3	1.372	1.089	2.34	.238	1.426	.199	11,674
80	106.8	.787	.701	2.90	.126	1.391	.221	6290
81	109.2	.820	.678	2.90	.130	1.385	.284	6550
86	104.9	.852	.601	3.00	.135	1.367	.217	6180
88**	105.0	.439	.249	3.85	.061	1.368	.260	2800
89T**	110.7	.819	.931	2.71	.144	1.430	.093	6550

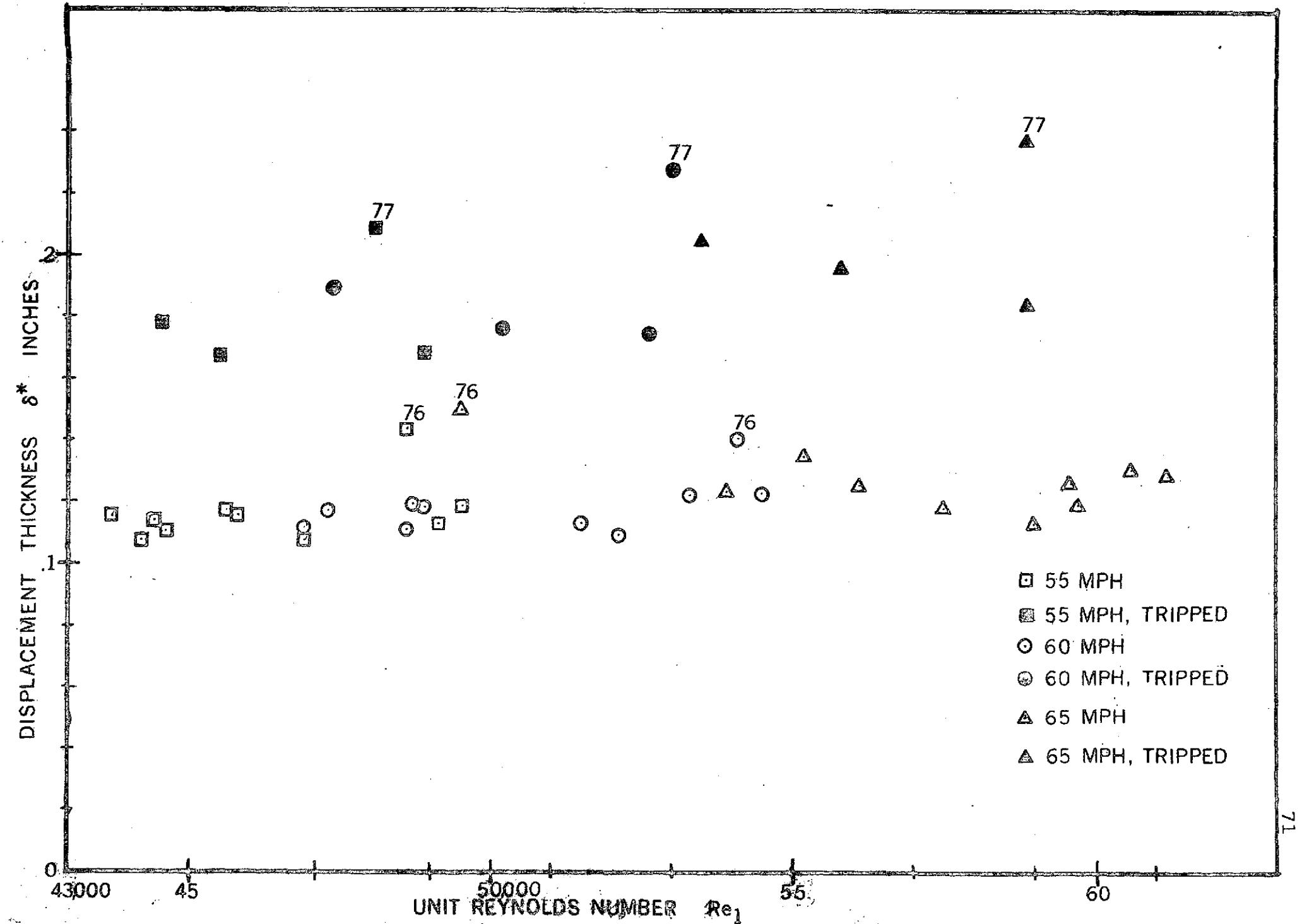
T - Tripped boundary layer

* - forward plug in aft. mounting bracket

** - aft. plug of forward mounting bracket

Fig. 18

FIG. 19



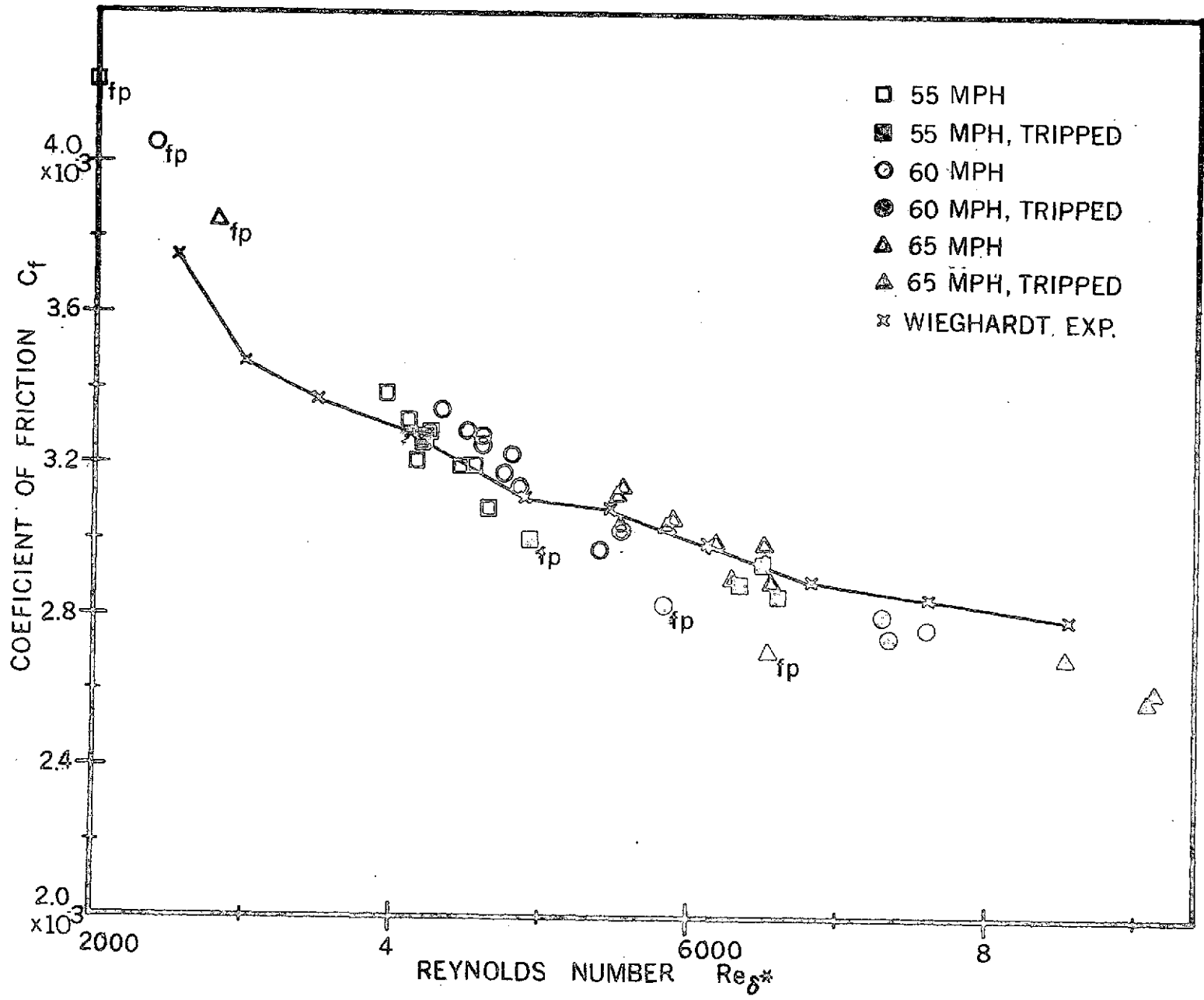


FIG. 20

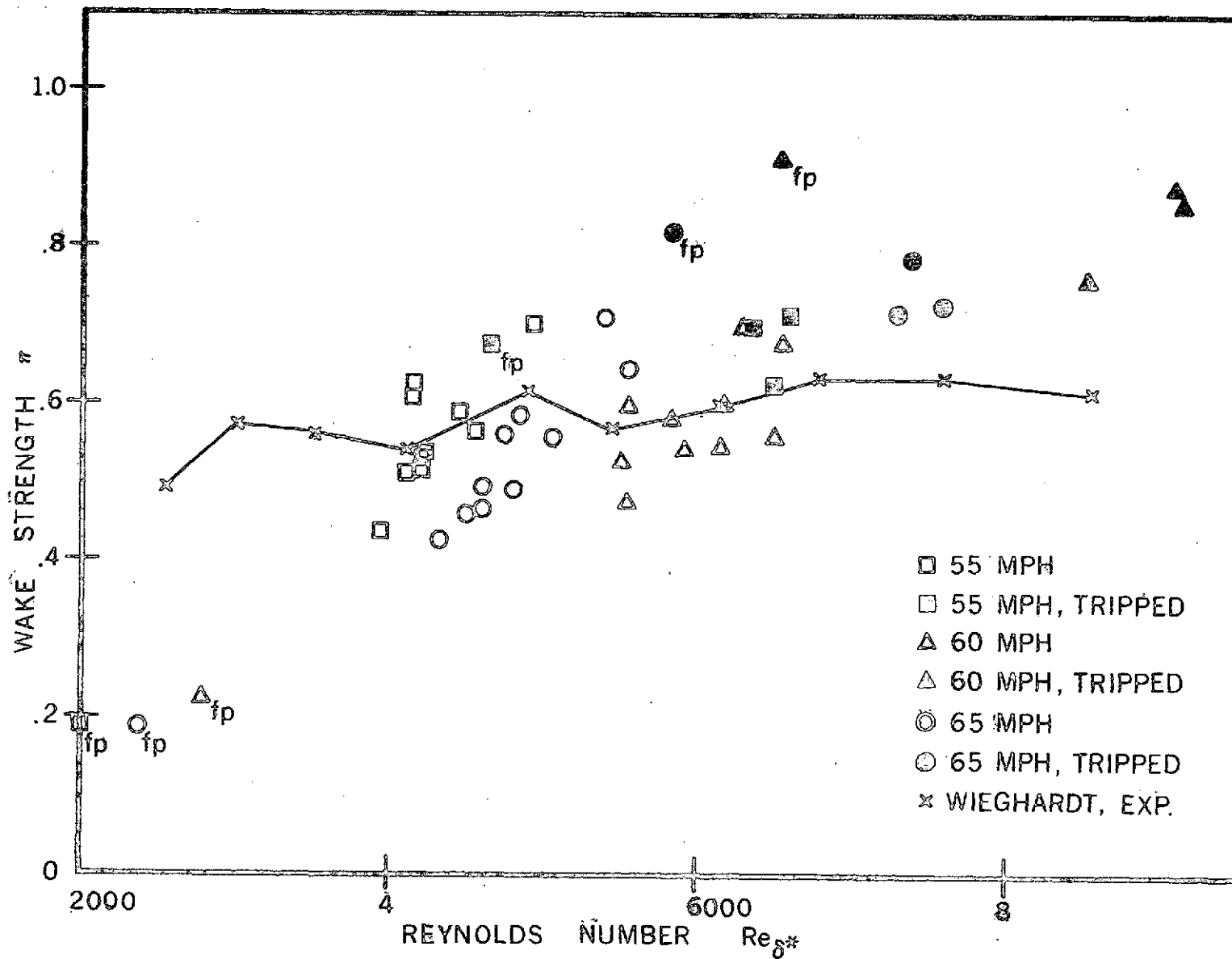


FIG. 21

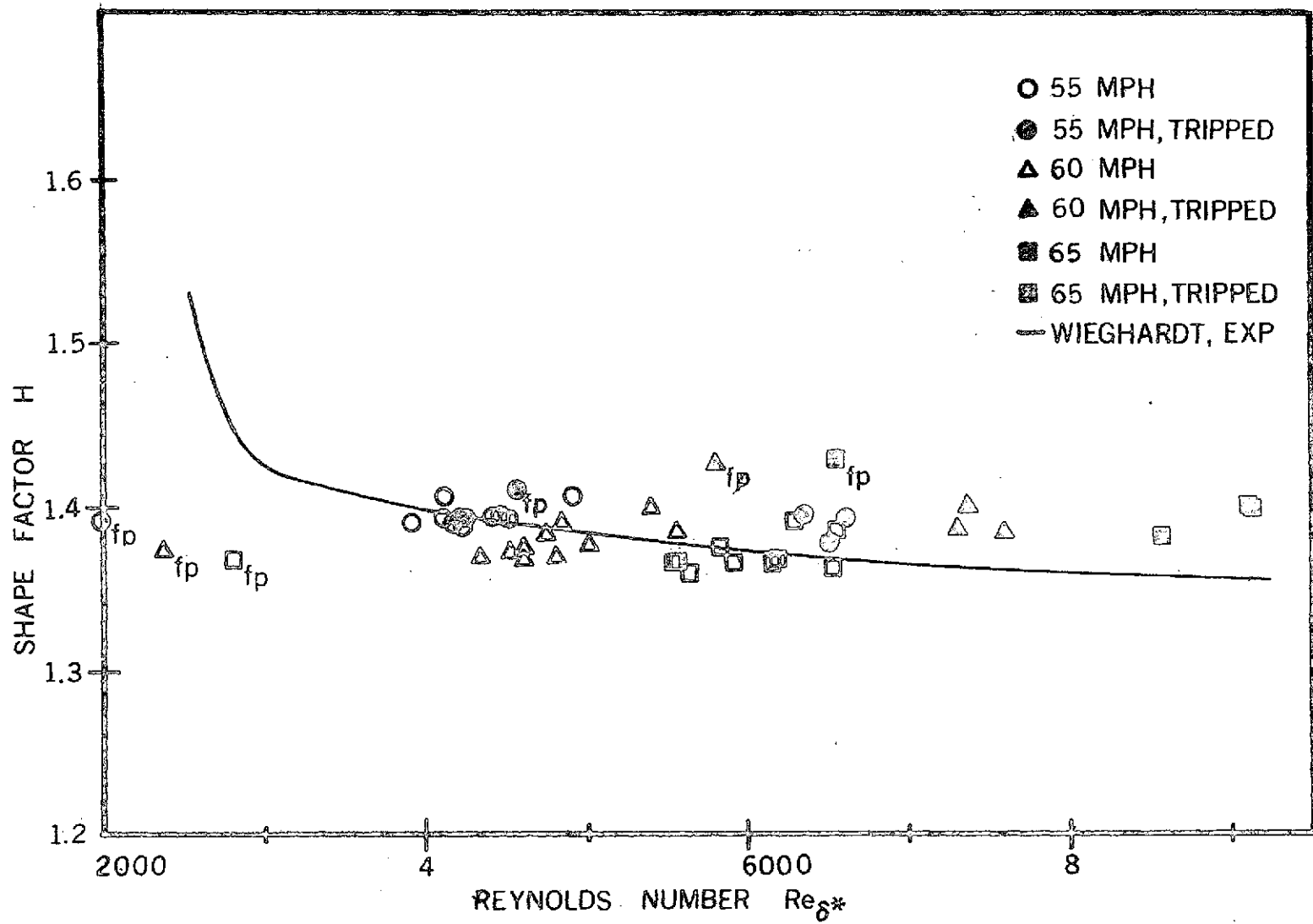


FIG. 22

Microphone RMS Histories
(all table values in volts)

FIGURE 23

EVENT	100db TEST	UNTRIPPED FLIGHTS			TRIPPED FLIGHTS		
		55 mph	60 mph	65 mph	55 mph	60 mph	65 mph

1/2" Microphone #1, SN 284175

TEST	.393						
FLT 90		.21	.25	.29			
FLT 91					.27	.31	.36
FLT 92					.27	.31	.36
TEST	.381						
FLT 93					.27	.31	.36
FLT 94		.21	.24	.29			
TEST	.388						
FLT 95					.28	.31	.36
FLT 96					.27	.30	<u>.33</u>

1/2" Microphone #2, SN 296467

TEST	.381						
FLT 90		.22	.27	.33			
FLT 91					.27	.31	.36
FLT 92					.26	.31	.35
TEST	.377						
FLT 93					.27	.32	.36
FLT 94		.22	.26	.32			
TEST	.380						
FLT 95					<u>.30</u>	.31	.36
FLT 96					.27	.29	<u>.33</u>

1/2" Microphone #3, SN 284167

TEST	<u>.289</u>						
FLT 90		<u>.16</u>	<u>.20</u>	<u>.24</u>			
FLT 91					<u>.03</u>	<u>.04</u>	<u>.04</u>
FLT 92					--	--	--
TEST	.373						
FLT 93					.27	<u>.31</u>	<u>.35</u>
FLT 94		.24	.27	.30			
TEST	.373						
FLT 95					.27	.29	.35
FLT 96					.26	.28	<u>.32</u>

EVENT	100db TEST	UNTRIPPED FLIGHTS			TRIPPED FLIGHTS		
		55 mph	60 mph	65 mph	55 mph	60 mph	65 mph

1/2" Microphone #4, SN 296614

TEST	.391						
FLT 90		.23	.28	.32			
FLT 91					.28	.32	.35
FLT 92					.26	.32	.36
TEST	.382						
FLT 93					.28	.32	.37
FLT 94					.24	.27	.32
TEST	.388						
FLT 95					.28	.32	.36
FLT 96					.27	<u>.29</u>	.34

1/4" Microphone #1, SN 248842

TEST	.465						
FLT 90		.41	.44	.53			
FLT 91					.43	.48	.55
FLT 92					.43	.50	.58
TEST	.464						
FLT 93					.43	.50	.58
FLT 94		.41	.46	.51			
TEST	.457						
FLT 95					.42	.47	.53
FLT 96					.43	.47	.53
TEST	<u>1.129</u>						

1/4" Microphone #2, SN 318661

TEST	.745						
FLT 90		.62	.70	.80			
FLT 91					.66	.78	.86
FLT 92					.65	<u>.73</u>	<u>.83</u>
TEST	.781						
FLT 93					.68	.78	<u>.89</u>
FLT 94		.63	.72	.83			
TEST	.693						
FLT 95					<u>.56</u>	<u>.65</u>	<u>.72</u>
FLT 96					<u>.59</u>	<u>.62</u>	<u>.75</u>
TEST							

FIGURE 25

EVENT	100db TEST	UNTRIPPED FLIGHTS			TRIPPED FLIGHTS		
		55 mph	60 mph	65 mph	55 mph	60 mph	65 mph
1/4" Microphone #3, SN 304671							
TEST	.456						
FLT 90		.38	.42	.50			
FLT 91					.41	.45	.53
FLT 92					.39	.45	.53
TEST	.434						
FLT 93					.39	.45	<u>.49</u>
FLT 94		.36	.40	.48			
TEST	.465						
FLT 95					.40	.45	.52
FLT 96					.39	.42	.51
TEST	1.317						
1/4" Microphone #4, SN 248826							
TEST	.378						
FLT 90		.31	.35	.41			
FLT 91					.34	.40	<u>.42</u>
FLT 92					.33	.38	<u>.44</u>
TEST	.388						
FLT 93					.35	.41	.47
FLT 94		.34	.37	<u>.45</u>			
TEST	.388						
FLT 95					<u>.38</u>	<u>.45</u>	<u>.50</u>
FLT 96	Microphone not flush				<u>.31</u>	<u>.33</u>	<u>.38</u>
1/4" Microphone #5, SN 153022							
TEST	.378						
FLT 90		.31	.36	.42			
FLT 91					.34	.39	<u>.41</u>
FLT 92					.34	.38	<u>.44</u>
TEST	.412						
FLT 93					.37	.42	.47
FLT 94		.33	.38	.44			
TEST	.413						
FLT 95					.38	.42	<u>.48</u>
FLT 96					.37	.39	<u>.46</u>
1/4" Microphone #6, SN 276979							
TEST	.482						
FLT 90		.38	.44	.51			
FLT 91					.43	.46	.52
FLT 92					.42	.48	.54
TEST	.497						
FLT 93					.45	<u>.52</u>	<u>.62</u>
FLT 94		.41	.46	<u>.55</u>			
TEST	<u>.572</u>						
FLT 95					<u>.52</u>	<u>.60</u>	<u>.68</u>
FLT 96	Microphone protruding				<u>.68</u>	<u>.76</u>	<u>.87</u>

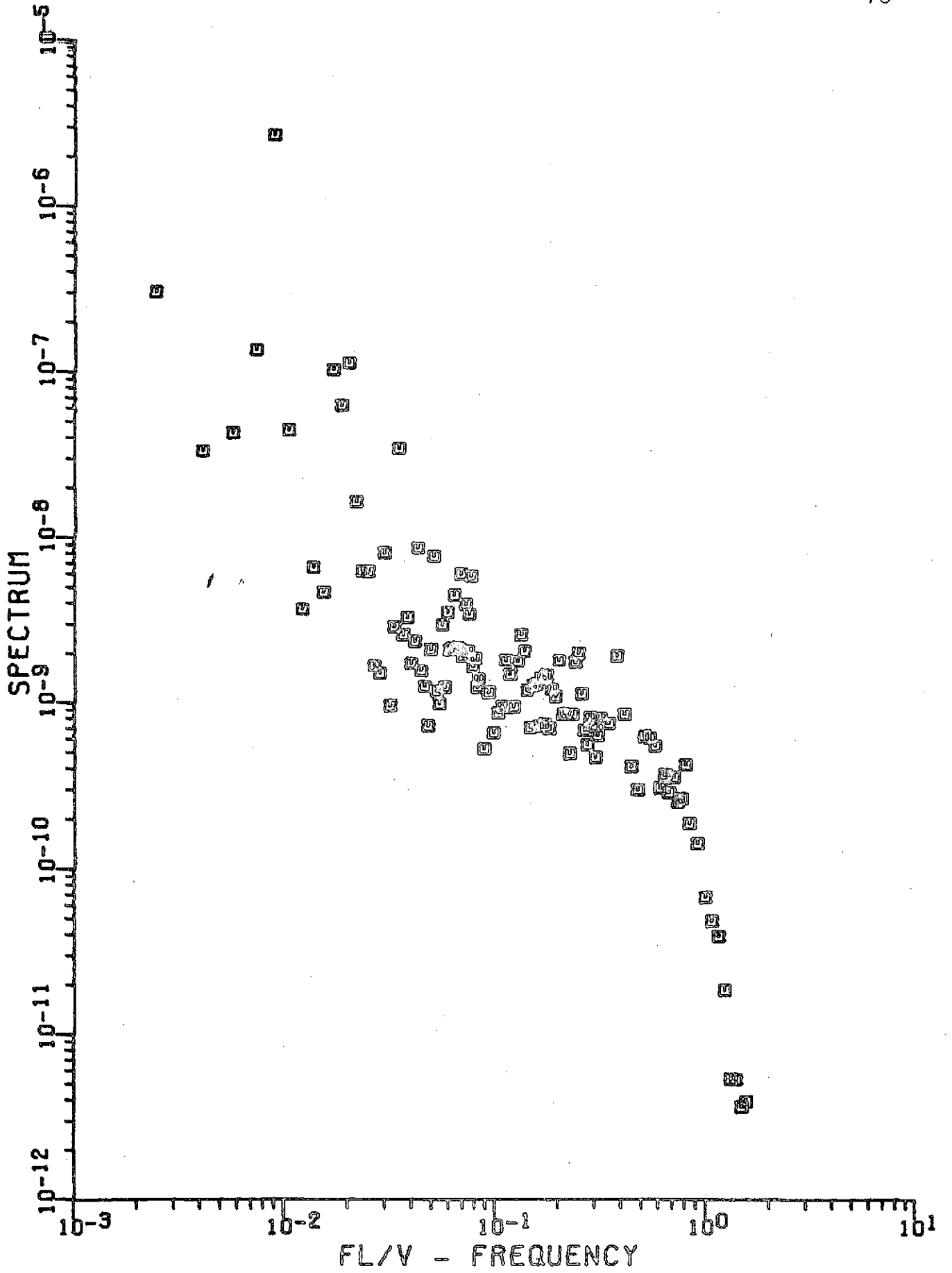
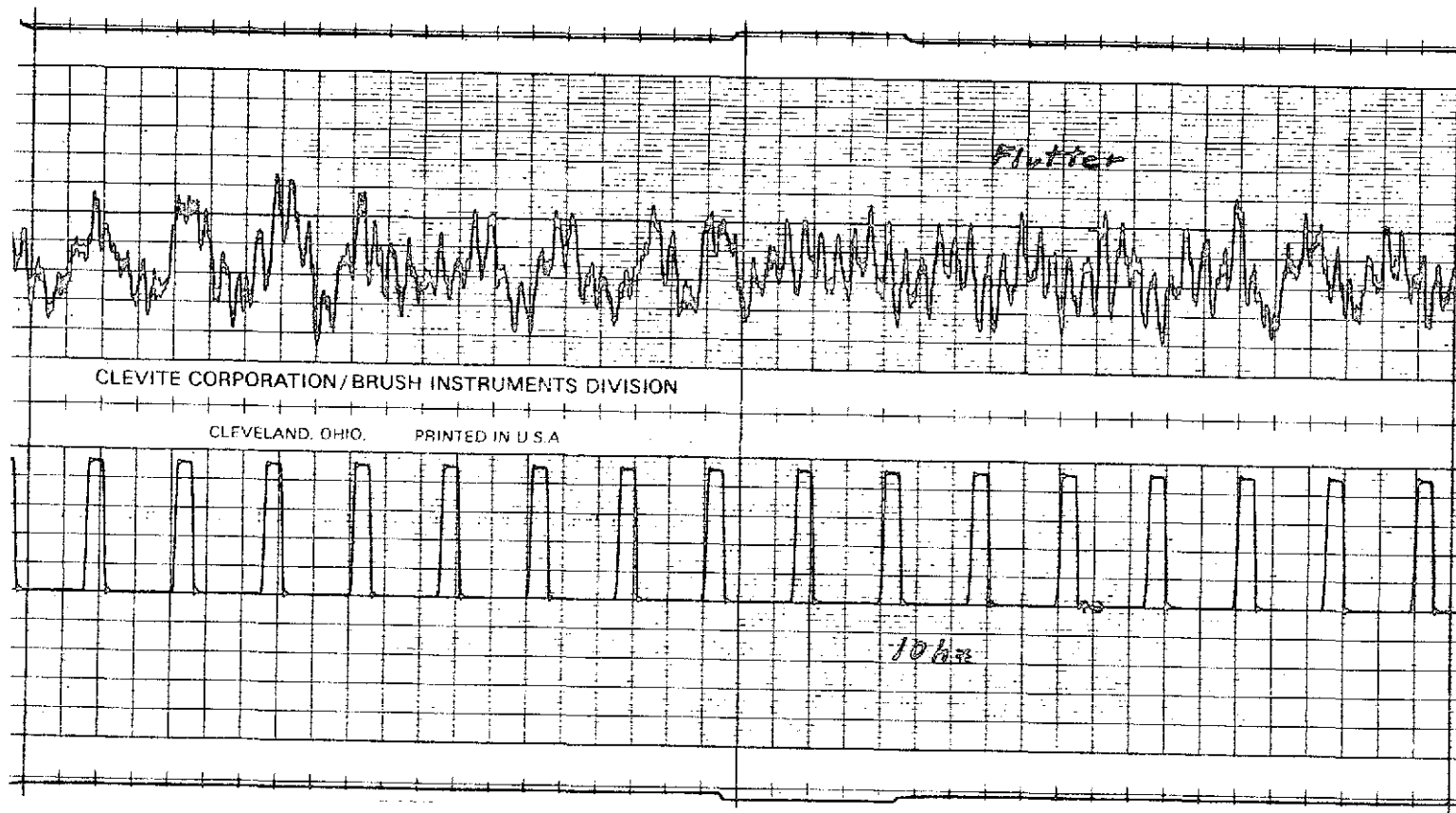


FIG. 26

FIG. 27

Tape Recorder Flutter Test Record



Scale 2mv/div , Chart Speed 125 mm/sec , Recorder Speed 30 ips
RMS .015 v Record & Play ← Power Switch

FIGURE 28a

$$\text{RMS of Pressure Fluctuations } C_{P_X} = P^2 / q$$

FLIGHT (MIC SIZE)	INDICATED AIRSPEED	FILE NUMBER	C_{P_T} TEST	C_{P_I} PSD INTEGRAL	C_{P_L} LOOP	$\frac{C_{P_L}}{C_f}$	$\frac{d}{\delta^*}$	q PSF
56 (1/2")	55	3924	3.42×10^{-3}	3.76×10^{-3}	4.04×10^{-3}	1.235	3.18	7.69
	60	3925	3.44×10^{-3}	3.69×10^{-3}	3.98×10^{-3}	1.225	3.15	8.89
	65	3926	3.07×10^{-3}	3.50×10^{-3}	3.70×10^{-3}	1.236	2.87	11.18
57 (1/2") Tripped	55	3927	4.06×10^{-3}	4.62×10^{-3}	4.82×10^{-3}	1.69	2.06	8.2
	60	3928	3.89×10^{-3}	4.35×10^{-3}	4.61×10^{-3}	1.658	1.95	9.4
	65	3929	3.71×10^{-3}	3.98×10^{-3}	4.33×10^{-3}	1.665	1.79	11.4
58 (1/4") Sensitivity Unknown	55	3930	6.22×10^{-3}	6.60×10^{-3}	6.88×10^{-3}	2.024	1.56	8.2
	60	3931	6.48×10^{-3}	6.74×10^{-3}	7.52×10^{-3}	2.244	1.51	9.0
	65	3932	5.47×10^{-3}	5.55×10^{-3}	5.18×10^{-3}	2.03	1.35	12.4
59 (1")	55	3933	2.33×10^{-3}	2.39×10^{-3}	2.74×10^{-3}	.826	6.69	8.3
	60	3934	2.21×10^{-3}	2.28×10^{-3}	2.64×10^{-3}	.801	6.63	9.6
	65	3935	2.21×10^{-3}	2.30×10^{-3}	2.64×10^{-3}	.863	6.23	11.2
62 (1/2")	60	4520	3.35×10^{-3}	3.45×10^{-3}	3.71×10^{-3}	1.039	3.26	8.95
63 (1/2") Tripped	60	4518	3.89×10^{-3}	3.80×10^{-3}	3.95×10^{-3}	1.406	2.10	9.1

FIGURE 28b

FLIGHT (MIC SIZE)	INDICATED AIRSPEED	FILE NUMBER	C_{P_T} TEST	C_{P_I} PSD INTEGRAL	C_{P_L} LOOP	$\frac{C_{P_L}}{C_f}$	$\frac{d}{S^*}$	q PSF
80 (1")	60	4519	2.15×10^{-3}	2.16×10^{-3}	2.23×10^{-3}	.734	6.07	9.5
81 (1/4")	55	4523	4.73×10^{-3}	4.75×10^{-3}	5.00×10^{-3}	1.567	1.58	8.32
	60	4524	4.23×10^{-3}	4.60×10^{-3}	4.61×10^{-3}	1.521	1.38	10.10
	65	4525	3.90×10^{-3}	4.26×10^{-3}	4.21×10^{-3}	1.450	1.29	12.22
92 (1/4") #1 (1/4") #2 (1/4") #3 (1/4") #4 (1/4") #5 (1/4") #6	50	4529	4.83×10^{-3}	4.68×10^{-3}	4.52×10^{-3}	1.59	1.04	9.45
		4531	4.42×10^{-3}	4.73×10^{-3}	4.69×10^{-3}	1.67	.97	9.45
		4528	4.45×10^{-3}	4.59×10^{-3}	4.19×10^{-3}	1.50	.95	9.45
		4527	4.41×10^{-3}	4.57×10^{-3}	4.50×10^{-3}	1.61	.92	9.45
		4535	4.12×10^{-3}	4.24×10^{-3}	4.11×10^{-3}	1.48	.92	9.45
		4527	4.39×10^{-3}	4.35×10^{-3}	4.57×10^{-3}	1.64	.92	9.45
(1/2") #1 (1/2") #2 (1/2") #4		4529	3.58×10^{-3}	3.57×10^{-3}	3.67×10^{-3}	1.24	2.79	9.45
		4534	3.66×10^{-3}	3.66×10^{-3}	3.67×10^{-3}	1.32	2.02	9.45
		4527	3.69×10^{-3}	3.47×10^{-3}	3.55×10^{-3}	1.31	1.86	9.45
93 (1/4") #1 (1/4") #2 (1/4") #3 (1/4") #4 (1/4") #5 (1/4") #6	60	4538	5.06×10^{-3}	5.20×10^{-3}	4.22×10^{-3}	1.49	1.04	9.05
		4537	4.94×10^{-3}	5.44×10^{-3}	5.16×10^{-3}	1.84	.97	9.05
		4537	5.65×10^{-3}	4.69×10^{-3}	4.69×10^{-3}	1.68	.95	9.05
		4536	4.98×10^{-3}	4.71×10^{-3}	4.87×10^{-3}	1.75	.92	9.05
		4544	4.77×10^{-3}	4.96×10^{-3}	4.77×10^{-3}	1.71	.92	9.05
		4536	4.97×10^{-3}	5.42×10^{-3}	5.69×10^{-3}	1.83	.92	9.05

FIGURE 28c

FLIGHT (MIC SIZE)	INDICATED AIRSPEED	FILE NUMBER	C_{PT} TEST	C_{PI} PSD INTEGRAL	C_{PL} LOOP	$\frac{C_{PL}}{C_f}$	$\frac{d}{S^*}$	ϵ PSF
(1/2") #1		4540	3.75×10^{-3}	3.93×10^{-3}	3.87×10^{-3}	1.30	2.79	
(1/2") #2		4543	3.95×10^{-3}	4.06×10^{-3}	3.87×10^{-3}	1.39	2.02	
(1/2") #3		4543	3.89×10^{-3}	3.90×10^{-3}	3.85×10^{-3}	1.38	2.02	
(1/2") #4		4538	3.87×10^{-3}	3.65×10^{-3}	3.70×10^{-3}	1.36	1.86	
<hr/>								
95	60							
(1/4") #1		4545	5.01×10^{-3}	4.54×10^{-3}	4.84×10^{-3}		1.04	8.58
(1/4") #2		4546	4.34×10^{-3}	4.34×10^{-3}	4.37×10^{-3}		.97	8.58
(1/4") #3		4546	4.90×10^{-3}	4.56×10^{-3}	4.88×10^{-3}		.95	8.58
(1/4") #4		4547	5.76×10^{-3}	5.69×10^{-3}	5.64×10^{-3}		.92	8.58
(1/4") #5		4553	5.02×10^{-3}	4.67×10^{-3}	4.79×10^{-3}		.92	8.58
(1/4") #6		4547	5.16×10^{-3}	5.53×10^{-3}	5.29×10^{-3}		.92	8.58
(1/2") #1		4545	3.95×10^{-3}	3.98×10^{-3}	3.91×10^{-3}		2.79	8.58
(1/2") #2		4552	4.93×10^{-3}	3.97×10^{-3}	3.91×10^{-3}		2.02	8.58
(1/2") #3		4553	3.83×10^{-3}	3.99×10^{-3}	3.88×10^{-3}		2.02	8.58
(1/2") #4		4545	4.07×10^{-3}	3.56×10^{-3}	3.73×10^{-3}		1.86	8.58
<hr/>								
	60							
(1/4") #1		4560		4.74×10^{-3}	4.95×10^{-3}		1.04	8.38
(1/4") #2		4555		4.52×10^{-3}	4.56×10^{-3}		.97	8.38
(1/4") #3		4555		4.84×10^{-3}	4.77×10^{-3}		.95	8.38
(1/4") #4		4560		4.34×10^{-3}	4.29×10^{-3}		.92	8.38
(1/4") #5		4562		5.21×10^{-3}	4.99×10^{-3}		.92	8.38
(1/4") #6		4556		7.64×10^{-3}	7.07×10^{-3}		.92	8.38
(1/2") #1		4554		3.93×10^{-3}	4.00×10^{-3}		2.79	
(1/2") #2		4561		4.02×10^{-3}	4.04×10^{-3}		2.02	
(1/2") #3		4561		3.78×10^{-3}	3.88×10^{-3}		2.02	
(1/2") #4		4554		3.58×10^{-3}	3.83×10^{-3}		1.86	

FIG. 29

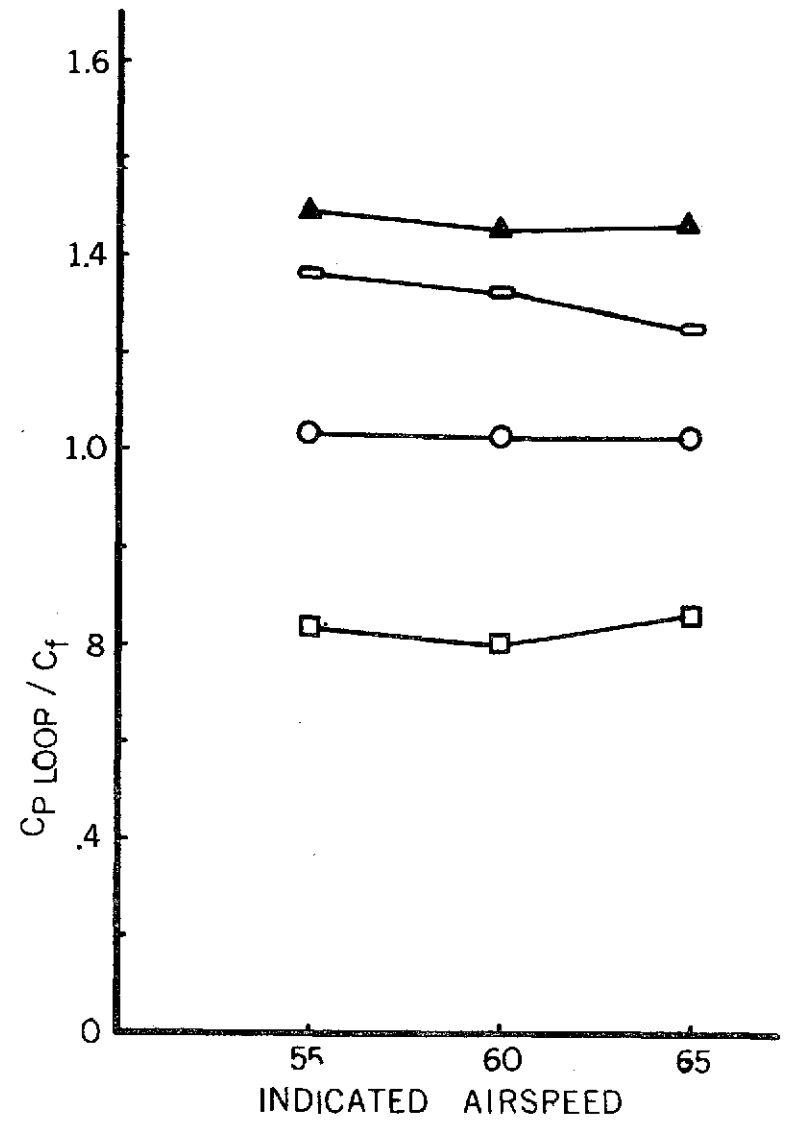
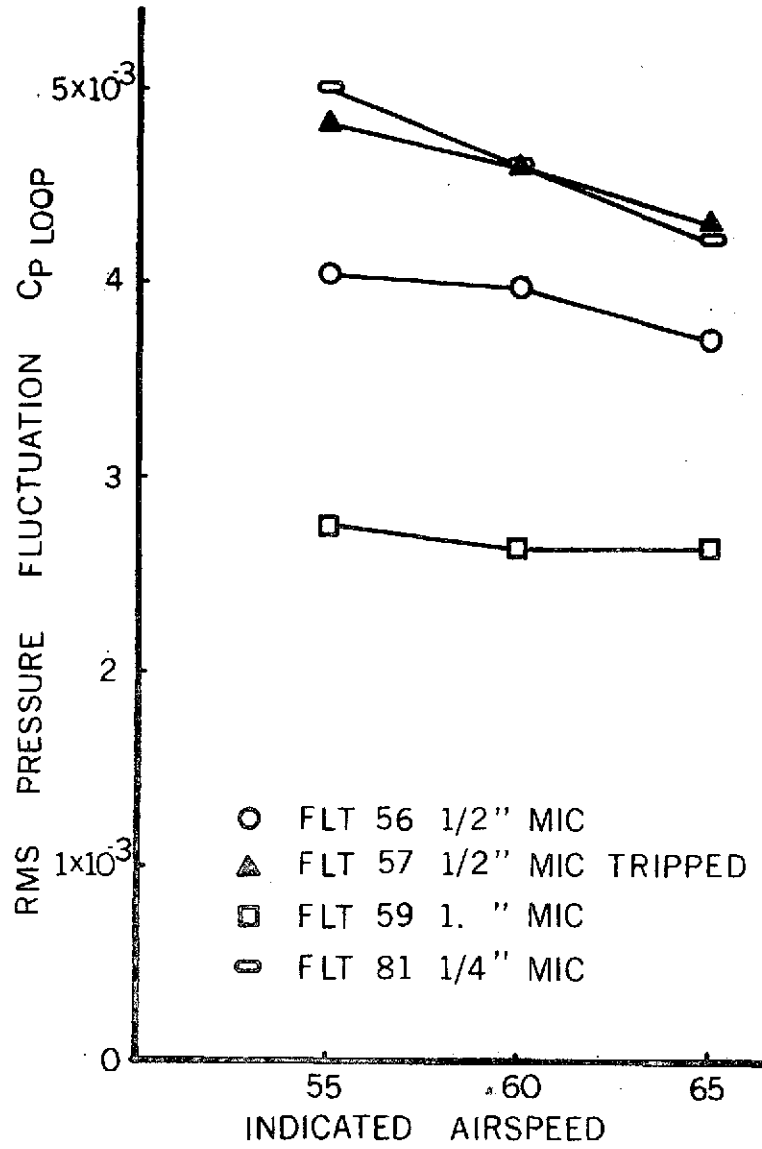
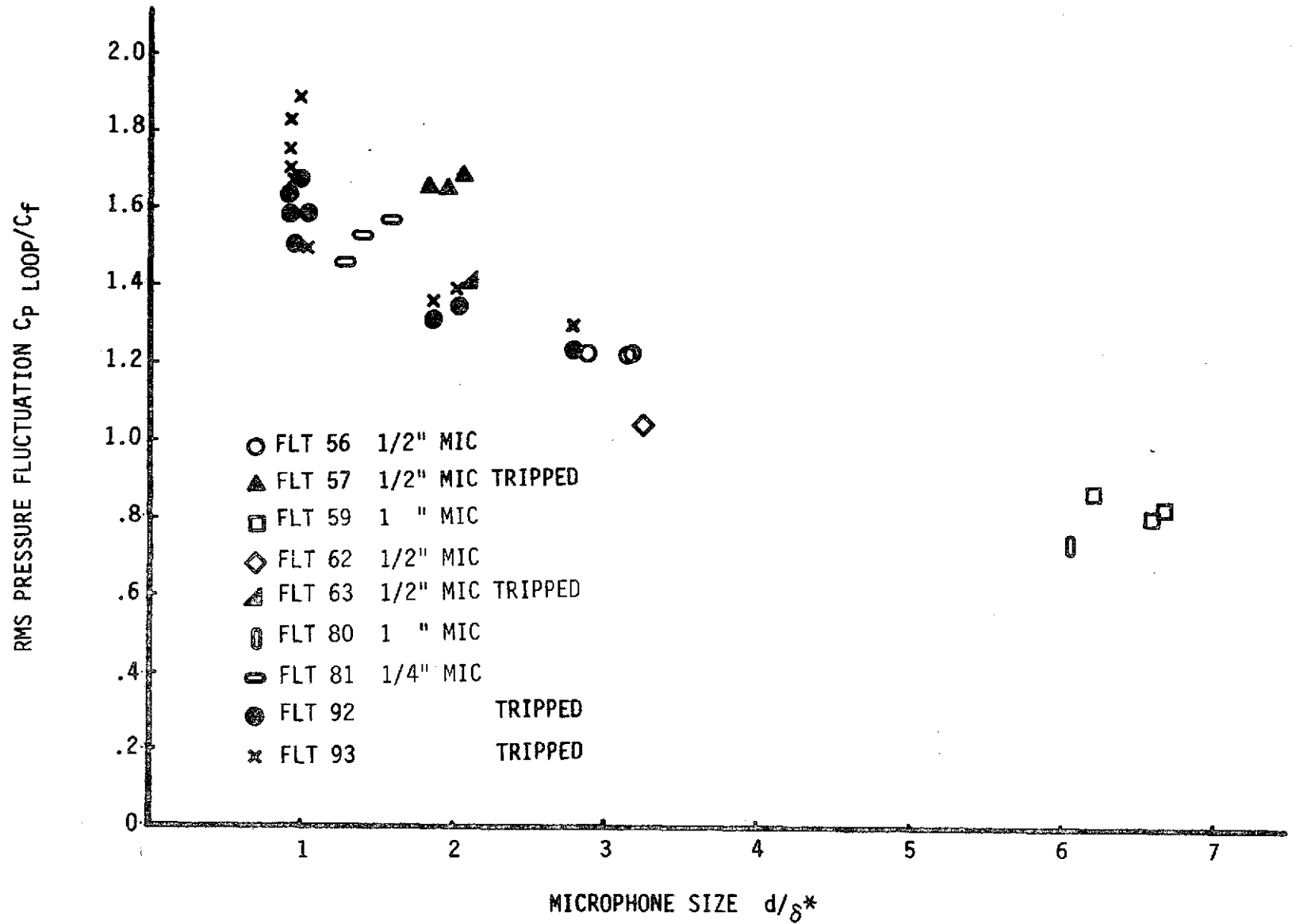


FIGURE 31



Power Spectra Correction Factors

86

Coordinate	$\frac{GV}{Q^2 \delta^*}$	$\frac{F\delta^*}{V}$	$\frac{GV}{\tau^2 \delta}$	$\frac{F\delta}{V}$
Correction Multiplier	C_1	C_2	C_3	C_4
File #				
3924	8.72	.115	1.25 x 10 ⁵	.750
3925	12.46	.118	1.78 x 10 ⁵	.788
3926	7.42	.126	1.25 x 10 ⁵	.839
3927	5.16	.172	1.01 x 10 ⁵	1.076
3928	5.22	.185	1.08 x 10 ⁵	1.166
3929	4.52	.199	1.10 x 10 ⁵	1.211
3930	7.83	.103	1.00 x 10 ⁵	.704
3931	9.47	.111	1.23 x 10 ⁵	.766
3932	6.59	.115	1.09 x 10 ⁵	.753
3933	8.14	.105	1.13 x 10 ⁵	.684
3934	8.56	.108	1.15 x 10 ⁵	.677
3935	8.06	.116	1.29 x 10 ⁵	.771
4520	1.764	.567	.243 x 10 ⁵	3.829
4521	2.292	.436	.461 x 10 ⁵	2.75
4522	1.646	.608	.307 x 10 ⁵	3.67
4523	1.784	.560	.271 x 10 ⁵	3.59
4524	1.640	.610	.289 x 10 ⁵	3.77
4525	1.544	.648	.289 x 10 ⁵	4.12
4527 (MIC 6)	2.198	.455	.450 x 10 ⁵	2.88
4527-4563:				
Track 11	3.03	.330		
Track 1	2.469	.405		
Track 2	2.230	.435		
Track 3	2.260	.442		
Track 4, 5, 6, 10, 11, 12, 13	2.198	.455		
Track 14	2.02	.495		

Remarks: Files 3924 through 3935 corrected for errors in Q, V, and L. Files 4520 through 4527 corrected for errors in L and tape playback speed.

Airspeed Effects On PSD, 1/4" Mic

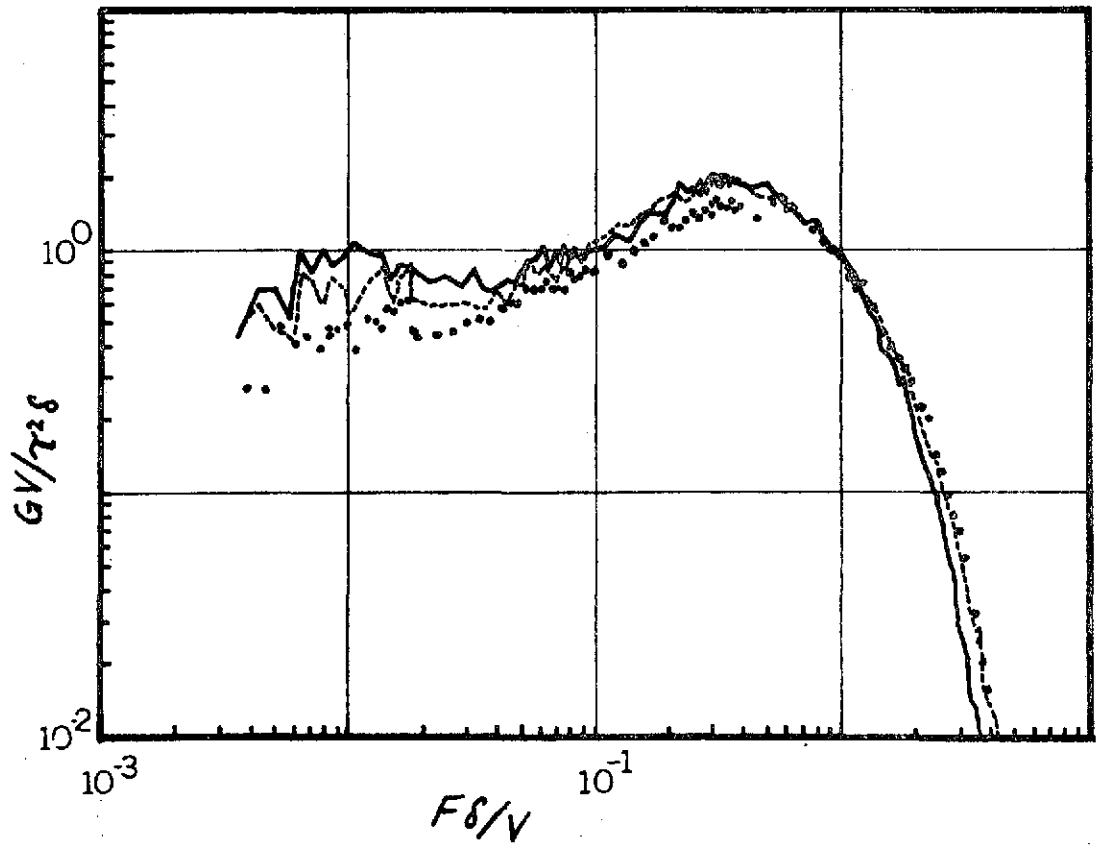
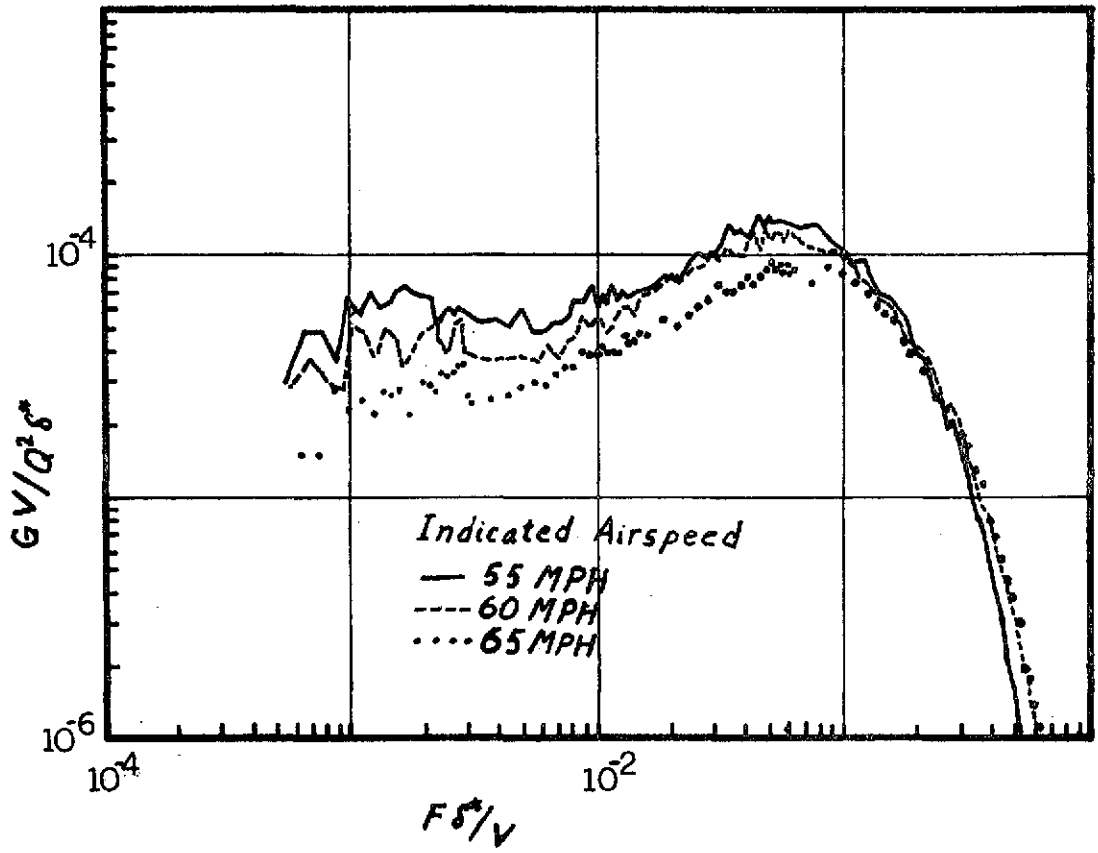


FIG. 33

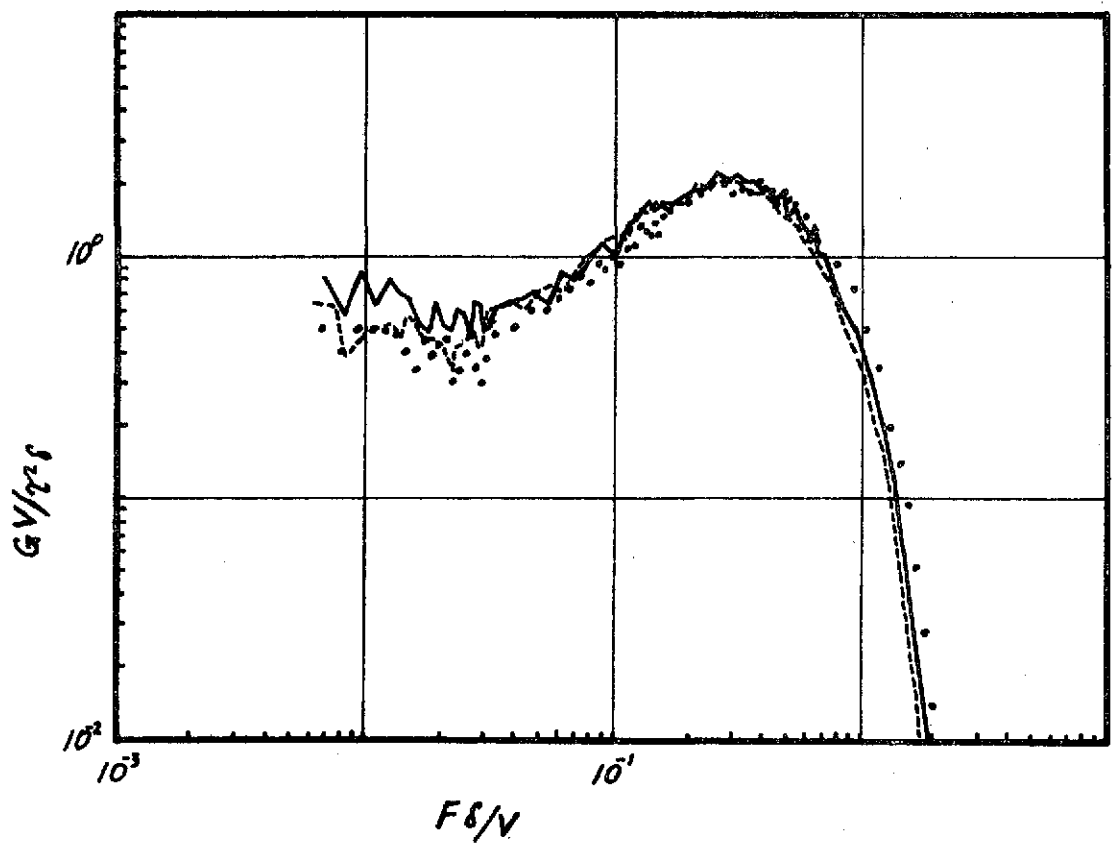
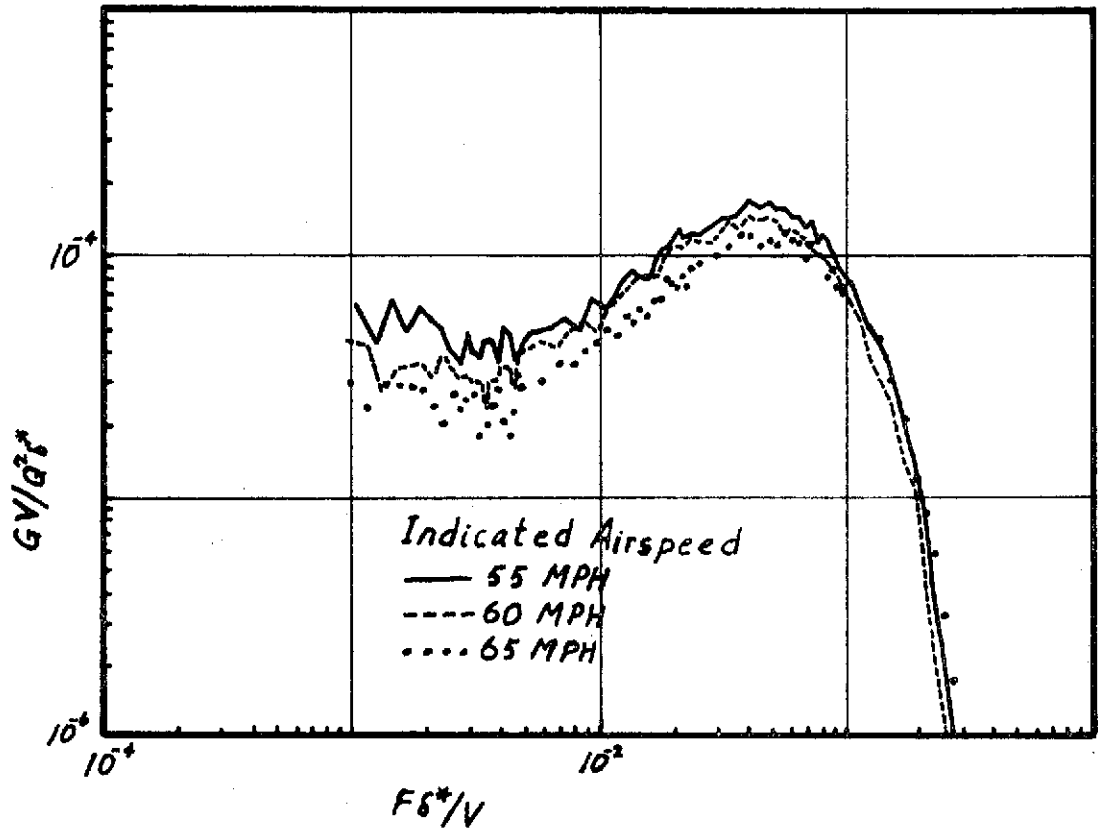


FIG. 34

Airspeed Effects On PSD, 1" Mic

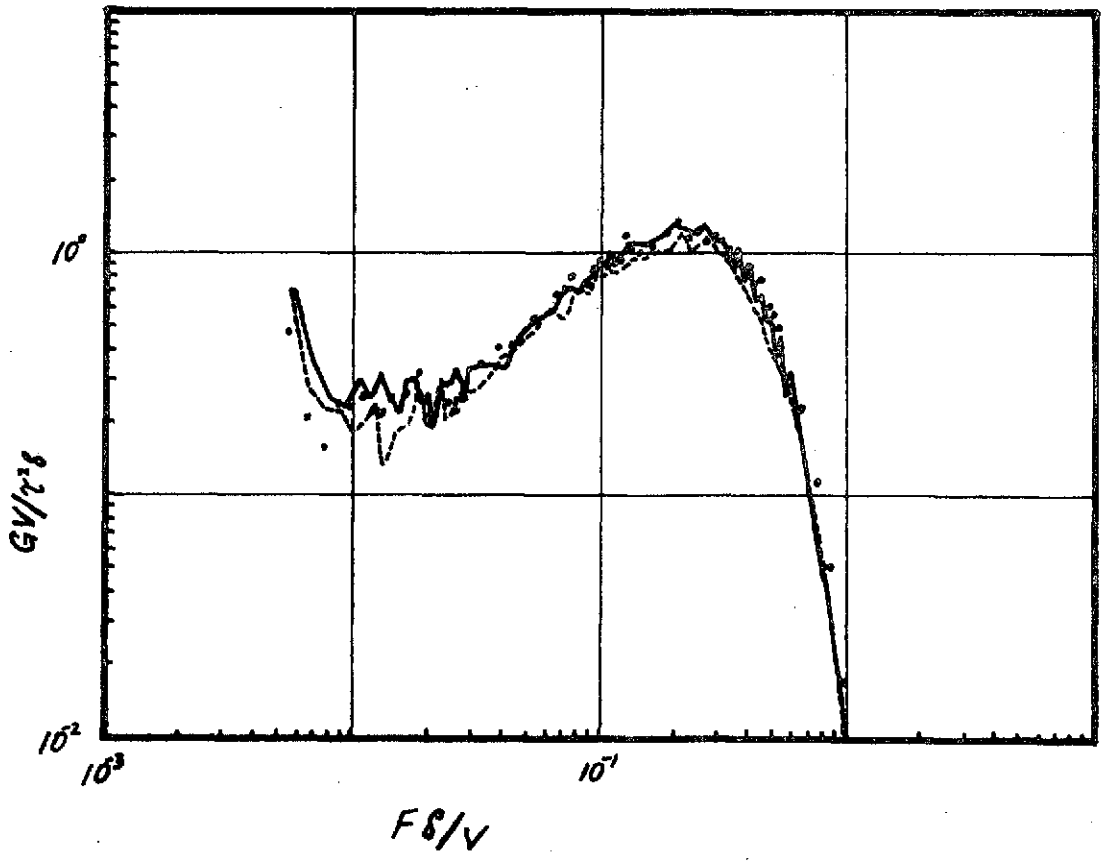
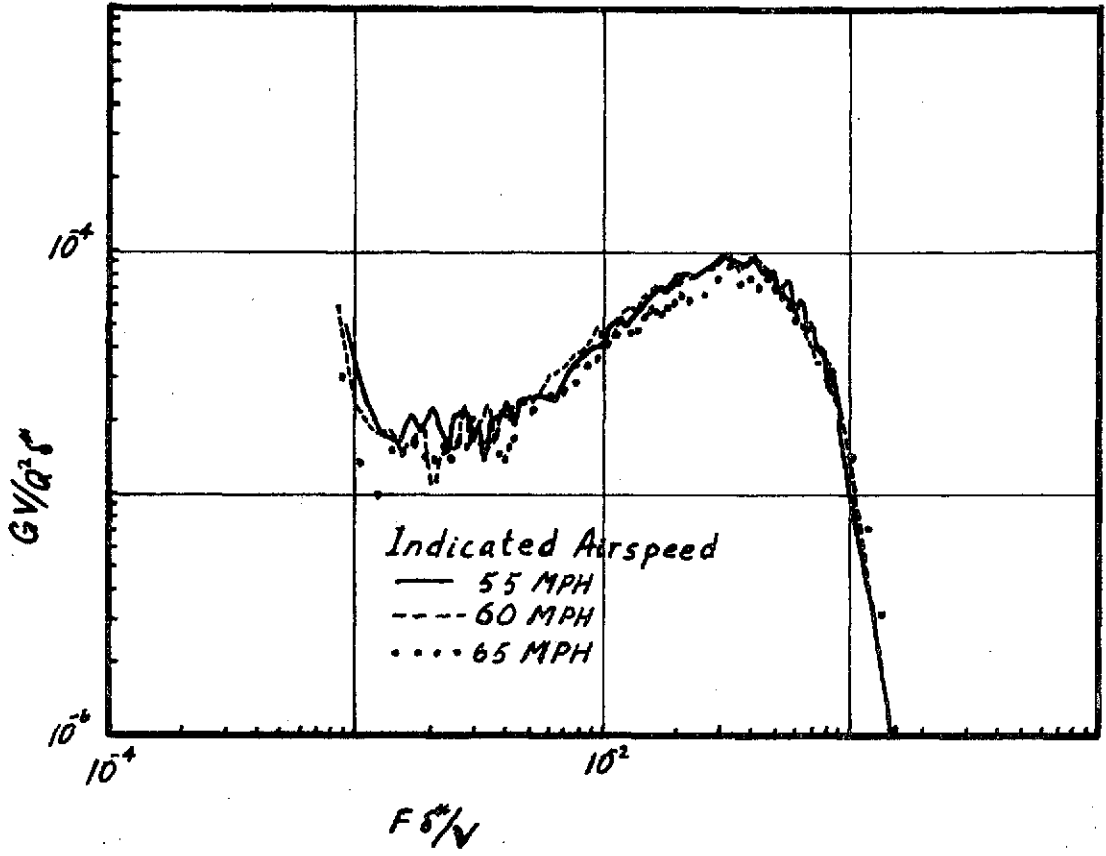


FIG. 35

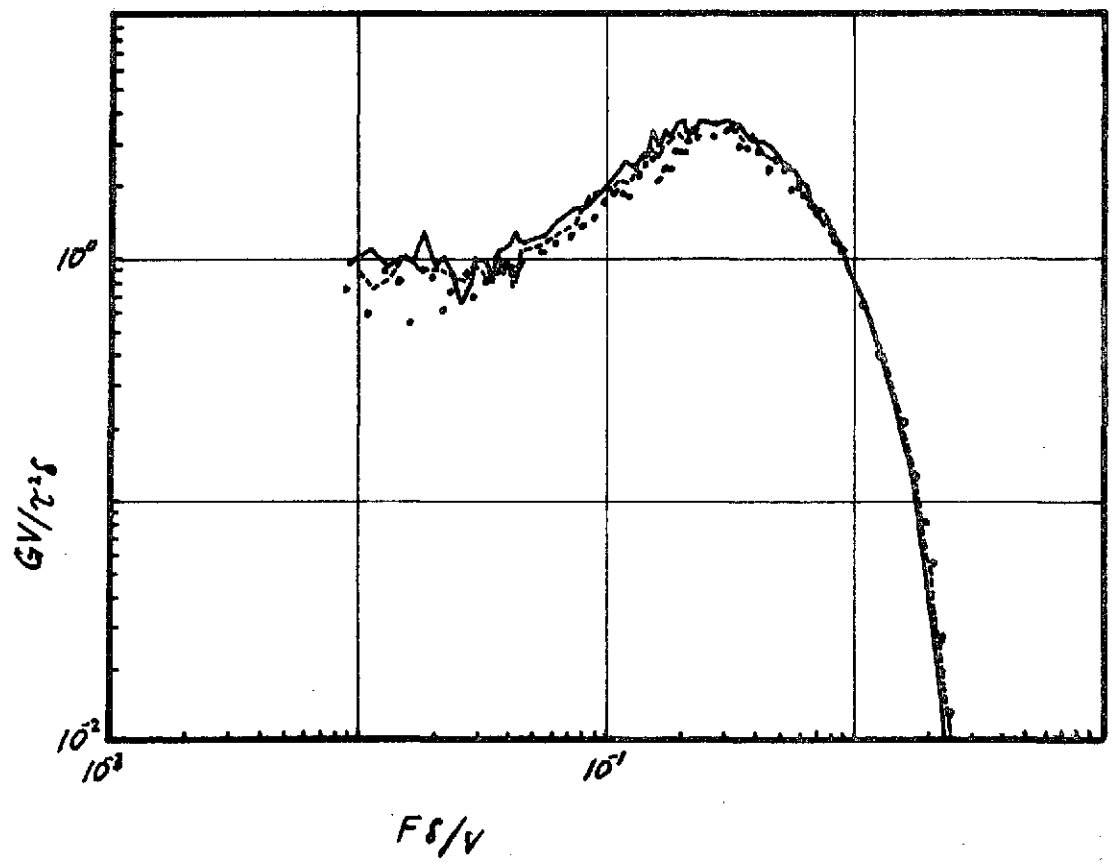
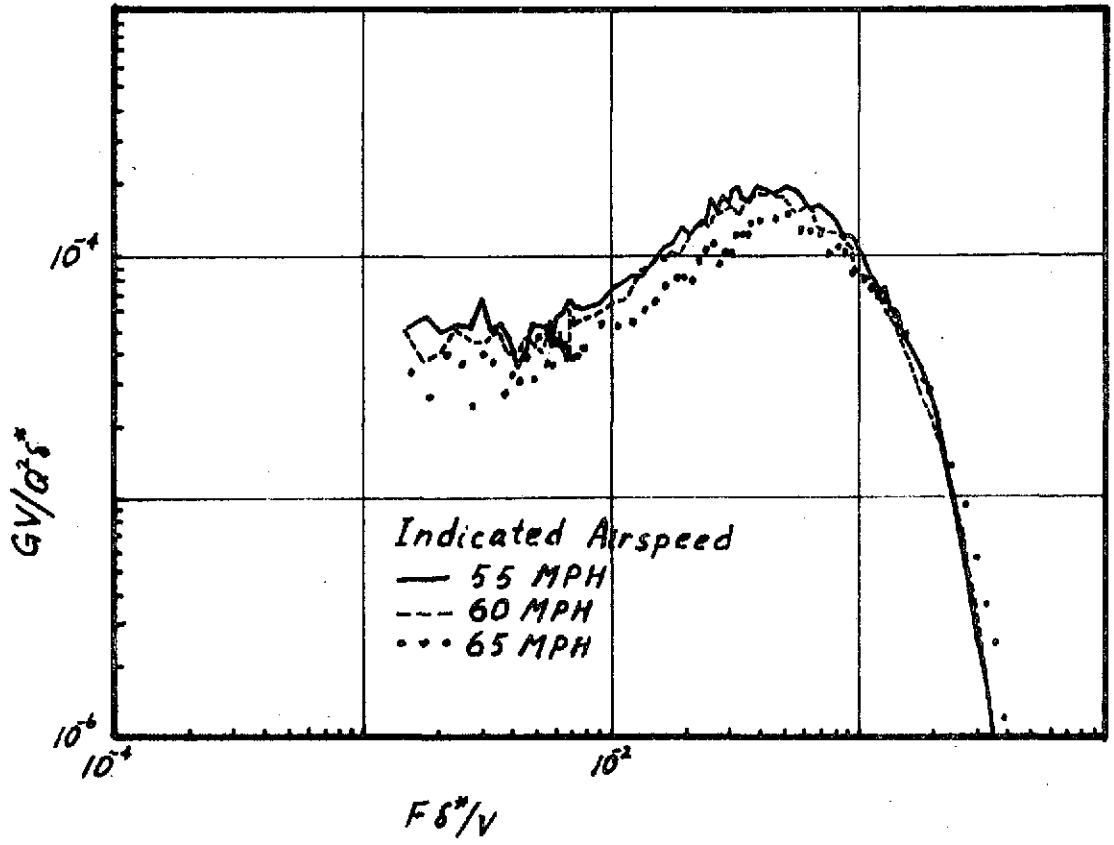


FIG. 36

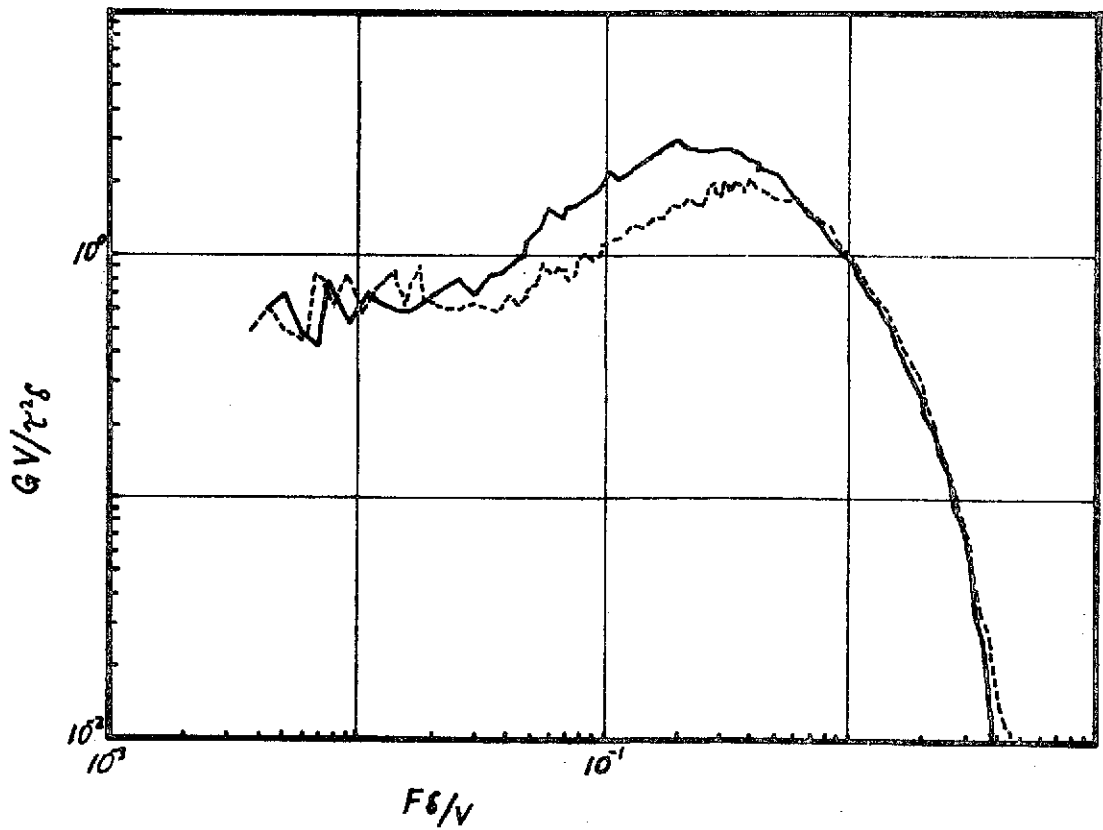
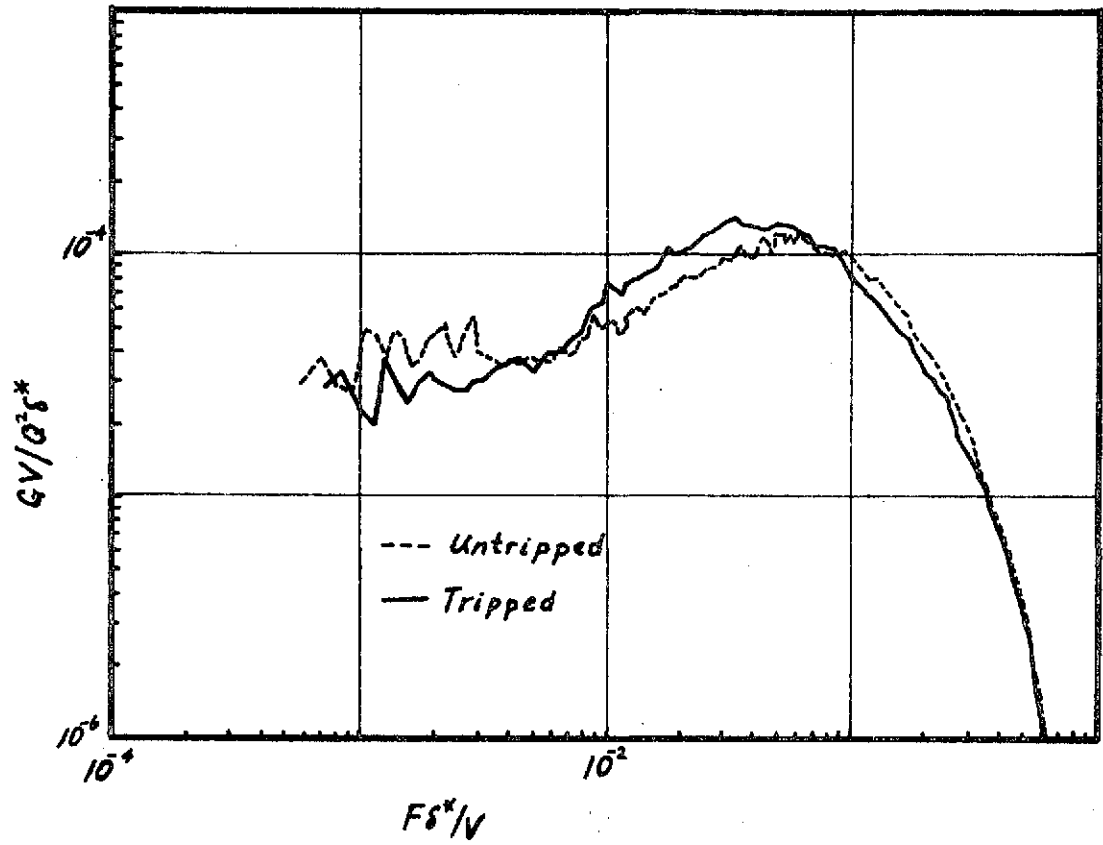


FIG. 37

Effects Of Tripping On PSD, 1/2" Mic

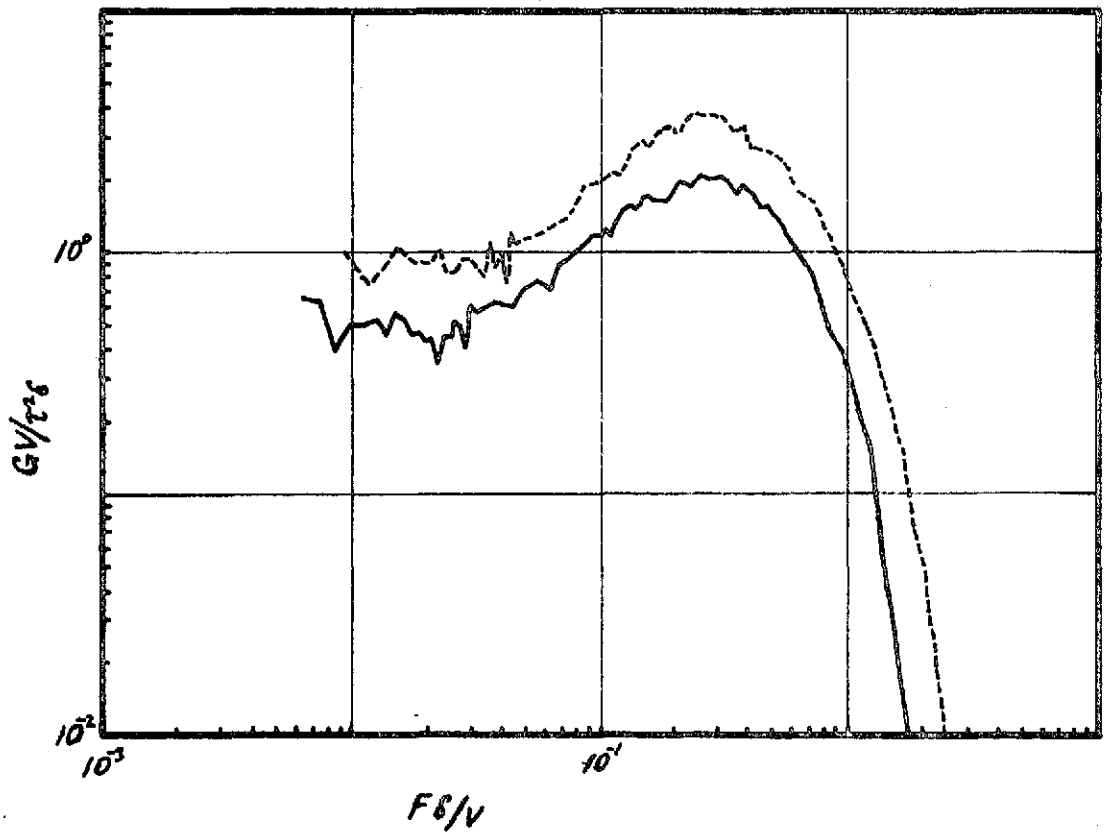
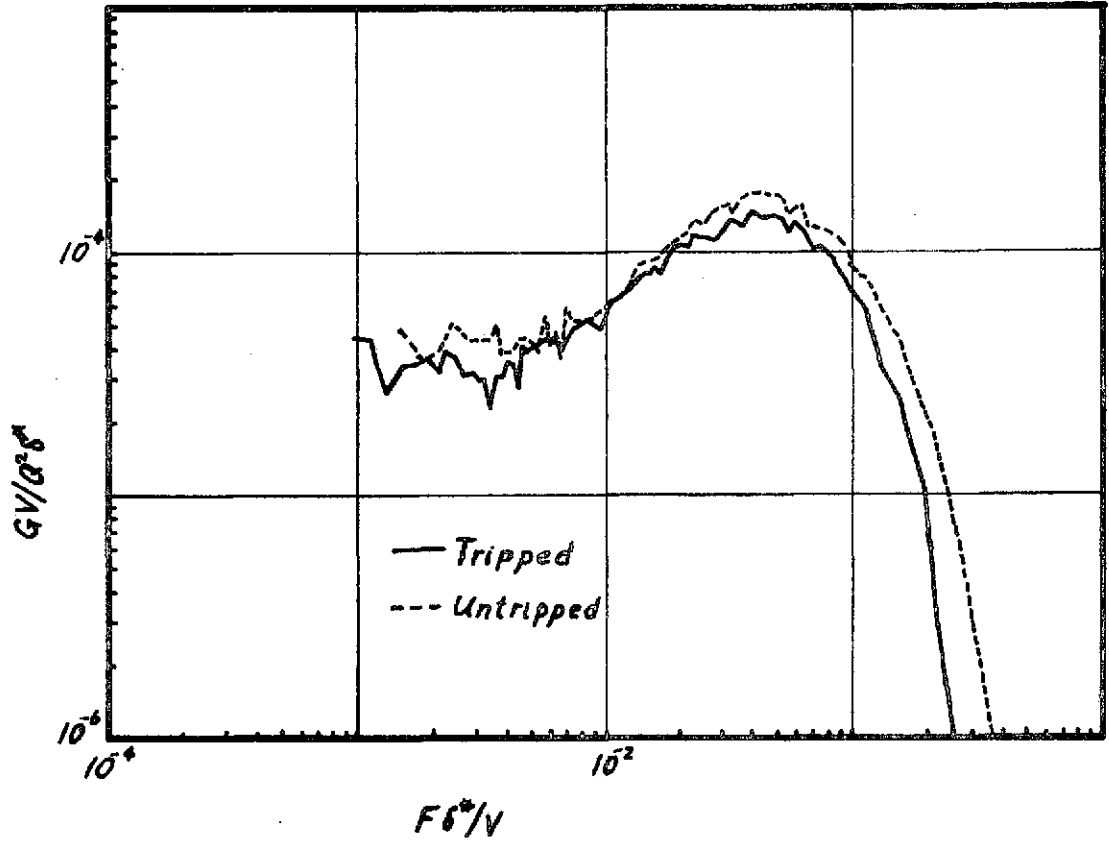


FIG. 38

Effects Of Microphone Location On PSD

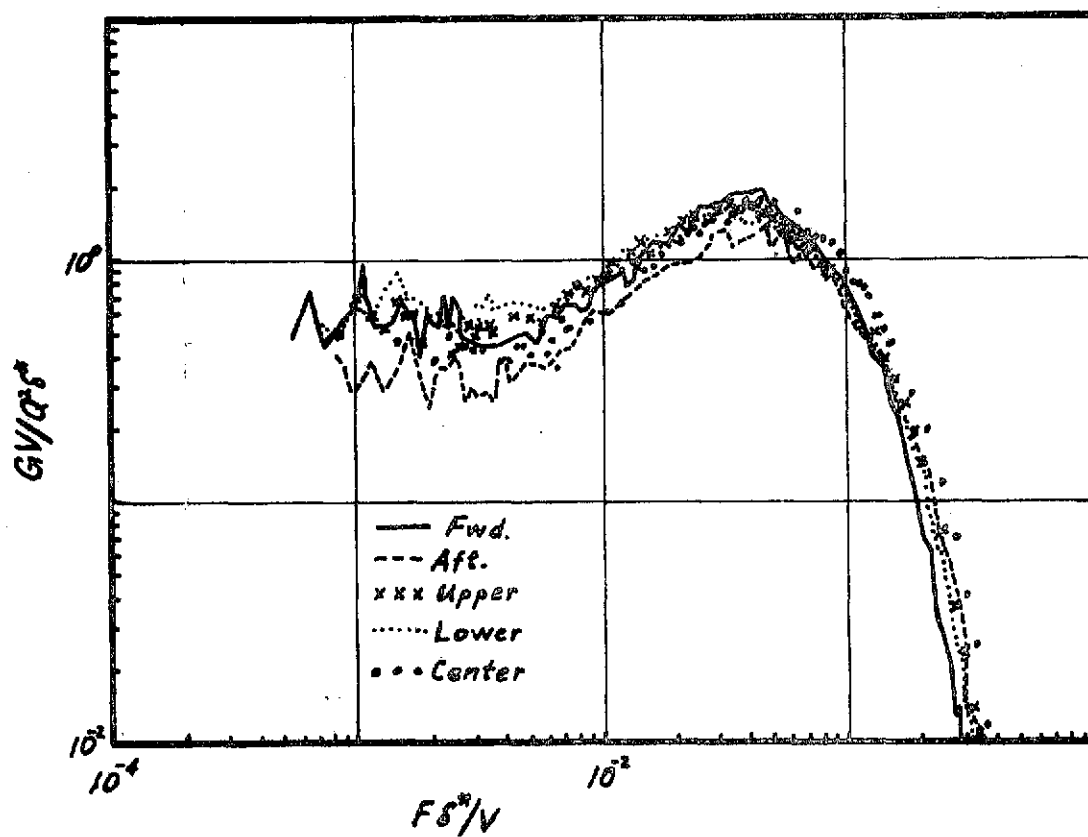


FIG. 39

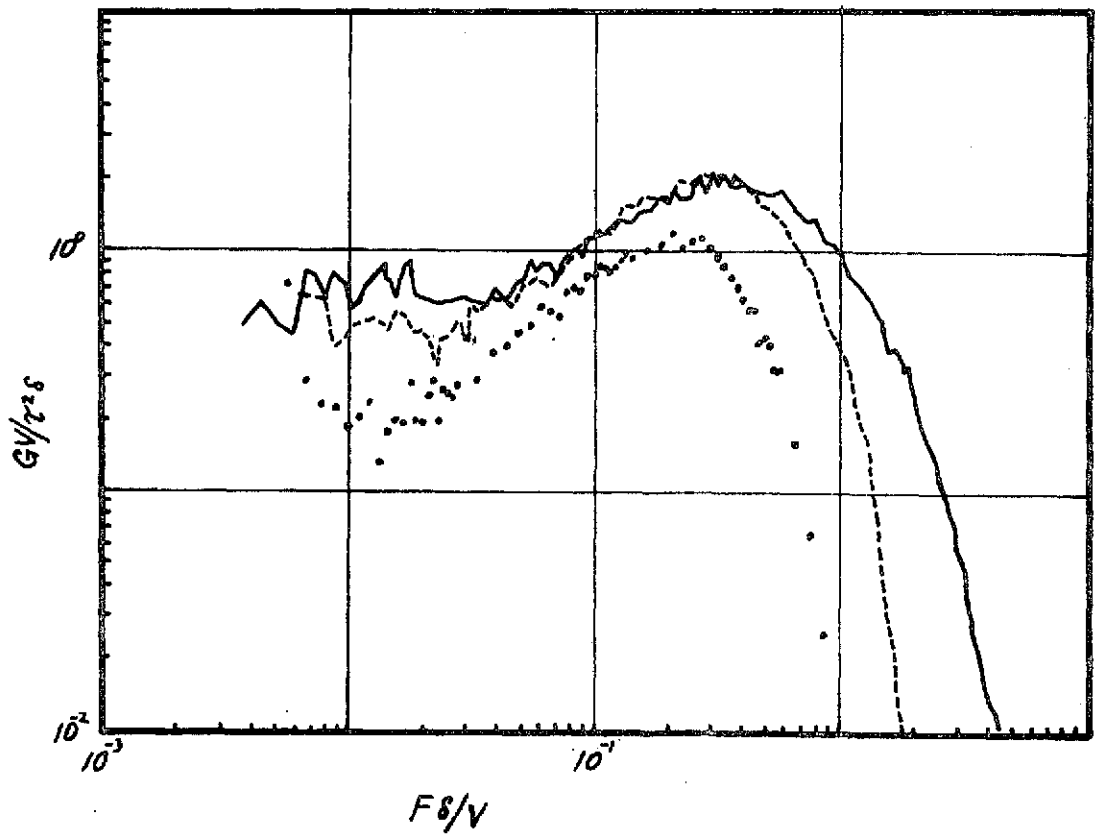
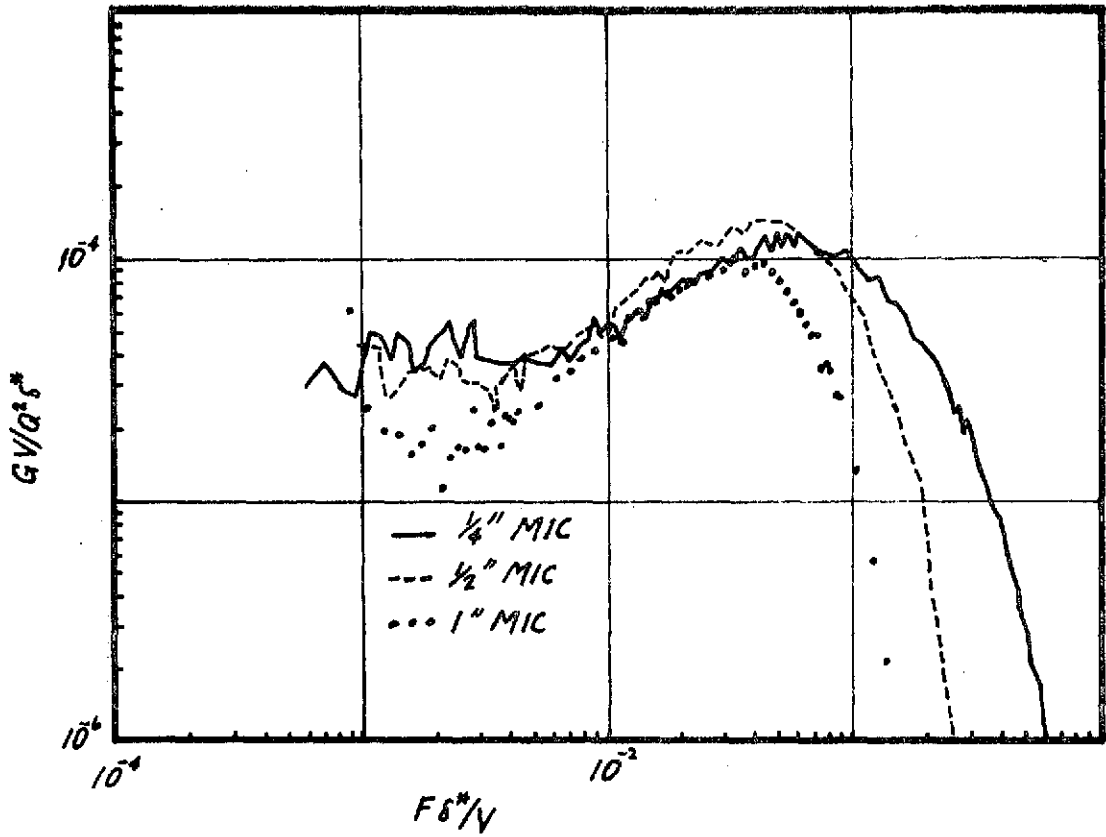


FIG. 40

C-2

Corcos Correction Applied To Fig. 40

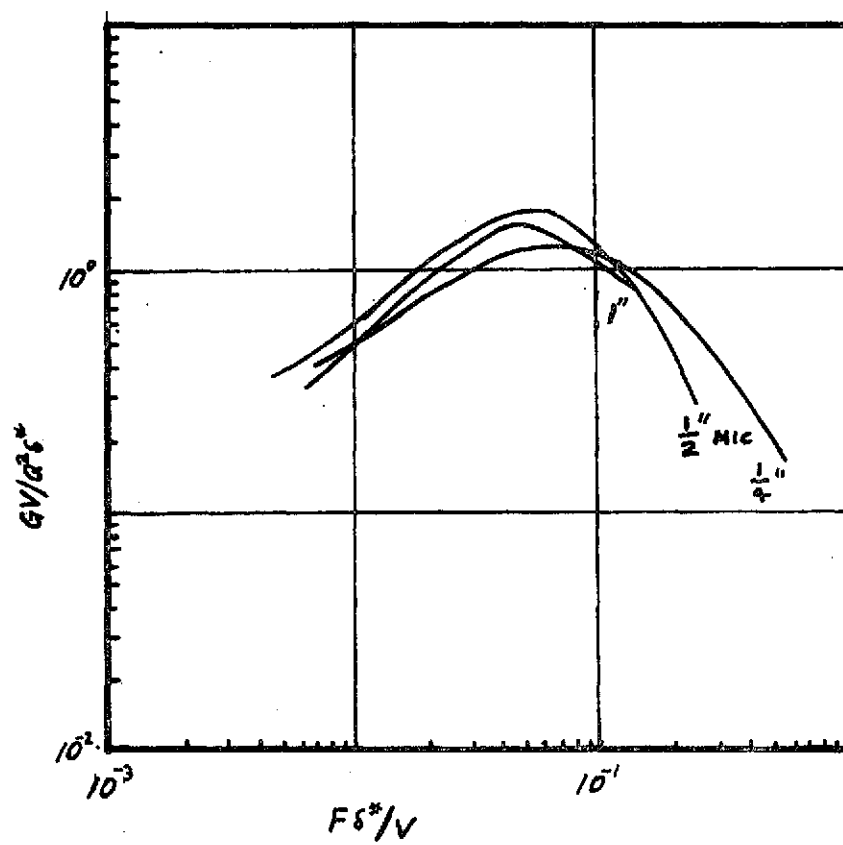


FIG. 41

Microphone PSD Histories

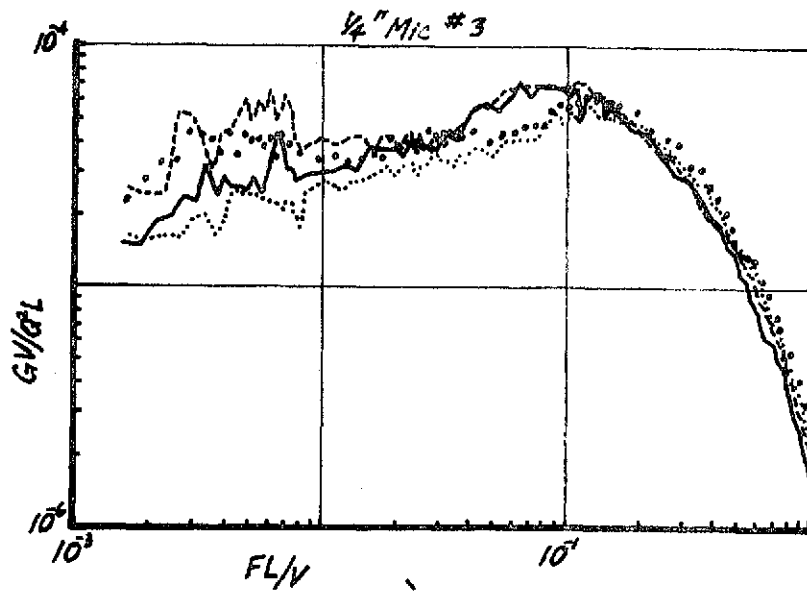
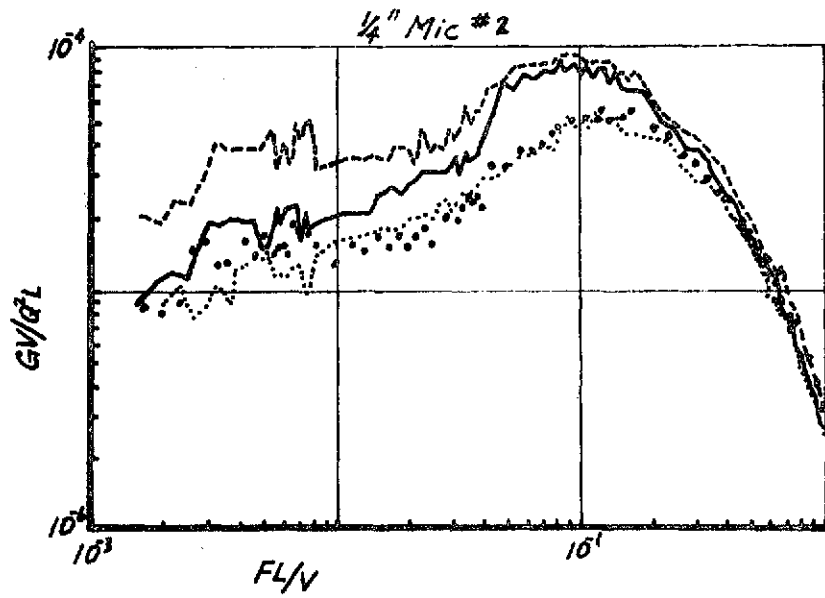
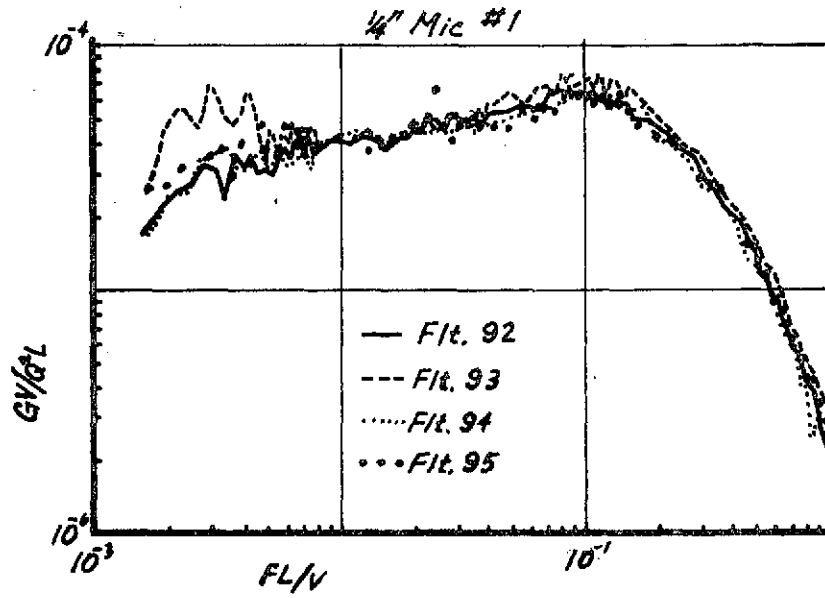


FIG. 42

FIG. 43 - Microphone PSD Histories

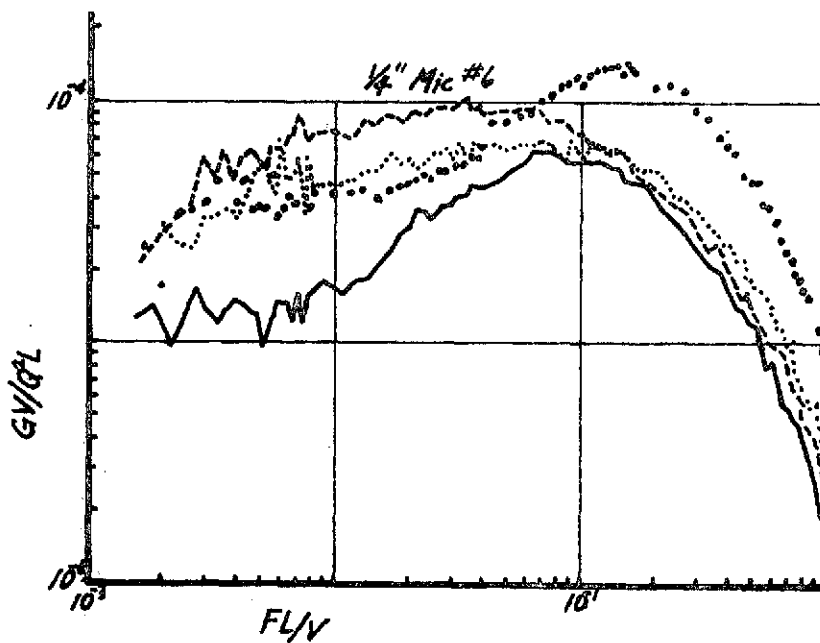
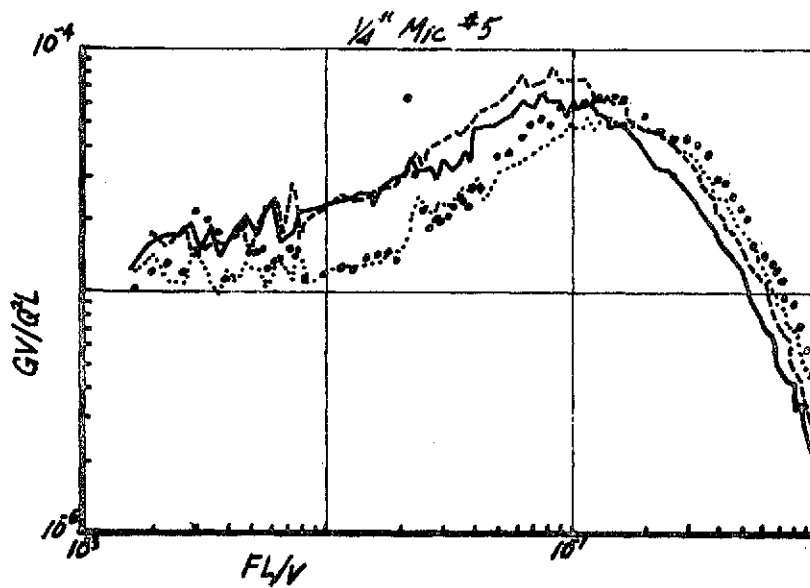
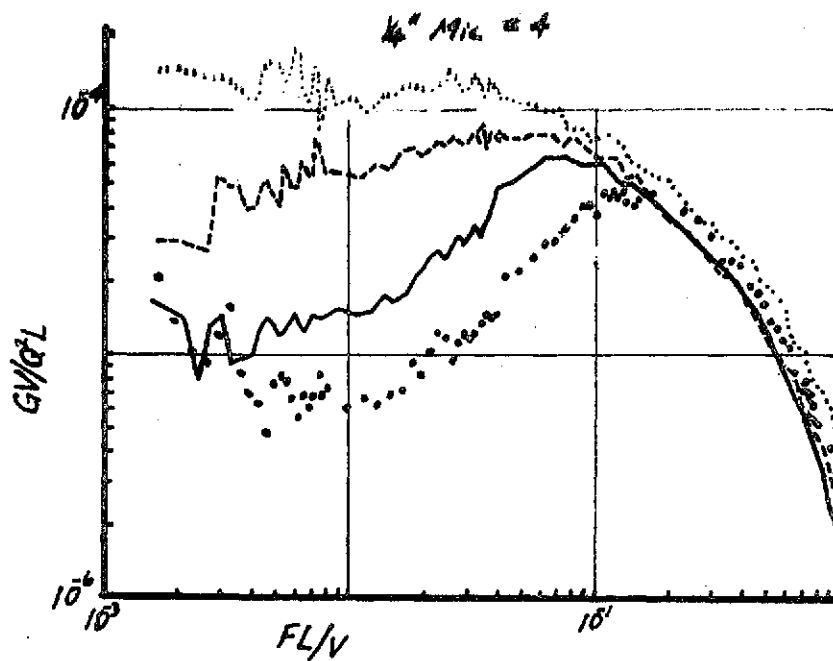
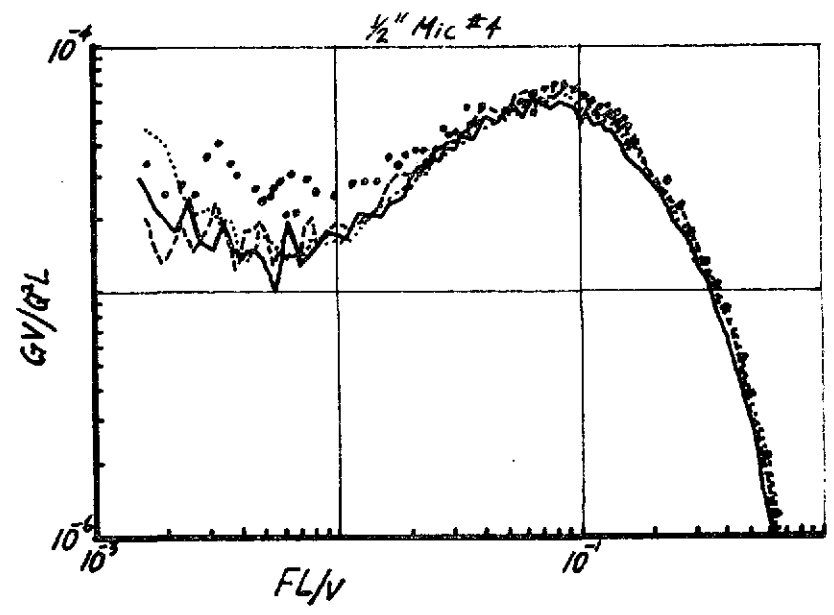
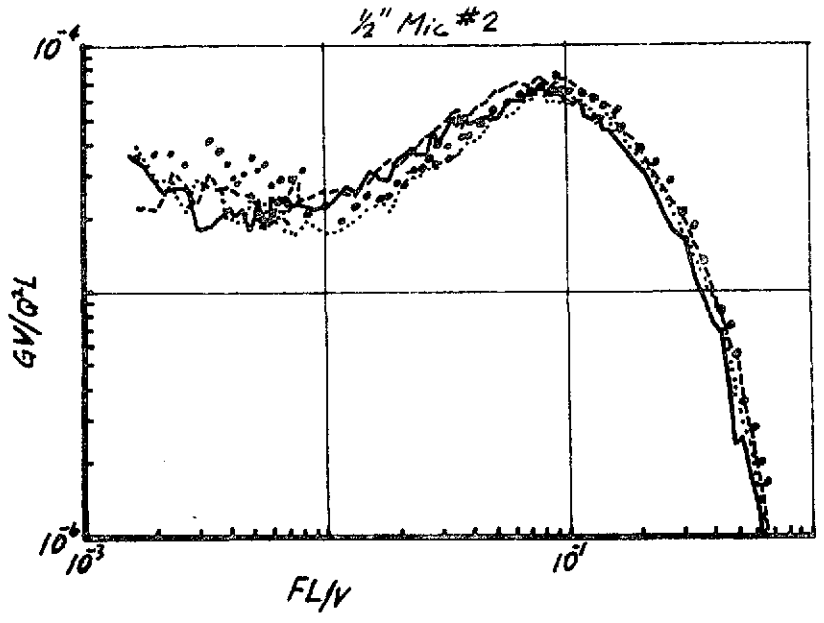
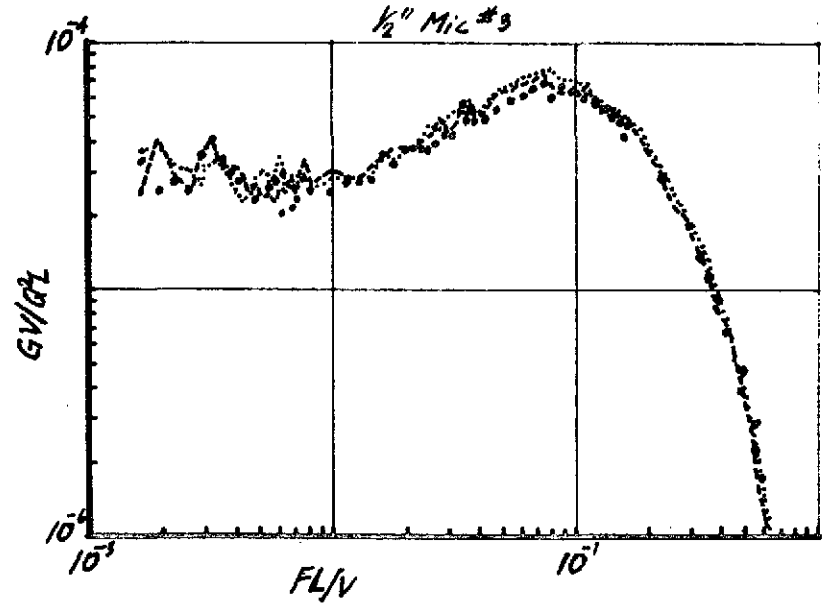
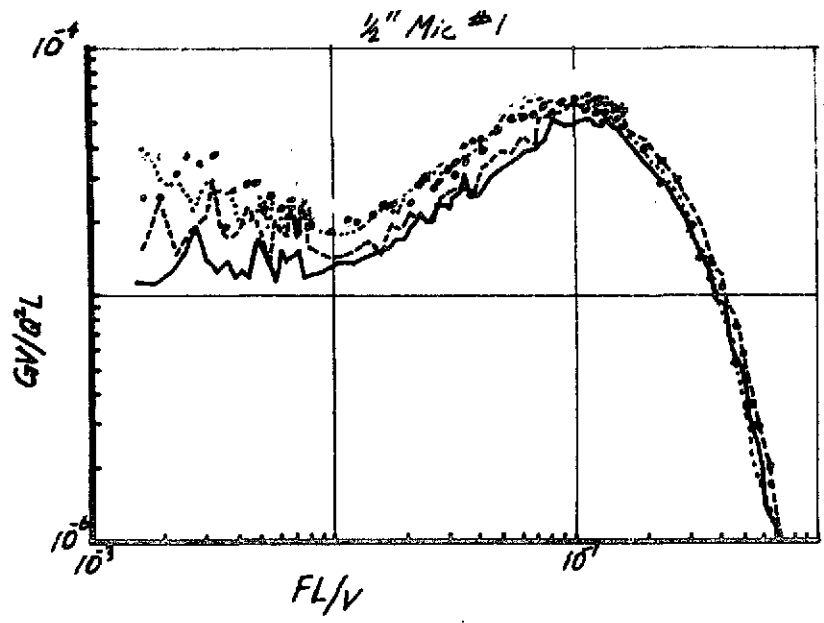


FIG. 44

Microphone PSD Histories



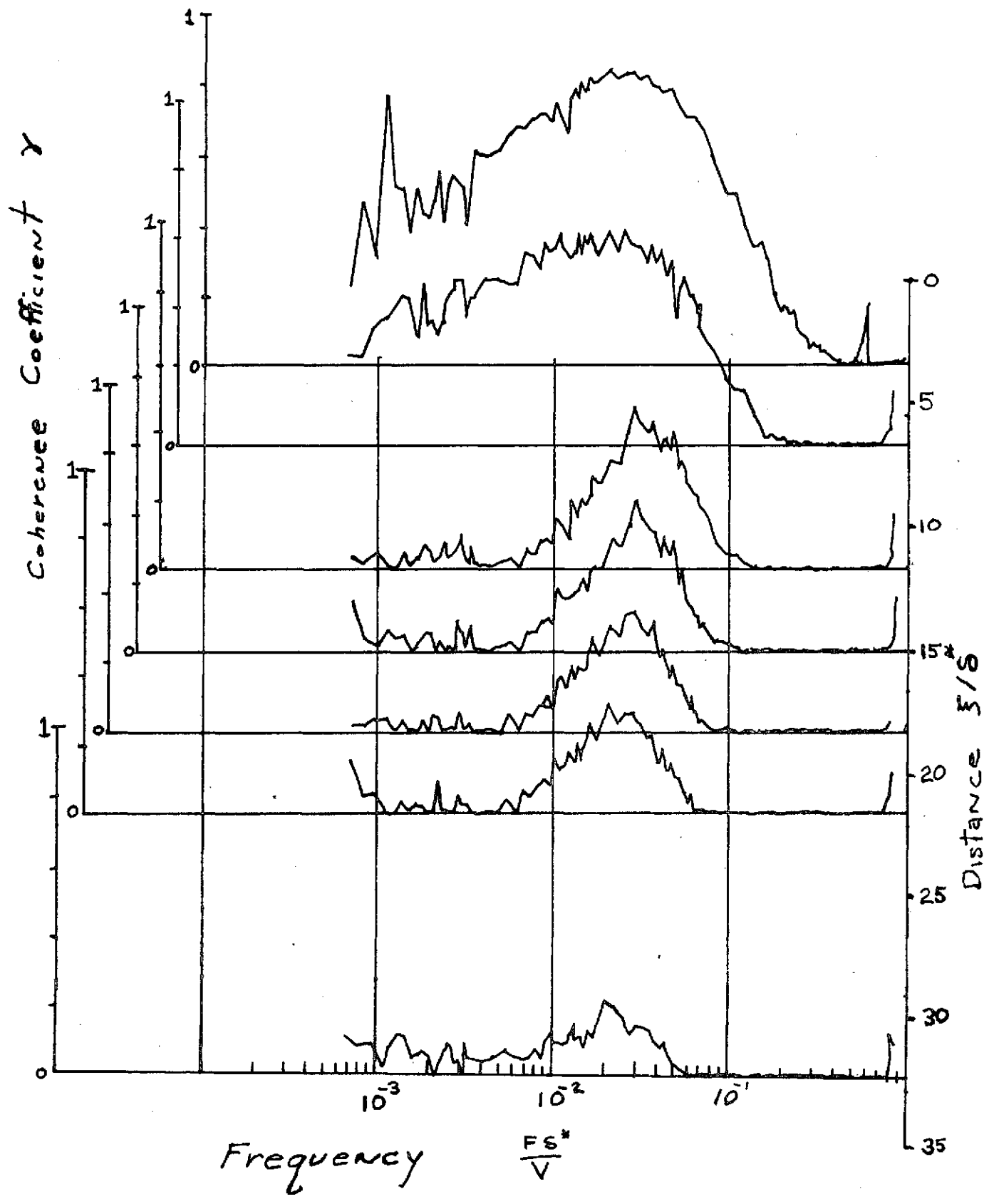


FIG. 45

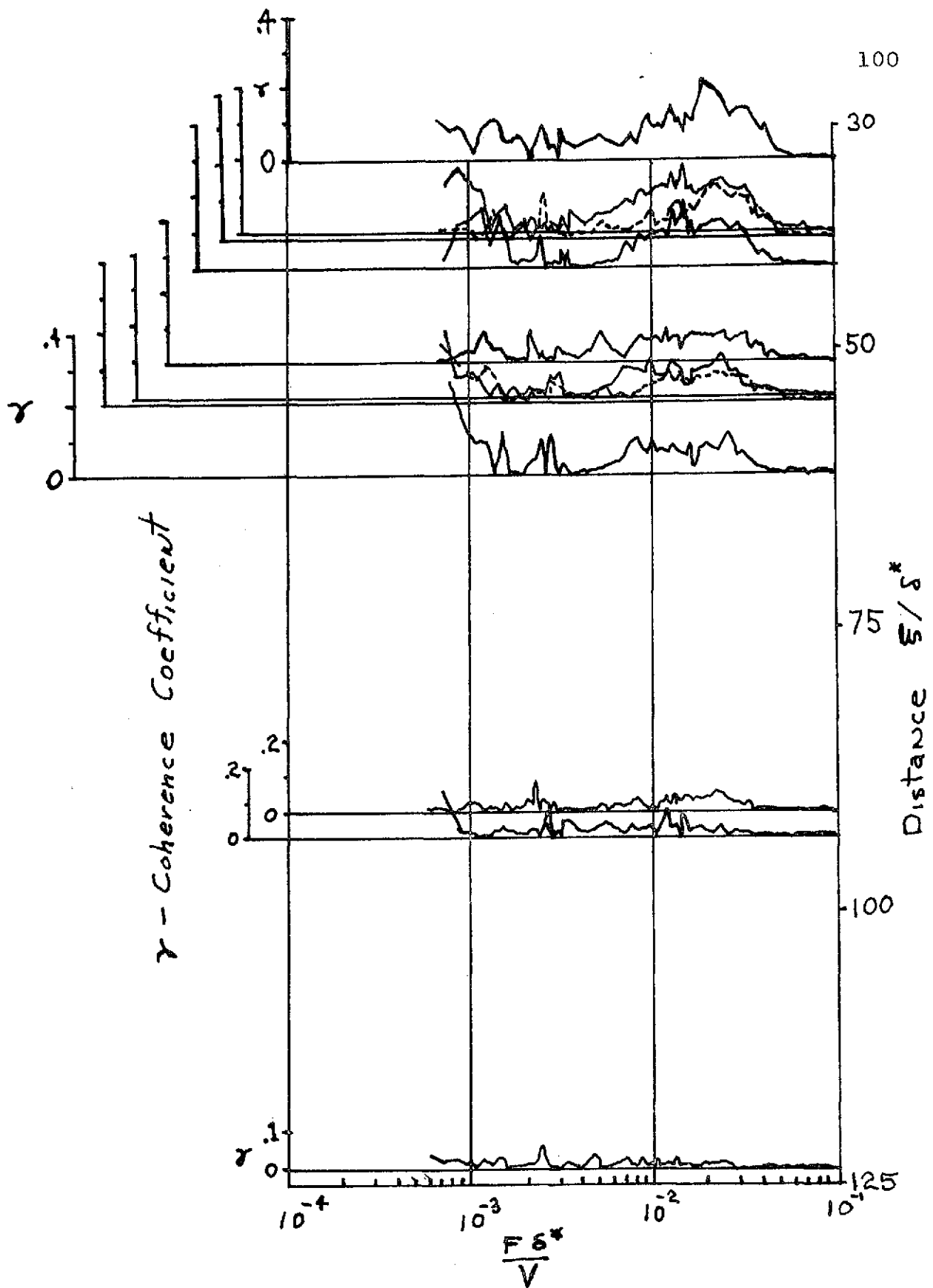


FIG. 46

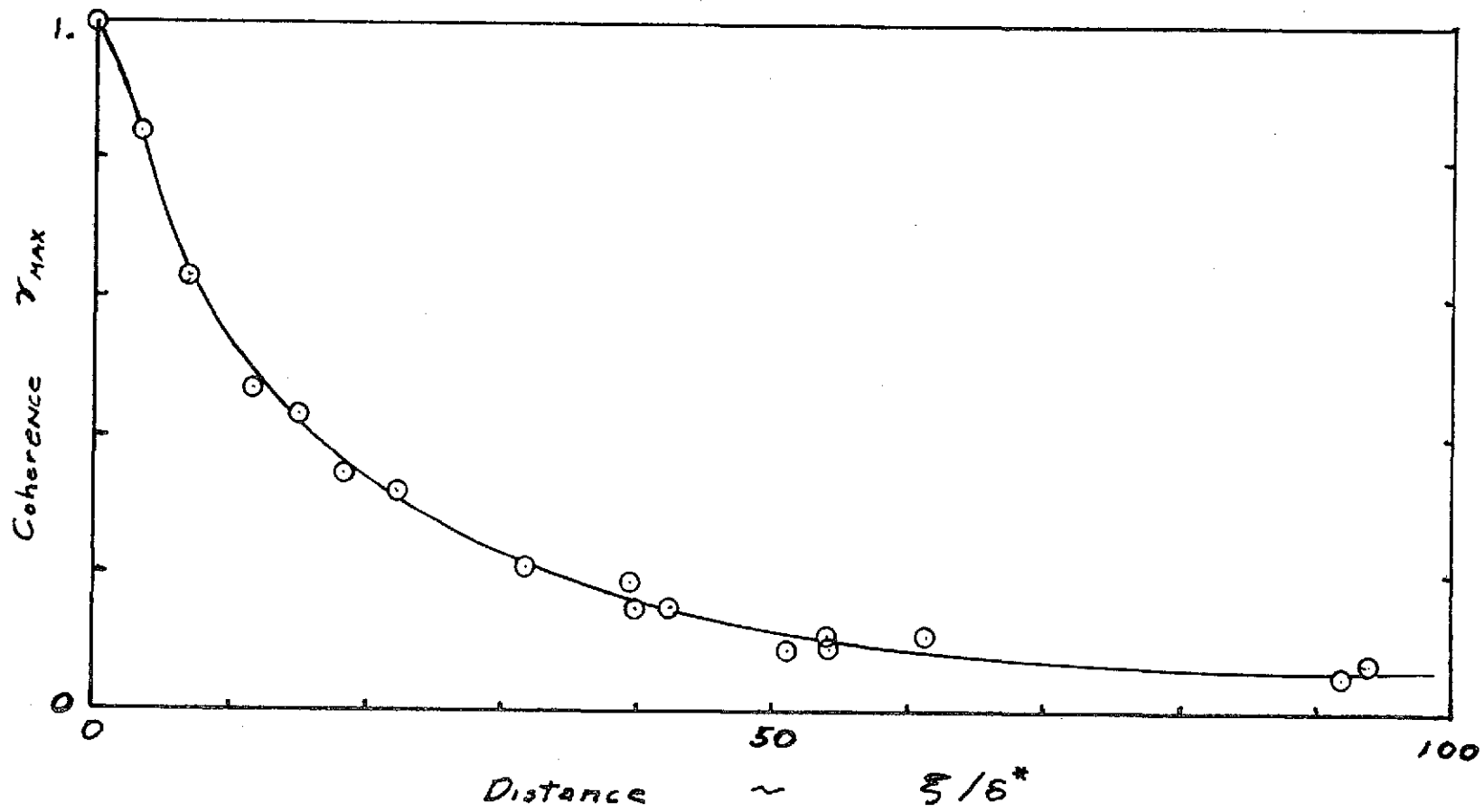


FIG. 47

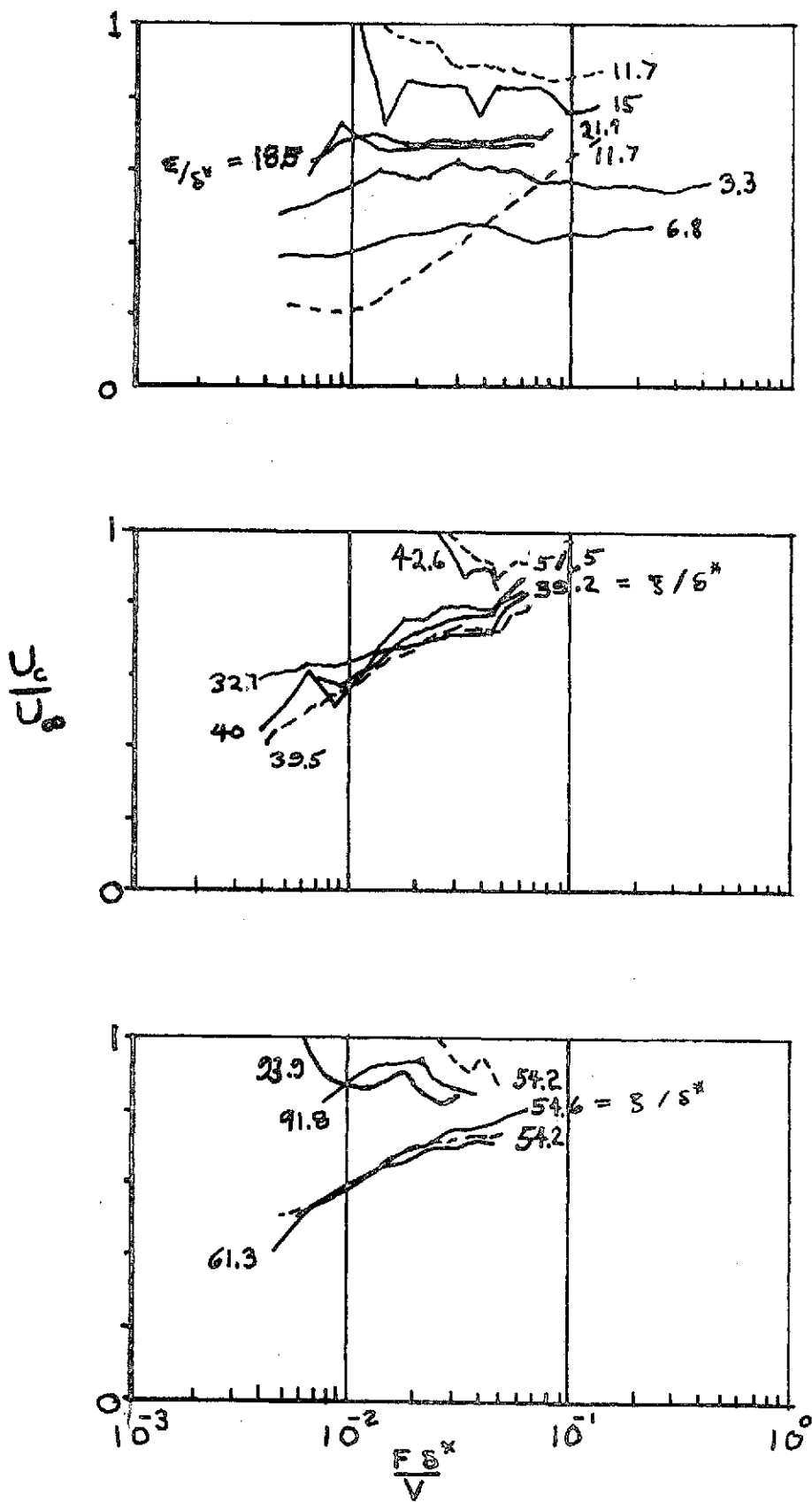


FIG. 48